OPTICAL REFLECTANCE IN FIBROUS TISSUES AND SKELETAL MUSCLES

A Dissertation presented to the Faculty of the Graduate School

University of Missouri

In Partial Fulfillment

Of the Requirements for the Degree

Doctor of Philosophy

---

by

JANAKA C. RANASINGHESAGARA

Dr. Gang Yao, Dissertation Supervisor

DECEMBER 2008

The undersigned, appointed by the dean of the Graduate School, have examined the dissertation entitled

OPTICAL REFLECTANCE IN FIBROUS TISSUES AND SKELETAL MUSCLES

Presented by Janaka C. Ranasinghesagara,

A candidate for the degree of doctor of philosophy,

And hereby certify that, in their opinion, it is worthy of acceptance.

_____

Dr. Gang Yao, Department of Biological Engineering

_____

Dr. Dongsheng Duan,
Department of Molecular Microbiology & Immunology

_____

Dr. Fu-hung Hsieh, Department of Biological Engineering

_____

Dr. Jinglu Tan, Department of Biological Engineering

_____

Dr. John Viator, Department of Biological Engineering

To My wife and Kids

ACKNOWLEDGEMENTS

First of all, I would like to sincerely thank Dr. Gang Yao for his time, patience, understanding, and most importantly his generous advice and friendship during my study at the University of Missouri. Throughout my doctoral studies, he encouraged me to develop independent thinking and research skills. He continuously stimulated me and greatly assisted me with my scientific writing. For everything you have done for me, I thank you.

I am extremely grateful for the assistance, generosity and advice from Prof. Fu-Hung Hsieh. His unconditional support during the last four years is invaluable. I would also like to thank my other doctoral committee members, Drs. Dongsheng Duan, Jinglu Tan, and John Viator, for their constant support and encouragement. I thank Dr. Kerry McDonald for his guidance on single muscle fiber separation, and Dr. Amanda Weaver of South Dakota State University for her enthusiastic support and collaboration.

Many friends have helped me during the last several years. I greatly value their friendship. I extend many thanks to my current and former lab members, especially Jinjun Xia, Xiaofei Fan and Xin Li for their expert advice and spiritual support. I owe special note of gratitude to Ya Guo for his help on advanced C/C++ programming. I am also indebted to our summer interns, Christine Ku and Vanessa Escalera. I would like to thank meat lab manager Rick Disselhorst, and senior research specialist, Harold Huff for their enthusiastic support.

I thank my deceased parents for setting up a path for fulfilling my dreams. I would like to thank all my siblings and their spouses for their support. I am grateful to my eldest sister, Lani for her continuous support and encouragement during my stay in the US.

Finally, and most importantly, I would like to thank my wife Himali. Her support, encouragement, unwavering love and faith were the bedrock for the last nine years. With minimum support from me, she kept the entire family's life in proper perspective. Her tolerance of my occasional improper moods showed her devotion and love. I thank my lovely sons, Chamidu and Nethum for the happiness they have brought to my life.

TABLE OF CONTENTS

LIST OF FIGURES

LIST OF TABLES

Table **Page**

OPTICAL REFLECTANCE IN FIBROUS TISSUES AND SKELETAL MUSCLES

Janaka C. Ranasinghesagara

Dr. Gang Yao, Dissertation Supervisor

ABSTRACT

We studied two biological tissues with optically anisotropic structures: high moisture soy protein extrudates and skeletal muscles. High moisture extrusion has been used to produce vegetable meat analogs that resemble real animal meat and have significant health benefits. Since visual and textural properties are key factors for consumer acceptance, assessing fiber formation in the extruded soy protein product is important for quality control purpose. A non-destructive method based on photon migration was developed to measure fiber formation in extruded soy proteins. The measured fiber formation index in intact samples showed good agreement with that obtained from image analysis on peeled samples. By implementing this new method in a fast laser scanning system, we have acquired two dimensional mappings of fiber formation and orientation in the entire sample in real time.

In addition to fibrous structures, skeletal muscles have a unique periodic sarcomere structure which produces strong light diffractions. However, inconsistent experimental results have been reported in single fiber diffraction studies. By applying the three-

dimensional coupled wave theory in a physical sarcomere model, we found that a variety of experimental observations can be explained if inhomogeneous muscle morphological profiles are considered. We also discovered that the sarcomere structure produced a unique optical reflectance pattern in whole muscle. None of the existing light propagation theories are able to describe this pattern. We developed a Monte Carlo model incorporating the sarcomere diffraction effect. The simulated results quantitatively resemble the unique patterns observed in experiments.

We used a set of parameters to quantify the optical reflectance profiles produced by a point incident light in whole muscle. Two parameters, q and B, were obtained by numerically fitting the equi-intensity contours of the reflectance pattern. Two spatial gradients were calculated along the directions parallel and perpendicular to muscle fibers. The mean diffuse intensity was obtained by excluding the specular reflectance. These five parameters provide a comprehensive and complete description of the diffuse reflectance in muscle. In a study of 336 muscle samples, we found these optical parameters were subject to the effects of different muscle physical and biochemical factors. Different types of muscle have significantly different diffuse intensities. Aging shows different effects on the q parameter in different muscles. In addition, the mean diffuse intensity is significantly different ($p<0.05$) in different animal breeds. Optical parameters showed good correlations with Warner-Bratzler shear force. Further studies on a large sample group are necessary to develop a statistical model to predict muscle physical and chemical properties using these non-destructive optical measurements.

CHAPTER 1

INTRODUCTION AND BACKGROUND

Optical techniques have been used in many areas such as biomedicine, food and agriculture industry (Tuchin, 2000; Nioka and Chance, 2005; Liu and others 2003; Xia and others 2007; Montes and others 2006; Lu and Ariana, 2002). Optical methods carry some intrinsic advantages. They are fast, non toxic and non invasive. In addition, optical tools are portable and economical (Raghavachari, 2001). The majority of biological tissues are turbid or highly scattering. In many existing studies, biological tissues are treated as isotropic, i.e., the scattering process is independent of the light incident direction. However, many tissues such as skin, dentin, skeletal muscle, white matter in brain are optically anisotropic (Nickell and others 2000; Kienle and others 2003; Binzoni and others 2006; Heiskala and others 2007). It is important to understand the effect of anisotropic tissue structures on optical scattering. Such knowledge will help in designing, developing and utilizing optical techniques to accurately retrieve physiological information from anisotropic tissues.

Two different anisotropic tissues have been studied in this dissertation. First, we studied light propagation in fibrous tissues by using high moisture extrudates as a model. Second, we studied light propagation in skeletal muscles. A brief introductory of these two tissues and the related existing work are given below.

1.1 HIGH MOISTURE EXTRUDATES

Soy beans contain the highest amount of protein content among all legumes (Wolf and Cowan, 1975). Soy foods have become very popular in the western world in the last

25 years because of their proven health benefits such as low saturated fat and no cholesterol. Soy food sales, including high moisture extrusion (40-80%) products, have grown to $4 billion in 2005 (Golbitz, 2006).

Thermoplastic expansion is a common method used in producing texturized vegetable proteins (Lin and others 2002). The method has become popular because it is less sophisticated, low cost, and produces no waste. High moisture extrusion technology (Lin and others 2000; 2002) is promising for texturizing vegetable proteins into fibrous products that resemble chicken or turkey breast meat in appearance and taste sensation. Such meat analogs are good alternatives for real animal meat products. They are ideal alternatives to meat for those who are unable to consume animal meat due to various reasons such as cost, health problems, or religious restrictions.

Both single and twin screw extruders can be used in the extrusion process. Twin screw extruders have more mixing capacity and higher throughput than single screw extruders. The extrusion process generates high shear force and pressure in the barrel (Lin and others, 2000). As a result, the protein melts into a viscoelastic material and forms new bonds and cross links. In the event of moisture insertion, this plasticized material expands and obtains the shape of the die. Bonded proteins form fibers aligning with the direction of extrusion while passing through the die. The amount of moisture and the temperature of heating units can change the fiber formation in high moisture soy extrudates (Ning, 1993).

For quality control purposes, it is important to develop non-destructive techniques to quantify fiber formation of extrudates during the manufacturing process because visual and textural properties are the key factors for consumer acceptance. Textural profile

analysis (Kazemzadeh and others 1986; Breene and Baker, 1975) has been used to investigate extruded protein products. However, these methods are not successful in describing the fibrous characteristics of protein products extruded under high moisture. Results obtained from textural profile analysis are mainly influenced by sample moisture content and have a poor correlation with fiber formation (Yao and others 2004). Electron and optical micrographs have been obtained in dissected samples to identify the fiber formation (Lin and others, 2002; Gwiazda and others 1987; Akdogan, 1999; Cheftel and others 1992; Lin and others, 2000). Although microstructure examination provides microscopic information on small sections, it does not accurately describe the global details of fiber formation. Visual inspection of peeled samples is a commonly used method in laboratories (Maningat and others 1999; Roussel, 1996; Akdogan, 1999). This subjective method is destructive and slow, thus is inappropriate for industrial settings.

Recently, Yao and others (2004) developed a method to assess fiber formation using fluorescence polarization spectroscopy. Polarization degrees of the fluorescence light excited by UV irradiation were measured to characterize the fiber formation. The polarization states of fluorescence light are affected by sample fibrous structures. This non-destructive method achieved reliable results when compared with visual inspections. However, fluorescence measurements are susceptible to ambient light because fluorescence emissions are usually weak and the wavelength is within the visible spectrum. Such deficiency is neither convenient nor practical for online monitoring.

In this dissertation, we presented a new optical method based on a theory of photon migration in fibrous tissues. This robust method is ideally positioned to be an online quality control tool for real-time monitoring of fiber formation in soy extrudates.

1.2 LIGHT PROPAGATION IN FIBROUS TISSUE

Several biological tissues and other food related products have optical properties that depend not only on the location but also on the direction. Such media are known as anisotropic media. The validity of using isotropic light propagation models such as diffuse equation on such medium is questionable. Several anisotropic light propagation models have been developed. Several groups (Stark and Lubensky, 1996; Heino and others 2003) proposed a modification to the diffuse approximation for transport equation. They replaced the scalar diffusion coefficient with a diffusion tensor. The anisotropic diffusion equation is

$$\frac{1}{c}\frac{\partial\Phi(\vec{r},t)}{\partial t} - \mathbf{D}\nabla^2\Phi(\vec{r},t) + \mu_a\Phi(\vec{r},t) + S(\vec{r},t). \qquad (1\text{-}1)$$

where c is the light velocity in the medium. Φ, μ_a, and S are fluence rate, absorption coefficient, and the light source respectively. **D** is the diffusion tensor with three none zero diagonal components. However this model was questioned by Kienle (2007) based on his Monte Carlo simulations.

Kienle and others (2003) proposed a method based on light scattering by cylindrical structures (Yousif and Boutros, 1992). They obtained the phase function for different incident angles and applied it in a Monte Carlo simulation. The simulation results were compared with the experimental results obtained in dentin, porcine artery and wood (Kienle and others, 2003; 2004; 2008).

The continuous time random walk (CTRW) theory (Weiss, 1994; Weiss and others 1998) has been used to study the complicated process of light transportation in scattering media. Dagdug and others (2003) have recently extended the CTRW theory to analyze

the light interactions with anisotropic turbid media. In CTRW theory, the sample is modeled as a three dimensional semi-infinite lattice structure with a planner boundary. The position of any point in the lattice is denoted by integer coordinates (x, y, z), where a positive z (z>0) representing the sample interior. Optical reflectance is measured at the planner surface defined by z=0. The photons enter the structure at (0, 0, 0) and follow random walking in the lattice. Photon movement is restricted only to the nearest six neighboring sites in the lattice, where the time between successive steps is random and depends on the transition probability. The transitional probabilities along different axes are different in anisotropic samples. The backscattered reflectance, R at a detection point r =(x, y, 0) can be derived as (Dagdug and others, 2003):

$$R(r) \approx \frac{I_o}{\pi}\left(1+\frac{2}{B}\right)^{0.5}\left(\frac{\sqrt{2\nu}}{Bx^2+y^2+B}\right), \qquad (1\text{-}2)$$

where ν is a parameter that characterizes the relative probability of absorption and scattering in sample; I_0 is the incident light intensity; B is the bias parameter or the ratio of transitional probabilities along the two different axes. B is equal to unity for isotropic scattering. It can be shown from Eq. 1-2 that the equi-intensity distribution of the surface reflectance F(x, y) is an ellipse:

$$F(x, y) = Bx^2 + y^2 = \text{constant}. \qquad (1\text{-}3)$$

Therefore, the bias parameter B can be derived as $(L_L/L_S)^2$, where L_L and L_S are the lengths of the two major axes of the equi-intensity ellipse along the long and short elliptic axes, respectively. This method has been successfully applied in studies of various anisotropic tissue structures (Sviridov and others 2005), and proves to be useful in quantifying fiber formation in meat analogs as shown in Chapters 3 and 4.

1.3 SKELETAL MUSCLES

Skeletal muscle is the largest single organ in most vertebrates and is essential for movements and many important physiological functions (Lieber, 2002; Yu and others 2005). Whole muscle consists of many fascicles, or collections of muscle fibers (muscle cells), encapsulated in an elaborate connective tissue matrix (Macintosh and others 2006). There are hundreds of small myofibrils within each single muscle fiber. The normal mechanical and physiological functions of all striated muscles are realized by the highly organized structures termed sarcomeres (Lieber, 2002).

Sarcomere is responsible for the mechanical and physiological functions of the muscle (Bonnemann and Laing, 2004). The majority of muscular diseases are related to the changes in sarcomere proteins (Proske and Morgan, 2001). Previous studies have shown that length-tension relationship is a reliable predictor of live muscle functions (Lynch, 2004). Pathological status of the muscle will alter this relationship. In reconstructive surgery, sarcomere length itself can be used to predict the muscle functionality (Lieber and others 1994). After vigorous exercise or other forms of extensive physical activity, sarcomeres can be disrupted (Proske and Morgan, 2001). The end results are uneasiness and pain.

A string of sarcomeres arranged in a myofibril aligns precisely in muscle fibers. Sarcomeres are readily observed under light microscope as alternating light and dark bands called I-band and A-band. The periodic appearance of I- and A-band is due to the difference in their optical refractive indices (Huxley and Hanson 1957). The segment of A-band with only myosin proteins is called the H zone. The Z-line and M-line are located in the middle of the I-band and in the middle of the H zone, respectively. The sarcomere

length is defined as the distance between two Z-lines. The “overlap” region refers to the part of the A-band where both actin and myosin are present.

The muscle contraction was explained by Huxley and Hanson (1954) using sliding filament theory. During the contraction, myosin moves along the filament by binding and releasing cross bridges (Lieber, 2002). Adenosine triphosphate (ATP), the chemical energy source, prevents the formation of actomyosin in the resting muscle. In the event of contraction, ATP is hydrolyzed to ADP and those unattached myosins attach to actins and form a temporary actomyosin complex.

In single muscle fiber studies, it was shown optical scattering was related to chemical and physical changes of the sarcomere (Burkholder and Lieber, 2001; Oba and others 1981). But single fiber experiments are invasive and destructive. Non-invasive optical measurements on whole muscle would be desirable.

Conversion of muscle to meat starts when animal is slaughtered. However, muscle continues to metabolize even after death. The absence of blood flow deprives the oxygenation and blocks the removal of waste products (Bate Smith, 1939). The lack of the oxygenation changes the aerobic production of energy to anaerobic (Lieber, 2002). The anaerobic process produces lactic acid as byproducts. This lactic accumulation in muscle reduces the pH from neutral (~7) to lower values (5.5 ~5.7). Once pH becomes very low, anaerobic energy transformation process is halted because enzymes associated with the process are deactivated. As a result, ATP regeneration is stopped and existing ATP is eventually depleted. In the absence of ATP, actin and myosin filament forms an irreversible actomyosin complex. At this stage, muscle is in “rigor”.

Meat is the major protein source for human nutrition. Meat tenderness, especially in beef, is the dominant palatability attribute considered by US consumers (Rhodes and others 1955; Van Syckle and Brough Jr, 1958; Ramsey and others 1963; Koch and others 1976) who are willing to pay extra money for tender beef (Shackelford and others 2001; Lusk and others 2001). Warner-Bratzler shear force is the standard method to evaluate the tenderness of the meat. According to our group's recent studies (Xia and others, 2007; 2008a; 2008b), optical scattering shows a good correlation with the Warner-Bratzler shear force. Optical based methods have the greatest potential for online industrial applications because they are rapid, non-destructive and inexpensive.

1.4 LIGHT-MUSCLE INTERACTIONS

Laser diffraction has been widely applied in studies of single muscle fibers or small fiber bundles. The refractive index variation between the A-band and the I-band in sarcomere act as an optical grating (Baskin and others 1979). Most previous experimental studies on light diffraction in single muscle fibers can be classified into two categories. The first category is related to the Bragg diffraction phenomenon (Rudel and Zite-Ferenczy, 1979; Thornhill and others 1991; Brenner, 1985; Baskin and others 1981). In such studies, diffraction efficiencies were measured as a function of incident angles (ω scan). In the second category, light diffraction efficiencies were measured at different sarcomere lengths (Paolini and others 1976; Baskin and others, 1979; Kawai and Kuntz, 1973; Buchthal and Knappeis, 1940) by stretching the muscle fibers. Classical diffraction theories have been applied to study the diffraction of light by muscle fibers (Fujime and Yoshino, 1978; Fujime, 1975; Yeh and others 1980; Kawai and Kuntz, 1973). Leung (1984) introduced a more complicated model by considering volume nature of the muscle

fiber. Although they provide good explanations for the relationship between sarcomere length and diffraction angles, most of these theories fail to explain the effects of fiber thicknesses on diffraction efficiency.

Huxley (1990) was the first to model the sarcomere as a thick grating unit. He considered wave coupling and studied how constructive and destructive interference can change diffraction intensity across the fiber. However, his model was not capable of analyzing muscle fibers with different striation patterns. Based on Huxley and Hanson's work (1957) on refractive index modulation in sarcomeres, Thornhill and others (1991) described a much improved sarcomere model and applied the first-order coupled wave theory developed by Kogelnik (1969). Sidick and others (1992) further introduced rigorous coupled wave analysis for planar diffraction (2DCW) (Moharam and Gaylord, 1982) to analyze light diffraction in muscle fibers for TE polarization. Their method was later extended to study the muscle birefringence effect (Sidick and others 1994).

All studies mentioned above were applied to discuss light propagation in muscle fibers. However, few investigations were conducted to study light propagation in whole muscles. Marquez and others (1998) and Zijp and ter Bosch (1998) measured optical reflectance in chicken and bovine muscles, respectively. They applied diffuse approximation of transport equation to derive optical properties of muscles and concluded that light propagation in skeletal muscle was orientation dependent. The same theory was used by other groups (Yu and others, 2005; Bargo and others 2005; Xia and others, 2007; 2008a; 2008b). For the first time, Binzoni and others (2006) have applied anisotropic light propagation model based on random walk theory to analyze optical reflectance in muscle. However, this theory failed to reproduce the optical reflectance

images observed in skeletal muscles. Our experimental results indicated that no existing model can accurately explain light propagation in skeletal muscle.

A precise assessment of optical parameters is the key factor to obtain correct physical and physiological parameters. As current photon migration theories cannot explain light propagation in the muscle, development of an anisotropic light propagation model is necessary. Such a model would be useful when applying optical methods for muscle physiological studies, clinical diagnosis and meat tenderness evaluations.

1.5 OUTLINES OF THE DISSERTATION WORK

This dissertation focuses on the study of light propagation in two different anisotropic tissues. In the first part, optical imaging techniques were developed to quantify fiber formations in fibrous meat analogs. Food manufacturers are looking for a method to assess fiber formation in soy protein products extruded under high moisture. In Chapter 2, we present an image processing technique based on Hough transform to calculate the fiber formation index in soy protein extrusions. Although dissected samples are needed, this method can replace human visual inspection and be used as a standard to evaluate other non-destructive techniques. In Chapter 3, we describe a non-destructive photon migration based technique. This method produces a reliable fiber formation index that shows good correlation with those obtained from the destructive image processing method. In Chapter 4, we present a real-time implementation of the technique using a fast laser scanning system and demonstrate its online use for monitoring fiber formations in whole extrusion samples.

In the second part of the dissertation, we present results on light propagation in whole skeletal muscles, a complex and highly anisotropic biological tissue. In Chapter 5,

a three dimensional coupled wave theory is applied to investigate how light propagation in single muscle fibers is affected by different sarcomere morphologies. We demonstrated that this model can be used to explain various single muscle fiber experimental studies reported before. In Chapter 6, we describe experimental and theoretical studies of light propagation in whole skeletal muscles. We found that the diffuse reflectance on skeletal muscle surfaces has a unique pattern, which is significantly different from those reported in any other tissues. By incorporating the three dimensional coupled wave theory in a Monte Carlo model, we can successfully reproduce these unique experimental observations. In Chapter 7, we present a comprehensive study to investigate the effects of different muscle physical and physiological traits on our optical measurements.

The majority of the dissertation has been published in the following journal papers. Permissions from journal publishers are provided in the Appendix.

Ch.2: J. Ranasinghesagara, F. Hsieh, and G. Yao, "An image processing method for quantifying fiber formation in meat analogs under high moisture extrusion," *J Food Sci.*70, E450-454 (2005).

Ch.3: J. Ranasinghesagara, F. Hsieh, and G. Yao, "A photon migration method for quantifying fiber formation in meat analogs," *J. Food Sci.*71, E227-231(2006).

Ch.4: J. Ranasinghesagara, F. Hsieh, H. Huff, and G. Yao, "A laser scanning system for real-time mapping of fiber formations in meat analogs," *J. Food Sci.*, In press (2009).

Ch.5: J. Ranasinghesagara and G. Yao, "Effects of inhomogeneous myofibril morphology on optical diffraction in single muscle fibers," *J Opt Soc Am* A, 25(12), 3051–3058 (2008).

Ch.6: J. Ranasinghesagara and G. Yao, "Imaging 2D diffuse reflectance in skeletal muscle," *Opt. Express* 15, 3998-4007 (2007).

CHAPTER 2

AN IMAGE PROCESSING METHOD FOR QUANTIFYING FIBER FORMATION IN MEAT ANALOGS

2.1 INTRODUCTION

High moisture extrusion using twin-screw extruders has shown great promise for producing meat analog products with vegetable proteins. Development of non-destructive techniques to quantify textural properties of extrudates is important because visual and textural properties are the key factors for consumer acceptance. Visual examination is often used as a standard evaluation method. However, it is subjective and qualitative. Machine vision techniques are often used as a substitute for human visual inspection for automatic, quantitative, and objective measurements. In this study, we developed an image processing technique based on Hough transform (Hough, 1962) that can automatically characterize sample fiber formation using digital images. Well-defined fibers are oriented along one direction and can be approximated as linear lines. Hough transform has been recognized as one of the best methods for detecting lines and curves in discrete images. It has been implemented in machine vision systems (Leavers, 1992) for various applications such as weeding robot (Chen and others 2003), field machinery (Astrand and Baerveldt, 2005), and fruit recognition (Jimenez and others 1999). Although samples need to be peeled for better imaging inspections, our imaging analysis algorithm can be used as a standard objective method to verify new noninvasive methods. The

numerical indices obtained on sample extrusion products were compared with results measured using fluorescence polarization spectroscopy in this study.

2.2 MATERIALS AND METHODS

2.2.1 Extruder

A co-rotating twin-screw food extruder (MPF 50/25, APV Baker Inc., Grand Rapids, MI) was used in this study. It has a smooth barrel with a length/diameter ratio of 15:1. The detailed configurations of the extruder have been described previously (Yao and others, 2004). The barrel has a clam-shell design, which is segmented into five zones, and each zone consists of single heating element. The temperatures from the first zone to the fourth zone were set at 25, 36, 100 and 155˚C by using these heating elements. The last zone was varied from 165 to 182˚C. Water was injected into the extruder barrel, 0.108m downstream from the feeding port of dry mix, to provide the required moisture content (55 to 65%) for the final product. A long cooling die with a dimension of 60×10×300 mm (W×H×L) was attached to the end of the barrel and was cooled by a 50:50 mixture of cold water and ethylene glycol at 5˚C.

2.2.2 Materials

Soy protein isolate (Profam 974) was obtained from ADM (Decatur, IL); wheat gluten and unmodified wheat starch (Midsol 50) was from MGP Ingredients, Inc. (Atchison, Kans.). These raw ingredients were blended at a ratio of 6:4:0.5, using an 18.9L Hobart Mixer for 30 min to ensure the uniformity of the feeding material. Extrusion was also performed using mixture of soy protein isolate (Pro-Fam 974, ADM, Decatur, IL) and whey protein (Alacen 894, NZMP, Lemoyne, PA) with a 3:2 ratio.

2.2.3 Imaging processing

Extrusion samples were dissected by hand peeling along the direction of fiber orientation to reveal the fibrous structures. Samples were well illuminated with a high power white LED light to capture minor details of the fibrous structure. Images were acquired by a video camera (Pulnix, TM-7EX, Sunnyvale, CA) placed approximately 25cm away from the sample. A 1.9cm × 1.4cm sample area was imaged with a magnification of 0.34. All images were rescaled and saved as 320 × 240 pixel images. The image processing technique used to analyze the above images can be subdivided into four phases: pre-processing, edge detection, Hough transform, and region of interest (ROI) analysis. During the pre-processing, images with excessive background were trimmed to minimize the improper shading at boundaries. In addition, images were low-pass filtered using a 3×3 Gaussian mask with unity standard deviation to smooth out noisy pixels of high spatial frequencies. We applied the standard 3×3 Sobel gradient edge detector (Weeks Jr., 1996) to identify the changes of gray levels in the image. A global threshold was then applied to convert the image to a binary image. The threshold value was chosen as 9.4% of the maximum gradient value which was based on a rule of thumb found by Pratt (1991).

In Hough transform, all pixels in a line segment were transformed into a corresponding single point in the parametric space (Hough, 1962). A straight line can be described using the following parametric equation (Duda and Hart, 1973).

$$\rho = x\cos\theta + y\sin\theta . \qquad (2\text{-}1)$$

where (x, y) represents a pixel on this straight line in the original image; ρ is the distance from origin to this line; and θ is the angle between this line and the y-axis. The

coordinates (ρ, θ) represent the parametric space or Hough space. We selected the center of the raw image as the origin, and transformed each pixel (x, y) into the parametric space (ρ, θ) using the above equation. From Eq. 2-1, it can be seen that a line in the raw image is represented by a single point (ρ, θ) in the parametric space. The pixel value in Hough space is proportional to the length of the corresponding line in the original image. In this transformation, pixels close to the center were sampled more than those away from the center because of their non-uniform distributions in the parametric space (Leavers, 1992). In order to overcome this problem, we normalized each pixel value in parametric space by the total possible values that can be accumulated in that particular point, which is the maximum line length in the original image. It is worth noting that this procedure may provide heavily-weighted phantom pixels at the boundaries in parametric space depending on the intensity distribution of the boundaries in the original image.

In general, the θ-axis in parametric space ranges from –90° to 90° (Weeks Jr., 1996) and the 0° is located at the middle of θ-axis. In our images, fiber was oriented almost horizontally in the image so that the corresponding high intensity pixels in parametric space were always closer to ±90°. For better visualization and easy calculation process, we shifted the θ-axis by 90° to translate our region of interest (ROI) to the center of the parametric space. For samples with good fiber formations, the raw images had alternative high and low intensity regions in a more uniform manner; while for samples with poor fibrous structures, the band structures were not significant in the raw images. When these images were Hough-transformed, the alternative high and low intensity regions were aligned along the ρ direction, which led to a highly varying gradient distribution in the parametric space. To characterize this effect, we used Sobel gradient edge detection on

Hough-transformed images and standardized the grey levels between 0 and 1. When a higher gradient value was present, the edge detection produced a higher pixel value. The majority of pixels in this edge detected image was not corresponding to fiber structures in the original image, and thus had low pixel values. To enhance the image for further processing, we applied a threshold that only kept a small percentage (2%) of the total pixels with high pixel values.

We can define a rectangular ROI from an edge detected binary image depending on ρ and θ values in the Hough space. In this ROI, the height $\Delta\rho$ is determined by the size of y-dimension in the original image. Because the boundary pixels may have incorrect values due to the normalization process described above, the top and bottom boundary pixels were excluded from $\Delta\rho$. The width $\Delta\theta$ is determined by the possible variations in fiber orientations. Although the sample's fiber orientation was always aligned with the extrudate moving direction, it may not be aligned with the x-axis of the raw image due to errors introduced when acquiring samples and taking the digital image. After analyzing large number of well defined fiber samples, we determined that a width of 30° was large enough to tolerate such variations.

In ROI, the distribution of pixels along the ρ axis is proportional to the fiber distribution along the y-axis in the original image. ROI can be divided into small cells to represent fiber distribution along the y-axis. The cell size was chosen to contain sufficient data to reflect the information in spatial distribution. We applied a moving average filter of size 2 to reduce noise in the data set (Gonzalez and Wintz, 1987). In other words, the effective cell, R_1, $R_2 \ldots R_n$, was constructed from the summation of two neighboring cells. The area of each effective cell was equal to $\Delta\theta \times (\rho_{i+2} - \rho_i)$ as shown in Fig 2-1.

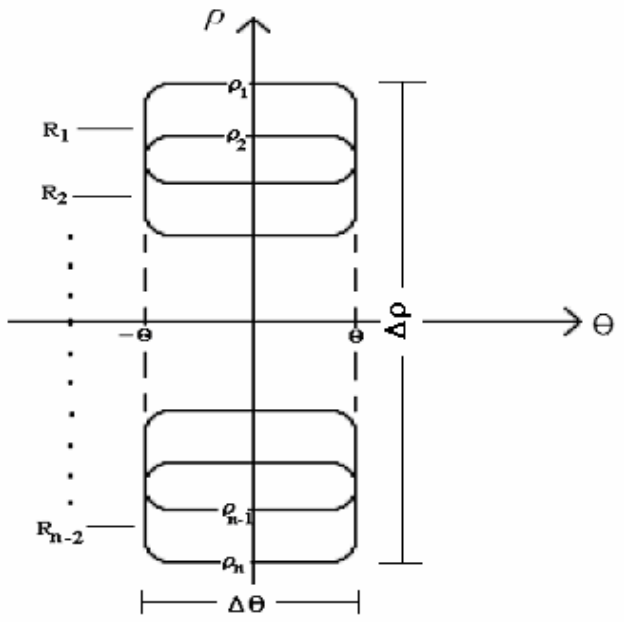

Fig. 2-1. Different cells defined in the region of interest (ROI).

When intensity of the pixel is represented by $Z(\rho, \theta)$, T_i provides the sum of all the pixels in the cell R_i:

$$T_i = \sum_{\rho_i}^{\rho_{i+2}} \sum_{-\theta}^{\theta} Z(\rho, \theta) \tag{2-2}$$

where *i = 1,2,....,n-2*. When more "high" pixels are present in all cells, the mean value of the cells $\mu(R)$ is higher. The standard deviation of all cells $\sigma(R)$ estimates the intensity distribution among those cells. When fiber distribution is uniform, the relative standard deviation (ratio of standard deviation and mean value) provides a lower value; and when distribution is non-uniform, relative standard deviation provides a higher value. A fiber index (Fitzgibbon and others 1999) was calculated as the inverse of the relative standard deviation of all cells:

$$FI = \frac{1}{\text{Relative Std. Deviation}} = \frac{\mu(R)}{\sigma(R)} \tag{2-3}$$

2.2.4 Fluorescence polarization measurements

The experimental setup has been reported previously (Yao and others, 2004). Briefly, a polarized UV light at 375nm was used to illuminate the sample and produced a broadband fluorescence light. The fluorescence light intensities at 540nm were measured at two orthogonal polarization directions, and the polarization degree was calculated as:

$$P = \frac{I_{\perp} - I_{//}}{I_{\perp} + I_{//}} \tag{2-4}$$

where $I_{\perp}$ is the fluorescence intensity with polarization perpendicular to the incident polarization direction, and $I_{//}$ is the fluorescence intensity with polarization parallel to the incident polarization direction. The measured fluorescence polarization degree was higher for samples with good fiber formation.

2.3 RESULTS AND DISCUSSION

Figure 2-2 shows the image processing process for two sample images. Both samples were extrusion products using a soy protein isolate mixture with 60.11% moisture content. Sample A was an extruded product and showed good fiber formation. Sample B was obtained at an early screw stage during a "dead-stop" run and showed bad fiber formation. The fibrous structures were easily identifiable in sample A as stripes with interleave high and low intensities. The raw images were cropped to 280×180 to remove excessive background and Sobel edge detection was applied. Edge detection can signify the structure variations in the images and remove the slow intensity variations caused by potential inhomogeneous illumination (Ritter and Wilson, 1996). A global threshold of 9.4% of the maximum grey scale was then applied to convert the image into a binary image.

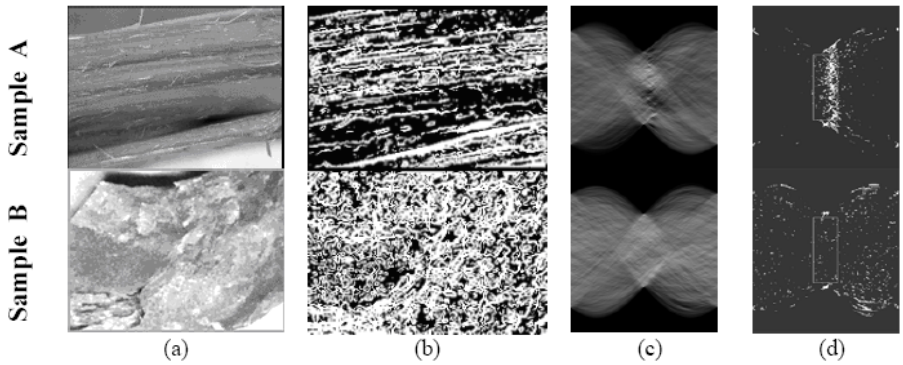

Fig. 2-2. Different stages of this image processing algorithm. (a) Original images; (b) after edge detection; (c) after Hough transform; (d) calculation of region of interest.

It can be seen from Fig. 2-2b that the fibrous structures were preserved in the forms of lines for sample A while the image looked noisy and irregular for sample B. Hough transform was then performed on these binary images. The size of the Hough image was 400×360 in ρ and θ directions. Due to those binary lines in sample A, there were high intensity pixels presented around middle axis of Hough space (Fig. 2-2c). On the contrary, sample B was rather uniform in Hough space. Sobel gradient edge detector was then applied to the Hough transformed images and a threshold was set to extract the 2% pixels with the highest intensities by analyzing the cumulative image histogram (Fig. 2-2d).

We chose a ROI (the boxes in Fig.2d) with an area of 160×60 pixels, in which Δρ was selected as 160 pixels (-80 to 80) to exclude 10 pixels at both top and bottom boundaries, and Δθ was selected as 60 pixels (-15° to 15°). The maximum height in the central region (θ=0°) was determined by the height of the cropped raw image which was 180 pixels. In order to divide this ROI into small cells for statistical analysis, a step size of 10 pixels was chosen. Because there were 160 pixels along the ρ-axis in ROI, a total of 16 cells were obtained. Considering a moving average filter of size 2 was used, the effective height of each cell was 20 pixels. After cells were selected (Fig. 2-1), the sum of

the all binary values in each cell was stored in a one dimensional array for statistical analysis.

Fiber indices were calculated using the inverse of the relative standard deviation according to Eq. 3. Samples with good fiber formation had high average intensity and low standard deviation, which led to a higher fiber index.

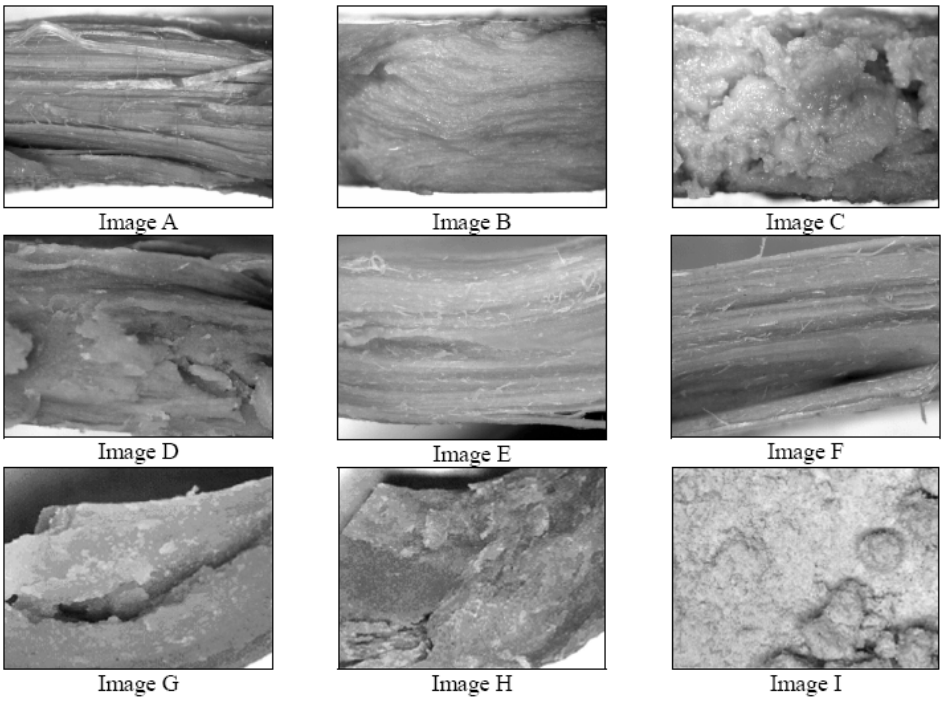

Fig. 2-3. Digital images of extrusion samples.

We compared the calculated fiber index with the result measured using fluorescence polarization spectroscopy (Yao and others, 2004) on 9 extrusion samples obtained at different extrusion conditions. The acquired digital images are shown in Fig. 2-3. Images A to C represent extrusion products using a combination of soy protein isolate and whey protein concentrate with a concentration ratio of 3:2. The barrel temperature was 160°C and moisture contents were 60, 65, and 70% (wb) for images A, B, and C, respectively. Images D and E represent extrusion products using a mixture of soy protein isolate,

wheat gluten, and unmodified wheat starch at a ratio of 6:4:0.5. The corresponding moisture contents were 66.8 and 60.1 % (wb) for images D and E, respectively. Images F to I represent samples collected at different extruder barrel stages during a dead-stop run when producing sample E. They were collected from die area (F), Zone-4(G), Zone-3(H), and Zone-1(I).

The correlation between these two methods is plotted in Fig. 2-4. It can be seen that the non-destructive fluorescence polarization index showed high correlation with this direct imaging processing results.

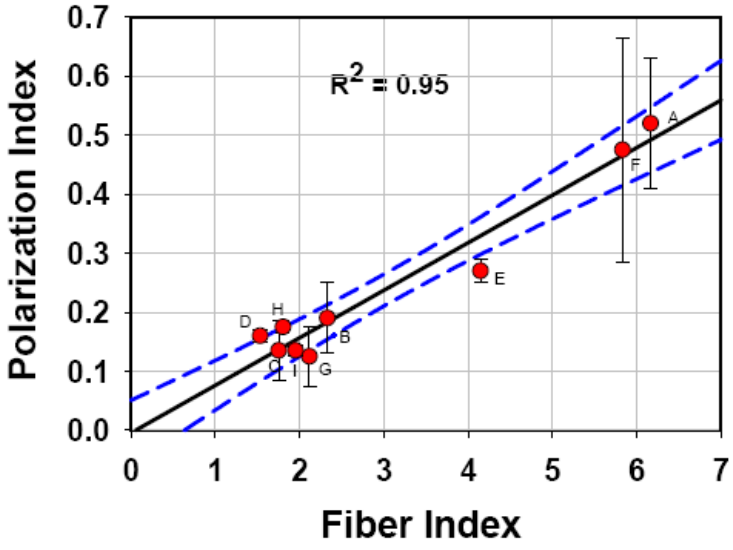

Fig. 2-4. Correlation of fluorescence polarization index and fiber index with 95% confidence interval.

The objective of using high moisture extrusion is to manufacture vegetable proteins into meat analog products such as chicken breasts. As an interesting comparison, we measured fiber index on three cooked real chicken breast samples and obtained a value of 6.15±2.09. This value was a little better than those measured from extrusion samples A and F.

It is worth pointing out that one of the critical criteria for effective edge detection is the threshold selection. Although many threshold selection methods are available (Sezgin and Sankur, 2004), not all of them are suitable for every application. The fixed global threshold method, which uses a single fixed threshold value to classify image pixels from background, is commonly used in image processing. Threshold selection depends on various factors, such as ambient illuminations; busyness of gray levels within the object and its background; inadequate contrast; and object size (Sezgin and Sankur, 2004). If we can keep all environmental conditions constant, fixed global threshold can be used without any change. Our results indicated that the 10% "rule of thumb" threshold for edge detection (Pratt, 1991) can be successfully applied and produced very stable results. In fact, any fixed threshold values from 8.5% to 11% of the maximum grey scale provided higher than 0.9 of correlation coefficient with fluorescence polarization data (Fig. 2-5A).

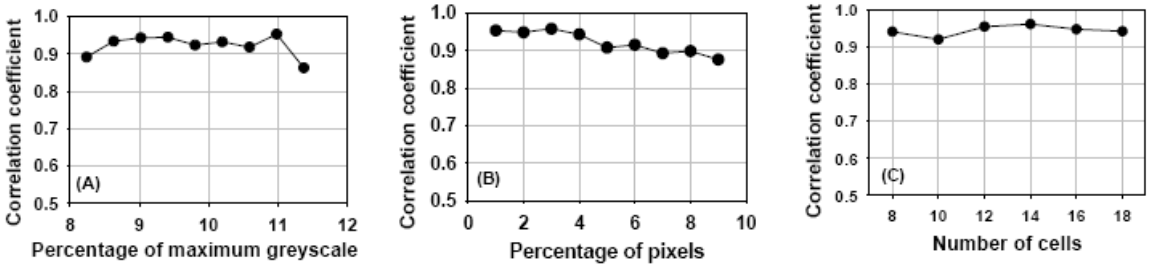

Fig. 2-5. Correlation coefficients obtained with (A) different threshold values of edge detected raw images; (B) different threshold values of Hough transformed images; and (C) different number of cells in ROI.

Selecting threshold based on cumulative histogram is another often applied method (Russ, 2005). In this method, the threshold value is determined as the pixel value that is greater than pixel values of a certain percentage of the total pixels. Threshold of 98% of cumulative histogram percentile was chosen for Hough transformed images in this study

to select the 2% pixels of the highest intensities. This value was chosen based on the observation that the sample's fiber orientation was always aligned with the extrudate moving direction with small angular tolerance, which implied that in Hough space, the pixels corresponding to fiber structures occupied a small region. If the angular tolerance is approximately ±5°, the number of pixels within such a small region was about 2% of the total pixels in Hough space. As shown in Fig. 2-5B, any values between 1% and 4% produced similar correlation coefficient with fluorescence measurements.

As discussed before, the area of ROI was chosen based on the size of the raw image and a prior knowledge about the fiber orientation in extrudates. The number of small cells within ROI was chosen to allow both enough data points for statistical analysis and larger enough cell size to smooth out noise induced variations. A size 2 moving average filter was used to further reduce noise. Fig. 2-5C shows that cell numbers from 8 to 18 produced similar correlation coefficient with fluorescence measurements.

2.4 CONCLUSION

It is a very important task to assess fiber formation in extruded products under high moisture. We have developed an image processing method that can compute the sample fiber index directly from digital images. This technique is based on Hough transform and statistical analysis of the region of interest. Our studies indicated that this method can provide highly dependable results to differentiate the structures with well defined fiber formation from the structures with poor fiber formation. This objective method provides a quantitative index by direct measurements on extrusion products. Therefore it can be used to replace the often used visual inspection method. Although samples need to be dissected to better reveal the fiber formations in digital imaging, this method can be used

as a standard quantitative method for evaluating other non-invasive methods. Sample fiber formation evaluated by a non-destructive fluorescence polarization method was compared with results obtained from this image processing method and showed excellent correlation.

CHAPTER 3

A PHOTON MIGRATION METHOD FOR CHARACTERIZING FIBER FORMATION IN MEAT ANALOGS

3.1 INTRODUCTION

High moisture (40-80%) extrusion products resemble chicken or turkey breast meat (Lin and others 2000; 2002). In Chapter 2, we discussed an image processing method based on Hough transform to assess fiber formation in extruded soy protein products. However, this method still requires preprocessing of samples before analyzing. Such deficiency is neither convenient nor practical for online monitoring.

In recent years, photon migration techniques using visible to near infrared wavelengths have found widespread applications in analysis of different material structures (Raghavachari, 2001). When light propagates in a turbid media, it is absorbed and randomly scattered. Eventually, some light escapes from the sample surface and is measured as the optical reflectance. Those scattered photons carry vital information about optical properties of the media which can be derived from reflectance measurements based on light transportation theories. In extruded protein products, the high temperature, pressure and shear during the extrusion process promote the formation of fibers (Luping, 1993). As a result of the high shear rate, most of the fibers are aligned along the direction of propagation in the cooling die. Therefore the final extruded product has a well defined anisotropic structure under optimal operation conditions. The continuous time random

walk (CTRW) theory (Weiss, 1994; Weiss and others, 1998) has been used to study the complicated process of light transportation in scattering media. Dagdug and others (2003) have recently extended the CTRW theory to analyze the light interactions with anisotropic turbid media. This method has been successfully applied in studies of various anisotropic tissue structures (Sviridov and others, 2005).

In this chapter, we explored the possibility of applying the anisotropic CTRW model in characterizing fiber formation in high moisture extrusion. An image processing method was developed to extract sample anisotropy properties from optical reflectance images measured on extruded samples, directly from the extruder. The results had a good correlation with those measured on peeled extruded samples using a Hough transform based imaging technique (Ranasinghesagara and others 2005).

3.2 MATERIALS AND METHODS

3.2.1 Materials

We used two different mixes of raw materials in this study. Mix #1 consists of 30% soy protein isolate (Profam 974, ADM, Decatur, IL), 30% defatted soy flour, 35% wheat gluten (MGP Ingredients, Atchison, KS), and 5% wheat starch (MGP Ingredients, Atchison, KS). In Mix #2, 30% defatted soy flour was replaced by soy protein isolate which was increased to 60%. The mixtures were extruded at different moisture contents (55% ~ 65%) and temperatures (165˚ ~ 182˚C). Two samples from each extrusion batch were acquired to be analyzed for each test. All imaging measurements were conducted at room temperature. A total of 40 samples were used (Table 3-1).

Table 3-1. Feed moisture contents and extrusion temperatures

Mix	Moisture (%)	No. of samples		
		T = 165˚C	T = 174˚C	T = 182˚C
#1	55	-	4	-
	65	2	4	4
#2	55	4	2	2
	60	2	4	4
	65	2	4	2

3.2.2 Imaging system

The experimental set up shown in Fig. 3-1 was used to measure optical reflectance images. A red LED (λ=680 nm) was used as the light source. The light was coupled into an optical fiber (400 μm in diameter) and delivered upon the sample at an angle of α=45˚ with the vertical axis. The fiber was not in touch with the sample. The sample was placed on a sample holder such that the extrusion direction was approximately parallel to the direction of the light fiber. A 12-bit digital camera (DALSA DS-21-01-M60-11E, Waterloo, Ontario, Canada) was mounted above the sample and the light incident location was approximately at the middle of the image. The acquired backscattered reflectance images were grabbed into a personal computer via a Camera Link® frame grabber (Solios XCL, Matrox Inc., Canada) for further processing.

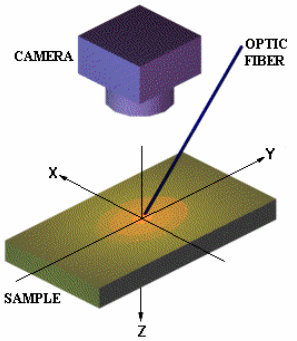

Fig. 3-1. Experimental set up for image acquisition

The camera lens magnification was set to 0.63. The image resolution was calibrated to be 18.9 μm/pixel. The amount of noise which is known as dark current (Mullikin and others 1994) was recorded for each measurement and subtracted from the image. To improve signal-to-noise ratio, ten images of the same sample were continuously acquired and averaged. Because the incident light on the sample surface was very low (120 μW) in the present system, we covered the system with black cardboard to block the ambient light throughout the procedure. In the future development, a high power light source such as a laser at near infrared region will be used to eliminate the necessity of blocking the ambient light.

Oblique incident scheme was used in this study in order to minimize the image obstruction from the incident optical fiber. As we were considering intensities far away from the incident point, effect of the oblique incident on light reflectance was insignificant. We verified this by performing measurements at different angles on anisotropic extrudates and did not observe any significant changes in the results. The reflectance profile of IntraLipid (IntraLipid™ 20%, Kabi Pharmacia Clayton, NC), which is a milk like lipid solution and is known to be isotropic, was recorded to verify the linearity of the CCD array. Results indicate that the imaging system had excellent linearity over a broad range of intensities.

3.2.3 Image Analysis

Image analysis was based on the anisotropic light propagation method based on CTRW theory discussed in Sec 1.2 of Chapter 1. An image processing algorithm was developed to measure the bias parameter B from the measured reflectance images. The reflectance image was stored as a 1024×1024 array and pixel locations were transformed

to the Cartesian coordinate system (Fig. 3-1) with the incident location chosen as the origin. The small area of the image obstructed by the incident optical fiber was removed from all images. First, a point on the x-axis was selected and its pixel intensity was used to find all image pixels with the same intensity. In order to compensate for intensity variations caused by noise, a ±1% margin was allowed when searching for these pixels. The corresponding n equi-intensity pixels were identified and their locations, (x_1, y_1), (x_2, y_2) ….. (x_n, y_n) were stored in an array. Then the direct least square error ellipse fit (DLSEEF) technique (Fitzgibbon and others, 1999) was applied to find the best fit ellipse. The general polynomial equation for a conic in (x, y) plane is given by:

$$G(\vec{\mathbf{p}}, \vec{\mathbf{u}}) = \vec{\mathbf{p}}\,\vec{\mathbf{u}} = ax^2 + bxy + cy^2 + dx + ey + f = 0 \qquad (3\text{-}1)$$

where vector $\vec{\mathbf{p}}$=[a, b, c, d, e, f]^T, vector $\vec{\mathbf{u}}$=[x^2, xy, y^2, x, y, 1], and a, b, c, d, e, f are conic parameters. The quantity $G(\vec{\mathbf{p}}, \vec{\mathbf{u}})$ represents the algebraic distance from a point (x, y) to the given conic. The fitting of a general conic can be approached by minimizing $\sum_{i=1}^{n} G_i(\vec{\mathbf{p}}, \vec{\mathbf{u}})^2$, which is the sum of algebraic distances from all the equi-intensity points to the conic. In order to ensure that the conic is an ellipse, the constraint condition of $4ac - b^2 = 1$ needs to be applied. After the conic parameter $\vec{\mathbf{p}}$ is obtained from the fitting, the azimuth angle (θ) or tilt angle of the ellipse is derived as,

$$\theta = \begin{cases} \dfrac{\pi}{4} & if \;\; a = c \\ 0.5\tan^{-1}\left(\dfrac{b}{a-c}\right) & \text{otherwise} \end{cases} \qquad (3\text{-}2)$$

And the bias parameter B can be calculated by using following equation:

$$B = \left(\frac{L_L}{L_S}\right)^2 = \frac{K(dCos\theta + eSin\theta)^2 + (-dCos\theta + eSin\theta)^2 - 4f}{(dCos\theta + eSin\theta)^2 + \frac{1}{K}(-dCos\theta + eSin\theta)^2 - 4f} \tag{3-3}$$

where the parameter K is calculated from the conic parameters:

$$K = \frac{aSin^2\theta - bSin\theta Cos\theta + cCos^2\theta}{aCos^2\theta + bSin\theta Cos\theta + cSin^2\theta} \tag{3-4}$$

The fitting error can be estimated using the average of the algebraic distance from all data points to the fitted ellipse:

$$\frac{1}{n}\frac{1}{L_L L_S}\sum_{i=1}^{n} G_i(\vec{\mathbf{p}}, \vec{\mathbf{u}}_i)^2 \tag{3-5}$$

where n is the total number of data points used in the fitting, and the term $L_L L_S$ accounts for the size of the ellipse. Obviously, the error is zero if all the points are on the ellipse.

3.3 RESULTS AND DISCUSSION

Fig. 3-2 demonstrates the image processing for three different samples: an isotropic medium (IntraLipid), an extrudate of poor fiber formation, and one with well formed fibers. Digital images of the extrudates were also shown (Fig. 3-2a) for reference. The extrudate surface was peeled by hand when taking these digital images to better expose their internal structures. As expected, for all IntraLipid samples of different concentrations, the B values remained close to one (1.01±0.01) because the equi-intensity profiles were circles for isotropic samples. Fig. 3-2 also indicates that the highly organized fibrous structure has a higher B value than that of poorly organized structures.

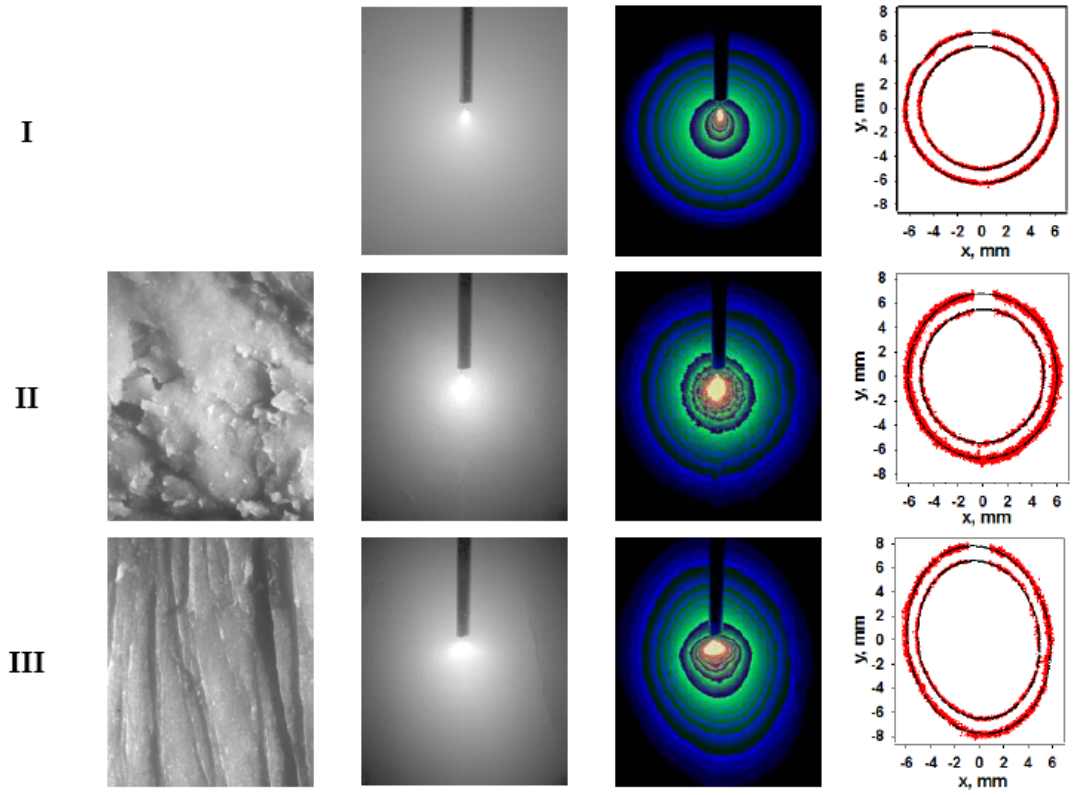

Fig. 3-2. Sample images of (I) IntraLipid solution (2.28%, B=1.01), (II) extrusion samples with limited fiber formation (Mix#2, T:165˚C, M:65%, B=1.22), and (III) extrusion samples of good fiber formation (Mix#2, T:182˚C, M:55%, B=1.77). (a) surface peeled images; (b) regular reflectance images (log scale); (c) pseudo color reflectance images that show the equi-intensity profiles; (d) elliptical fitting (solid lines) of the equi-intensity contours at 5.0 mm and 6.0 mm.

According to the CTRW theory, optical scattering depends on the transitional probabilities of scattering along x and y direction. When fiber formation is high, the transition probability along the fiber direction is greater than that along the direction perpendicular to the fiber. As a result, probability of scattering along the fiber direction is smaller than that along the perpendicular direction. Photons undergoing less scattering reach longer distances, which leads to a reflectance ellipse with major axis oriented in fiber formation direction. For samples with less fiber formation, the transition probabilities are nearly isotropic, which leads to a circular reflectance profile. We also

conducted tests on raw materials and obtained circular reflectance profiles as expected.

Fig. 3-3 shows examples of B values calculated for equi-intensity curves at different distances from the incident point. The B values of ellipses close to the incident point was not stable (Fig. 3-3a) because the photons near the incident carry information mostly about the surface layers. Having only a few scatterings, these photons were unable to provide the global information of the underlying structure and were subject to the effects of initial incident conditions. However, photons that were detected far away from the incident underwent multiple scattering and carried vital information about the anisotropy of the medium.

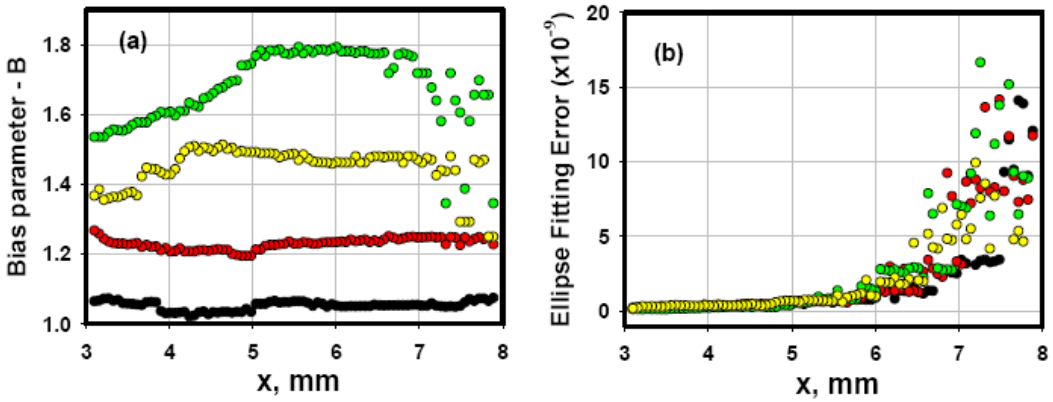

Fig. 3-3. (a) Bias parameter values as a function of distance to the incident point along x-axis; and (b) the corresponding fitting errors calculated using Eq. 9. Four extrusion samples of various degrees of fiber formation were used in the example.

It can be seen in Fig. 3-3a that the locations where the bias parameter stabilizes depend on the actual fiber formation. Samples of little fiber formation gave small yet consistent B values from a distance less than 3 mm from the origin; whereas samples with well formed fibers had very stable B values from ~ 5 mm away from the light incident point. For regions beyond ~6.5 mm from the origin, the results were noisy because the reflectance decreased with the distance to the incident location (Fig. 3-3b).

The final B value for each sample was determined by averaging all individual B values calculated from 5 to 6 mm.

The calculated bias parameter B has a good match with visual inspections. In order to provide a quantitative assessment of this technique, we compared the B values with the fiber index measured directly from peeled samples using an image processing algorithm reported previously (Ranasinghesagara and others, 2005). After reflectance imaging measurements, the extrusion samples were hand peeled to reveal the internal fibrous structures. Digital images of peeled samples were then acquired and analyzed using the Hough transform based processing method that can quantify fiber formations.

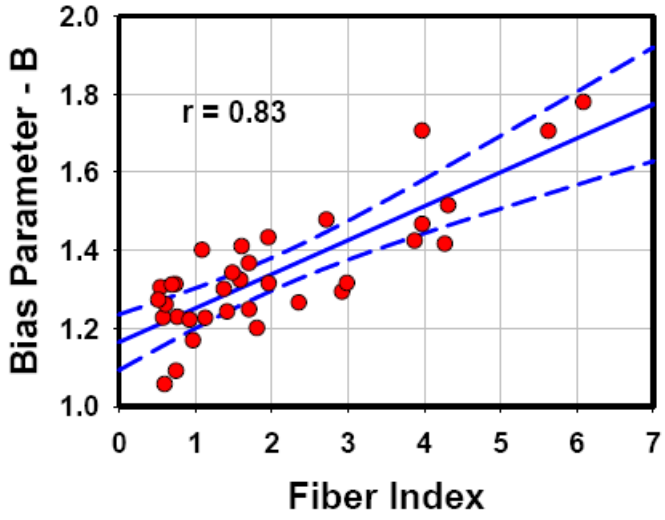

Fig. 3-4. Correlation between the bias parameter B and the fiber index.

It was noticed that sample preparations using hand peeling sometimes introduced variations in the fiber index calculations. To improve the tolerance of such variations, we modified the previous algorithm (Ranasinghesagara and others, 2005) by using the pixel cluster density (Theodoridis and Koutroumbas, 2003) instead of average pixel values in the region of interest (ROI) analysis. Fig. 3-4 shows that a good correlation exists

between the bias parameter and the fiber index. It is worth pointing out that the current photon migration method is non-contact and non-destructive. It does not need sample preparation and all measurements are conducted directly from the sample surface.

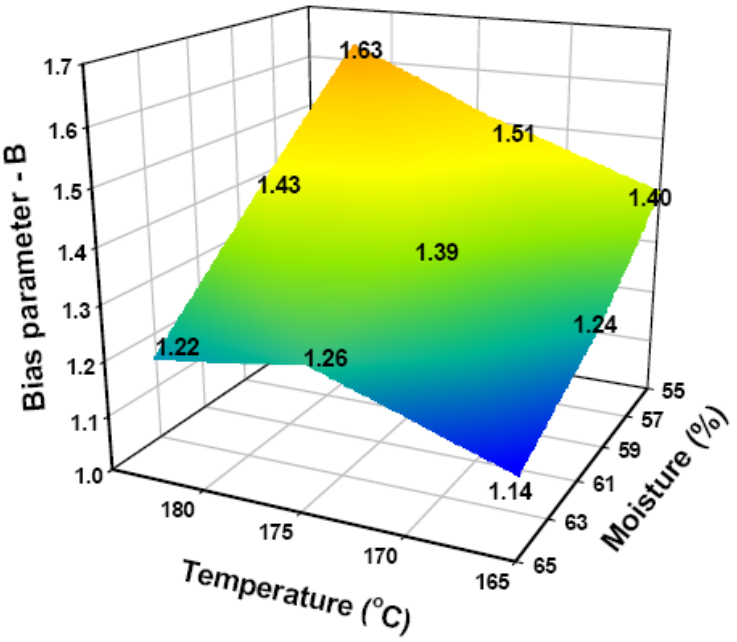

Fig. 3-5. Averaged bias parameter values at different extrusion temperatures (˚C) and moisture contents (%). Mix #2 was used as raw material.

In high moisture extrusion, the main factors affecting fiber formation are temperature, moisture and the type and proportion of raw materials. Fig. 3-5 illustrates the effect of temperature and moisture on the fiber formation in Mix #2. When moisture content was high, water served as a lubricant, which reduced the friction between extruded materials and both screw and cooling die (Lin and others 1997). As a result, less fiber was formed in the extruded products. On the other hand, a higher temperature leads to a highly organized structure (Lin and others, 2002). There effects were confirmed in this study by B values measured at different extrusion conditions (Fig. 3-5). Even though products extruded at higher temperature and lower moisture conditions have the best fiber

formation; their color appearance (dark brown) is usually not visually attractive. On the other extreme, products extruded at lower temperature and higher moisture conditions have a mushy structure with very little fiber formation. Therefore, it is important to find an optimal extrusion protocol that can produce final products with both good texture properties and attractive appearance.

3.4 CONCLUSION

We developed a technique for assessing the fiber formation in the high moisture extrudates based on an anisotropic photon migration model. Backscattered reflectance images from extruded samples were acquired. And the bias parameter was obtained by numerically fitting the equi-intensity reflectance profiles. The calculated bias parameter had a good correlation with the degree of fiber formation in extrudates. This method is simple to implement and the results have good immunity to light incident angle. The reflectance profile is not affected by the incident light intensity as shown in Eq. 1-2. No sample preparation is required during the measurements. This method can be used as a rapid assessment tool assisting the search for optimum extrusion temperature and moisture conditions which can provide good texture and fiber formation for different raw materials. More importantly, it has a potential to be used as a real time quality control and assurance device for products having fibrous structure in an industrial setting.

CHAPTER 4

A LASER SCANNING SYSTEM FOR REAL-TIME MAPPING OF FIBER FORMATIONS IN MEAT ANALOGS

4.1 INTRODUCTION

We have developed a nondestructive method to detect fiber formation in meat analogs by measuring the optical reflectance pattern at the sample surface in Chapter 3. This photon migration based method provides a reliable measure of the actual fiber formation. This technique is fast and non-invasive, thus is ideally positioned for online monitoring of fiber formation in soy meat analogs.

In this study, we further advanced this technology by implementing it in a fast laser scanning system. The LED light source and the optical fiber described in our previous study (Ranasinghesagara and others 2006) was replaced by a laser to increase the incident light intensity. This new implementation allows a two-dimensional mapping of the fiber formation and orientation in the entire sample in real time. The system has been tested on extrusion products produced from the high moisture extrusion facility in the food engineering lab at the University of Missouri.

4.2 MATERIALS AND METHODS

4.2.1 Materials

The extruder and extrusion conditions were similar to those described in our

previous study (Yao and others, 2004). A co-rotating, twin-screw food extruder (MPF 50/25, APV Baker Inc., Grand Rapids, MI) with a smooth barrel and a length/diameter ratio of 15:1 was used to produce extrusion samples. The barrel was sectioned into five temperature zones and each zone was heated with an electric cartridge heating system. A long cooling die was mounted at the end of the barrel and was cooled by a 50:50 mixture of cold water and ethylene glycol at 5°C.

We used two different raw mixtures in this study. The raw materials used in mix #1 were 85% soy protein isolate (Profam 974, ADM, Decatur, IL) and 15% wheat starch (MGP Ingredients, Atchison, KS). In mix #2, the amount of soy protein isolate was decreased to 57% and the wheat starch was decreased to 5%. In addition, 38% wheat gluten (MGP Ingredients, Atchison, KS) was added to the mix. All mixtures were extruded at 165°C with 60% and 70% (wb) moisture contents in the aforementioned high moisture twin screw extruder.

4.2.2 Scanning system

A schematic illustration of the scanning system is shown in Fig. 4-1. A non-polarized He-Ne laser (10 mW, 633 nm) was used as the light source. The incident beam was slightly focused by a focusing lens (f = 450 mm), to provide a small beam size on the sample surface. The laser beam was redirected by a reflection mirror to a galvanometer scanner (M2, General Scanning, Billerica, MA) after passing through a small aperture (1.0 mm) at the center of the imaging mirror #4. The incident light was scanned across the extrusion sample by rotating the galvanometer. The beam diameter of the incident laser beam is ~ 1mm at the sample surface. The diffusely reflected light from the sample was redirected by the scanning mirror and the imaging mirror #4 before being captured

by a CCD camera (DALSA DS-21-01-M60, Canada). A 2×2 binning was applied to capture a 512×512 12-bit image. The image was acquired by a frame grabber (Solios XCL, Matrox Imaging, Canada) and stored in a two dimensional array in the memory for further processing. A band-pass optical filter at 633 nm (bandwidth = 2.4nm, N47-494, Edmund optics, Barrington, NJ, USA) was incorporated inside the imaging lens of the CCD camera so that the room light has little effect on the acquired images. The spatial resolution of the imaging system for both the x- and y-axis is 96μm/pixel. The optical system was carefully adjusted to ensure alignment.

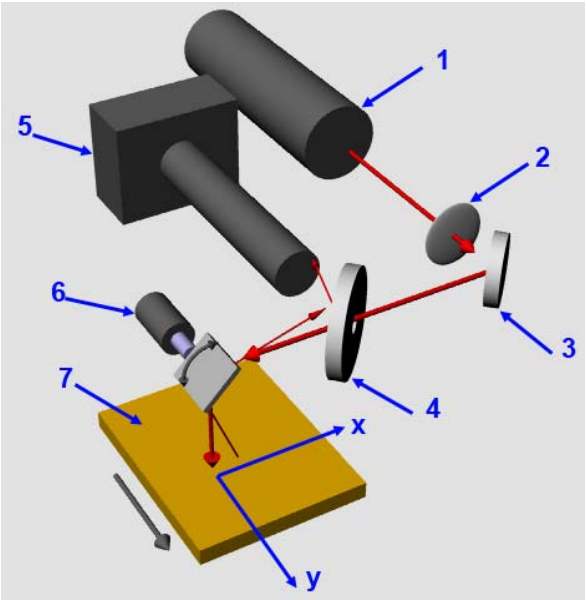

Fig. 4-1. Schematic of the scanning system. 1: laser; 2: focus lens; 3: reflection mirror; 4: mirror with a center hole; 5: camera; 6: scanning mirror; 7: extrusion sample out of the die.

A coordinate system was defined so that the extruder axis was along the y-axis and the extrudates moved at a constant speed along this direction. At the beginning of each scan, the galvanometer was set at the boundary of the sample and then moved along the x-axis toward the other side (Fig. 4-2). When reaching the sample boundary, the galvanometer was stopped and moved backward toward the initial position. This process

was repeated until the system was stopped by the operator via a software interface. Considering the extudate's linear movement, two different scanning modes can be realized: the zig-zag and parallel scan. A zig-zag scan is formed when image acquisition takes place during both forward and backward scanning so that the scanning trajectory forms a zig-zag pattern on the sample surface. A parallel scan is achieved if the image is acquired only during the forward scan and the scanning locations form a series of parallel lines at the sample surface.

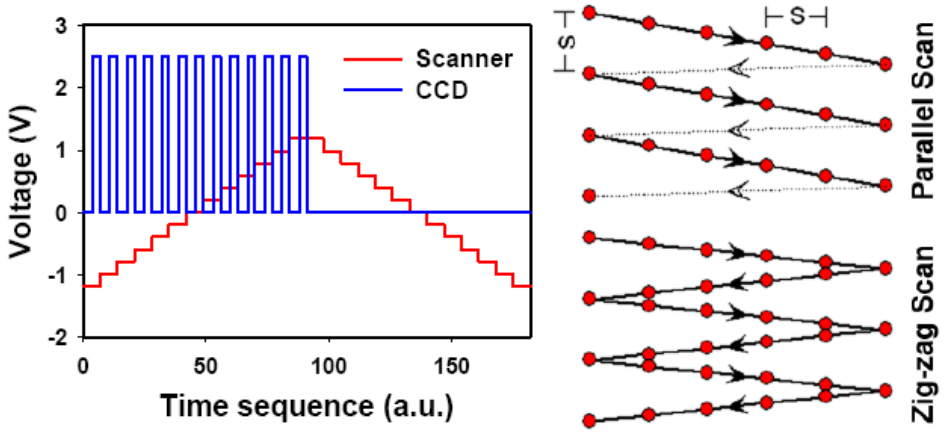

Fig. 4-2. Signal sequences for synchronizing the optical scanner and the CCD camera for one scan cycle. A parallel scanning sequence was illustrated, where the CCD is triggered only during the forward scanning. For a zig-zag scanning, the CCD is triggered during both forward and backward scanning. The scan patterns are also shown with circles representing scanning points on the sample.

It can be seen in Fig. 4-2, that a zig-zag scan provides additional scans between two parallel scans although the spatial locations of the sampling locations are not evenly distributed. Therefore, the fiber formation images can not be constructed from a zig-zag scan as straightforward as from a parallel scan. All results described below were obtained by using parallel scans.

The scan angle of the galvanometer is directly proportional to the applied voltage. The camera and the scanner are synchronized using two signal sequences generated from

a signal generation board (PCI-6221, National Instruments, Austin, TX). The first signal is a TTL sequence that triggers the frame grabber. For a parallel scanning, the frame grabber is only triggered during the first half of the scan cycle as shown in Fig. 4-2. But it is continuously triggered during a zig-zag scanning pattern. The second signal produces discrete voltages to move the scanner. If the distance from the scan mirror to the sample is L, the step angle ($\Delta\theta$) of the scanner can be calculated as:

$$\Delta\theta = \tan^{-1}\left(\frac{s}{L}\right) \tag{4-1}$$

where s is the scanning spatial resolution or the distance on the sample surface between two consecutive scanning points. The step voltage increment/decrement (ΔU) required to produce a $\Delta\theta$ can be calculated as:

$$\Delta U = \frac{\Delta\theta}{G} \tag{4-2}$$

where G is the responsivity of the scanner in deg/V. The maximal image acquisition speed of the system is automatically adjusted in the control software based on specified scanning spatial resolution (s), extrusion speed (v), and scanning width (d). The total number of scanning points (N_{line}) within a single scanning line is calculated as:

$$N_{Line} = \frac{d}{s} \tag{4-3}$$

where the scanning width d is usually a little smaller than the sample width to avoid any boundary effects.

In a parallel scanning, the scanner is set to complete one full cycle when the extrusion sample progresses a distance similar to the scanning spatial resolution s. In other words, the scanner has moved a total of $2\times N_{line}$ points when the sample has moved

a distance of s. Therefore the frequency of the signal (f_{Signal}) generated to drive the galvanometer is

$$f_{Signal} = 2 \times N_{Line} \times \frac{v}{s} = \frac{2dv}{s^2} \tag{4-4}$$

where v is the extrusion speed. The signal generation frequency should be smaller than the camera frame rate ($f_{Signal} \leq f_{Rate}$) to avoid any missing frames during the scanning. Since the small step response time of the scanner is less than 400 μs and the image processing takes 3~5 ms, the image acquisition speed in our system is limited by the frame rate of the camera which is 60 Hz. The actual image acquisition speed used for this study was 20 Hz because the extrusion speed was 10 mm/s, the sample width was 60 mm, and the scanning spatial resolution was 7 mm.

4.2.3 Calculation of the fiber formation

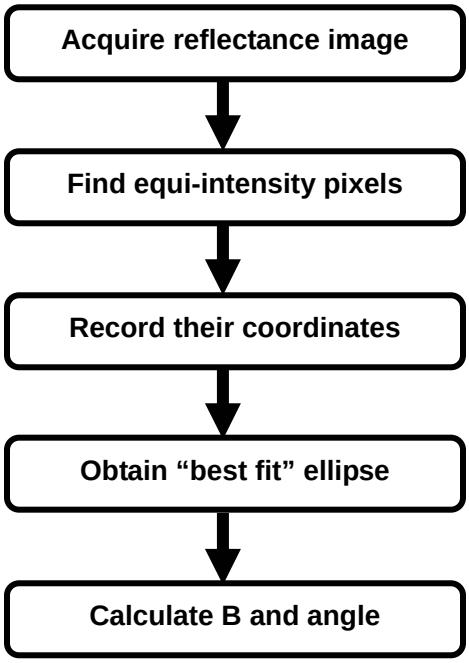

Fig. 4-3. Image and data processing procedures.

Fig. 4-3 shows the image and data processing sequence. When triggered, the camera captured the optical reflectance image which was stored in a temporary array. Predefined pixel intensity was applied to extract all image pixels with similar intensities. A ±2% intensity margin was used in the study during the pixel search to compensate for intensity variations.

The direct least-square-error ellipse fitting method (Fitzgibbon and others, 1999) was then applied to obtain the best-fit ellipse for those extracted pixels. A complete set of ellipse parameters such as the center coordinates, length of axes, and the ellipse orientation angle (relative to the y axis) was obtained. The Bias parameter B is calculated as

$$B = \left(\frac{L_L}{L_S} \right)^2 \tag{4-5}$$

where L_L and L_S are the long and short axes of the best fit ellipse. The calculated B parameter and orientation angle were displayed in real time in the software. As shown in our previous studies (Ranasinghesagara and others, 2006), the B parameter has a good correlation with the degree of fiber formation. A larger B parameter indicates samples with better fibrous structures; while a B parameter close to 1.0 indicates samples with no fiber formation. The long axis of the ellipse indicates the fiber orientation. Ideally, the fiber formation is aligned with the extrusion direction (the y-axis in Fig. 4-1). Therefore, quantitatively, the fiber orientation angle α, is defined as the angle between the y axis and the long axis of the ellipse. For a sample with uniform fiber formations along the extrusion direction, α is close to zero degree.

4.2.4 Two-dimensional mapping

Once the B parameters and orientation angles were obtained for all scanning positions, these values were used to construct two dimensional maps. The measurement results were organized in a two dimensional array based on the original measurement locations. A pseudo-color coding was used to display B values. In other words, a different color was used to represent a different B value. To display fiber orientations, a vector map was used. A small arrow was drawn at each scanning point and the arrow head represented the fiber orientation. The two maps of the fiber formation and fiber orientation were co-registered based on the locations of the scanning point. Since the sample was moving during the scan, the calculated two dimensional maps were slanted. These two dimensional maps provide a convenient view for assessing the fiber formation and fiber orientation in the entire scanning area.

4.3 RESULTS AND DISCUSSION

We conducted several offline tests to verify the performance of the laser scanning system and studied the effects of the laser incident angle and sample orientation. We also conducted real-time scanning experiments on freshly extruded samples and studied the fiber formation changes during the cooling phase.

A scan step of s = 7 mm was used in our tests. A smaller scan step may provide a better scanning spatial resolution. On the other hand, this value should not be much smaller than the size of the extracted ellipse. Our previous study (Ranasinghesagara and others, 2006) suggested that a smaller than 5 mm scanning spatial resolution may lead to an unstable B parameter, whereas a value larger than 8 mm led to noisy data due to the low power LED source used. When the measurement location was too close to the

incident location, the results were more subject to the effects of surface irregularities. In this study, we improved the signal to noise ratio by using a 10 mW He-Ne laser and found that a 7 mm scanning resolution can provide stable and reliable results in the samples we tested.

4.3.1 Effects of incident angle and fiber orientation

During the angular scanning, the laser beam may have slightly different incident angles at different scanning positions on the sample surface. Especially at the boundary, the sample surface formed a noticeable angle with the optical axis of the camera. This slight angle difference might induce a distortion to the acquired image because our imaging axis is aligned with the normal incident light. However, in the actual instrumentation, this angle is usually about several degrees and thus its effect is negligible. In order to reveal any potential effects, we imaged a fixed point at a sample extruded with 60% of moisture and mix #2 at different incident angles. At each incident angle, the same point was scanned 25 times. The mean and standard deviation of the bias parameter B are shown in Fig. 4-4. The results show no significant effect.

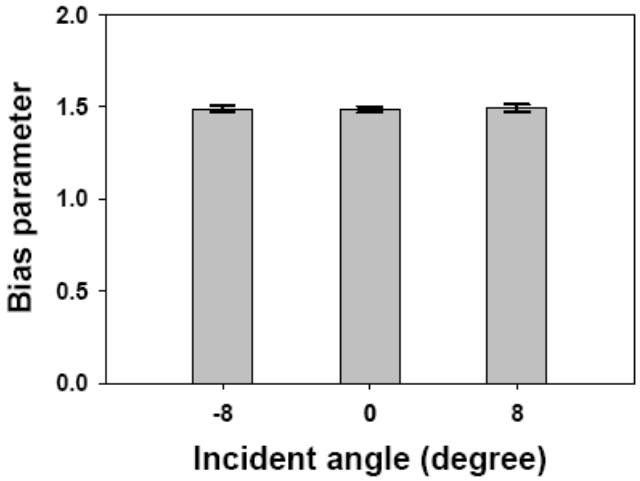

Fig. 4-4. The Bias parameters obtained at three different light incident angles.

The fibers inside extrudates may not be aligned with the extrusion direction. If the imaging system is not perfectly aligned, the acquired images may be spatially distorted and the extract ellipse may depend on the fiber orientation. We confirmed our system alignment by testing the same sample at different orientations. A testing sample was initially placed at a random orientation. Then it was rotated in a step of 30° clockwise. At each orientation, the same location was scanned 25 times. Fig. 4-5 indicates that the bias parameter B does not change with the sample orientation. The extracted equi-intensity data and the best fit ellipse for each orientation are also shown in Fig. 4-5. It can be noticed that the extracted pixel points are noisy due to the speckle phenomenon caused by the coherent light source. However, when scanning moving samples in real time tests, the sample moved a small distance of 0.5 mm during the image acquisition process. The speckle noise was largely reduced because of the averaging effect (Iwai and others 1982), which resulted in smooth equi-intensity profiles.

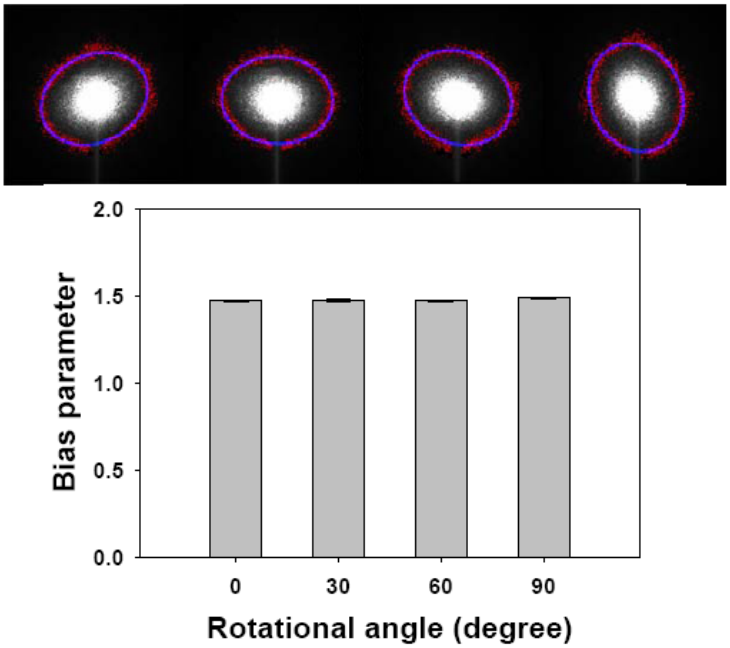

Fig. 4-5. The effect of sample fiber orientation on the measured bias parameter. The top pictures showed that extracted equi-intensity pixel data (points) and the best fit ellipse (line) for the sample at different orientation.

4.3.2 The repeatability of the measurements

To test the repeatability of the measurements (Perez and others 2006), we scanned the same sample area multiple times. All samples were kept in room temperature for several hours to stabilize before taking measurements. Mix #1 was used in the extrusion. The first sample (Fig. 4-6a) was extruded with 70% moisture content and the second sample (Fig. 4-6b) was extruded with 60% moisture content. Following the procedures described in Sec. 4.2.4, the two dimensional maps of the bias parameter and the fiber orientation were constructed. The color scale used to encode the bias parameter B was also shown in the figure along with the maps. For example, the blue color refers to low fiber formation and the red color refers to good fiber formation. The fiber orientation at each scanning location was displayed with small arrows.

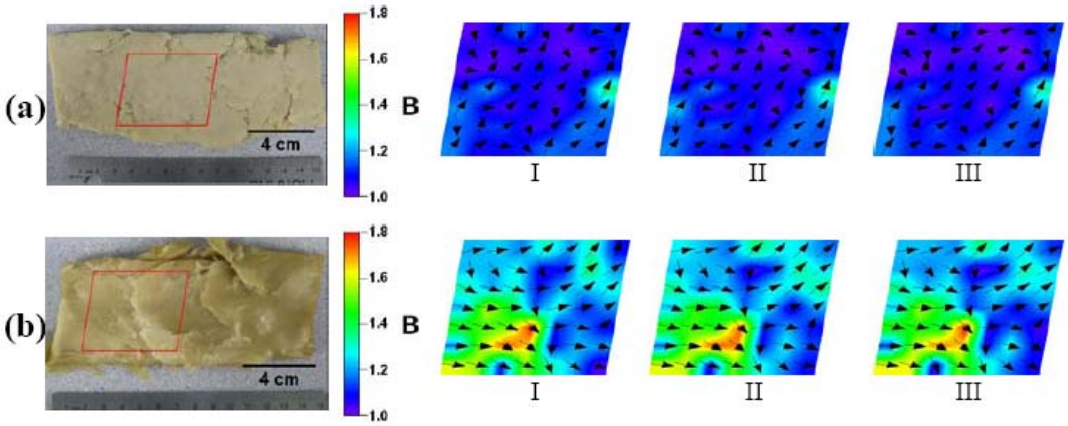

Fig. 4-6. The 2-dimensional maps of the B parameter and fiber orientation angle obtained in two extrusion samples. I, II, and III are three different measurements of the same sample. (a) Sample extruded with 70% moisture content. (b) Sample extruded with 60% moisture content. Mix #1 was used in the extrusion

Previous studies have revealed that the fiber formation and orientation may change due to many extrusion parameters. The major parameters affecting fiber formation are temperature, moisture, and the specific mixture of the raw materials (Lin and others, 2002). The samples extruded with high moisture tend to have a low fiber formation with

random fiber orientations. These effects were also observed in this study as shown in Fig. 4-6, i.e., the bias parameter was larger in the sample extruded with 60% moisture content (Fig. 4-6b) than in the sample extruded with 70% moisture (Fig. 4-6a). In addition, the fiber formation and orientations were not uniform in the extrudates. The fiber orientations in the sample with low fiber formation (Fig. 4-6a) were noticeably more random than those in the sample with good fiber formations. Furthermore, it can be seen that the fiber orientations in Fig. 4-6b were not straight. The fibers in the top portion of the sample in Fig. 4-6b showed a clear curvature.

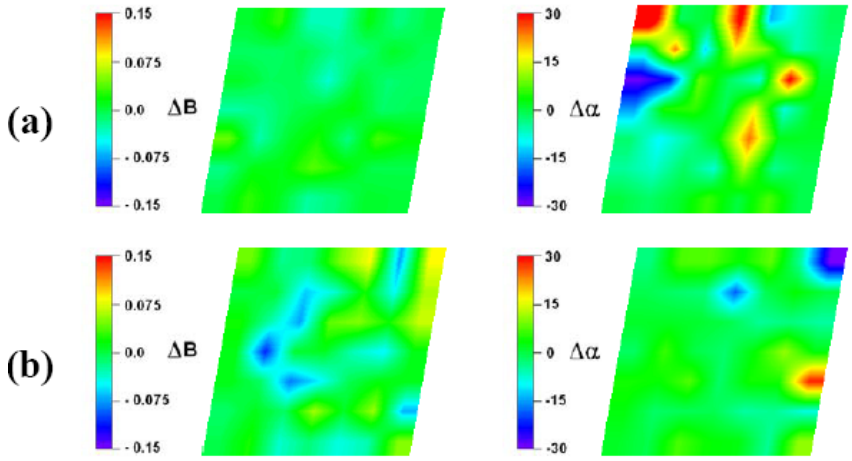

Fig. 4-7. The maps of difference in bias parameter (ΔB) and fiber orientation (Δα) calculated between the first two measurements shown in Fig. 4-6. (a) Sample extruded with 70% moisture content. (b) Sample extruded with 60% moisture content.

Figure 4-6 shows three repeated scans of the same sample. For both samples, the images obtained in three separate scans look very similar to each other. In order to quantify the difference between multiple measurements, we calculated the difference of the bias parameter B and the orientation obtained at all scanning locations in the two scans. To display the results obtained in the entire scanning area, the calculated images of ΔB and $\Delta\alpha$ are shown as two dimensional images in Fig. 4-7. In other words, the value of a point in the difference image (Fig. 4-7) indicates the difference between the values in

the two original images (Fig. 4-6) at the same point. A pseudo-color coding was used to display the numerical values of ΔB and $\Delta\alpha$. In the color scale used (Fig. 4-7), green color indicates small or no difference between scans, red color represents a large positive difference, and blue color represents a large negative difference.

The maximum changes of the bias parameter (ΔB) were 0.109 and 0.045 in samples extruded with 60% and 70% moisture content, respectively. The corresponding average values of the coefficient of variance (CV) were 1.55% and 2.98%, respectively. The change in orientation was larger than in the bias parameter. The majority of orientation angle changes were within ±15° (green color) in both samples. The average values of the coefficient of variance (CV) were 9.76% and 5.71% in samples extruded with 60% and 70% moisture content, respectively. However, a careful analysis indicated that the locations with higher $\Delta\alpha$ values had very low fiber formation. The extracted ellipse was close to a circle when fiber formation was poor, which resulted in an unstable orientation angle. The aforementioned testing results indicated that the laser scanning system showed a good repeatability.

4.3.3 Simulated conveying belt scanning

A simulated conveying belt was constructed using a step-motor driven translational stage to measure the same sample multiple times. The speed of the stage was adjusted to match that of the extruder (10 mm/s). The stepper motor was programmed to bring the stage back to its original position after each scan. The movement accuracy of the translation stage was verified by scanning a calibration grid. The sample was kept on the stage throughout the process so that the same points were scanned in each scan. The laser scanning system (Fig. 4-1) was mounted above the translational stage. The raw material

mix #2 was extruded at 65% moisture content. The extrudates were taken immediately from the extruder and placed on the stage which was moving at the same speed of the extruder. The entire sample was then scanned every 5 min in the first 15 min.

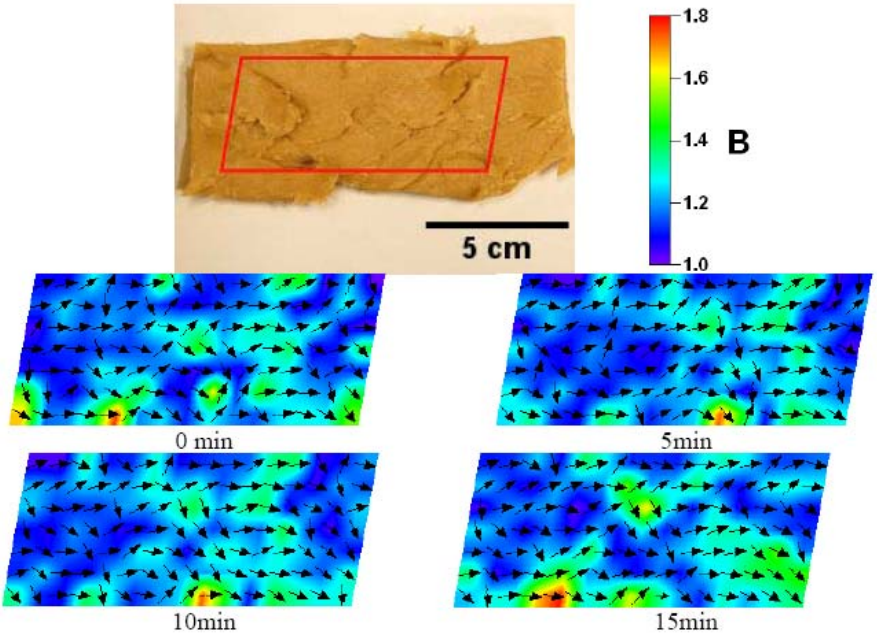

Fig. 4-8. The B parameter and orientation maps of a fresh extrusion sample taken at 0, 5, 10, and 15 min after coming out of the extruder, respectively. The sample was extruded using mix #2 at 65% moisture content.

Fig. 4-8 shows the actual sample and the scanning results at 0, 5, 10 and 15 min after the extrusion. Similar to the results in Fig. 4-6, the blue color shows low fiber formation and the red color shows good fiber formation.

Due to the decrease in sample temperature and the structural settling, the measured fiber structures showed many changes at several locations during the 15 min. To better display the variations, we calculated the changes of the bias parameter and the orientation for the samples measured at 5, 10 and 15 minutes relative to the zero minute result (Fig. 4-9). Despite a few locations, the majority of the sample areas had minor changes in the B parameter (green color).

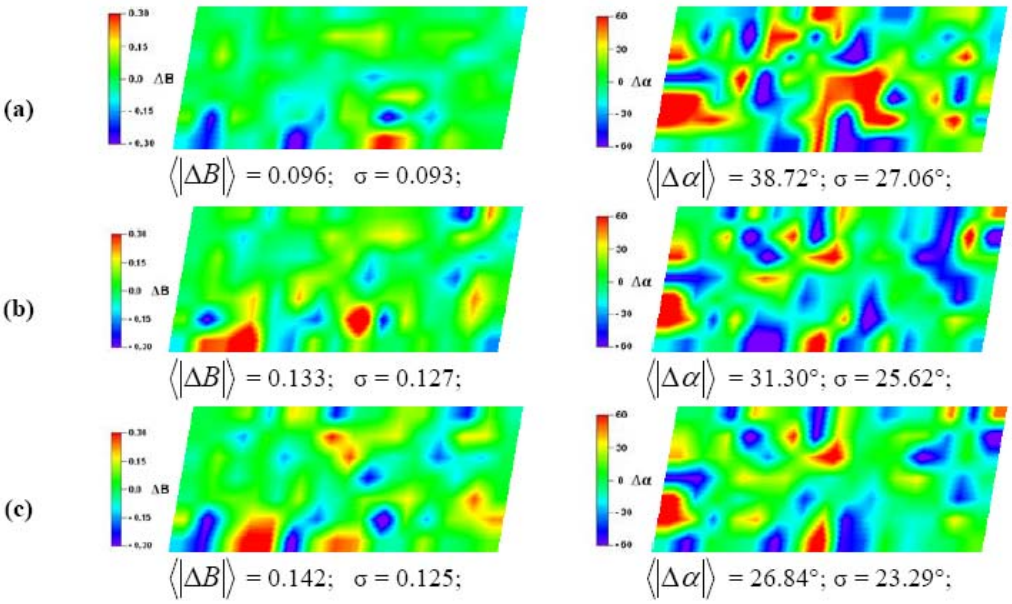

Fig. 4-9. The ΔB and Δα map at (a) 5 min, (b) 10 min, and (c) 15 min measured relatively to the 0 min results in Fig. 4-8. The corresponding mean value and standard deviation of the difference obtained from all image pixels were shown below each image.

As an overall measure of the B parameter change, we calculated the mean value of ΔB for all pixels. Because the ΔB can be negative or positive, we used the absolute value $|\Delta B|$ in the calculation. As shown in Fig. 4-9, the calculated $\langle|\Delta B|\rangle$ had the largest change in the first 5 min, and the changes were slowing down in the 10 min and 15 min results. On the other hand, we observed high variations in fiber orientation angles. The highest variance of Δα was observed in the first 5 min. The change of fiber orientation was much smaller thereafter as shown in Fig. 4-9. These changes may be related to internal changes of the sample during the cooling period.

4.4 CONCLUSION

We developed a real time laser scanning system based on photon migration to map fiber formations in meat analogs. The bias parameter and fiber orientation angle were

obtained at each scanning location at the sample surface and 2-dimensional images were formed to visually display the results. The present scanning speed of our system is limited by the CCD frame rate of 60 Hz and it can be further improved by using a high speed, high sensitive camera. We have applied the system to map fiber structure changes in extrusion samples. We observed large fiber orientation changes during the cooling phase after extrusion. These tests suggested that the system has the potential to be used in time sensitive measurements. This non-destructive real time scanning system may provide a useful means to monitor fiber formations in an industrial setting.

CHAPTER 5

EFFECTS OF INHOMOGENEOUS MYOFIBRIL MORPHOLOGY ON OPTICAL DIFFRACTION IN SINGLE MUSCLE FIBERS

5.1 INTRODUCTION

Classical diffraction theories have been applied to study the diffraction of light by muscle fibers (Fujime and Yoshino, 1978; Fujime, 1975; Yeh and others, 1980; Kawai and Kuntz, 1973). Despite multiple previous attempts to develop an accurate model to describe sarcomere diffraction, few studies have attempted to explain the many inconsistencies observed in the experimental results. For example, the efficiency of first order diffraction was shown to increase with sarcomere length by Baskin and others (1979). Others have reported a curvilinear relationship (Paolini and others, 1976). We hypothesized that such apparent inconsistencies can be explained if the inhomogeneous nature of the muscle fibers was taken into consideration. Most of the previous theoretical studies assumed that muscle fiber had a uniform and well-organized myofibril arrangement featuring straight, skewed or sinusoidal ripple striations (Fujime, 1975; Thornhill and others, 1991; Leung, 1982; Judy and others 1982; Ishiwata and others 1985). On the other hand, microscopic studies have shown that morphological and optical parameters did not remain constant throughout a myofibril (Moss, 1979; Sundell and others 1986; Brenner, 1985; Leiber and others 1984). In general, a muscle fiber can be divided into small domains with relatively uniform myofibril properties. When

illuminated by a wider light beam, the resulting diffraction is the sum of the various levels of diffraction from all the contributing domains (Brenner, 1985; Sundell and others, 1986). Different domains may have different morphological parameters. Sidick and others (1994) found that a random skew effect should be included in order to explain their birefringence experimental results. However, such inhomogeneous morphology effects have not been studied in detail using a theoretical framework.

In this study, we developed an improved sarcomere diffraction model by considering various myofibril inhomogeneities and the domain effect. The new model is consistent with other published data. We applied three-dimensional coupled wave analysis for conical diffraction (3DCW) (Moharam and Gaylord, 1983) to simulate the diffraction of light by muscle fibers. In contrast to the coupled wave analysis for planar diffraction (2DCW) (Moharam and Gaylord, 1982), the 3DCW is appropriate for any incident angle on any incident plane with either TE or TM polarization. Accordingly, 3DCW is more flexible and is a promising tool for analyses of light propagation in whole muscle (Ranasinghesagara and Yao 2007). The simulation results were quantitatively compared with previously reported experimental results on single muscle fibers. We found that a variety of experimental observations can be explained more accurately by the new model that considers inhomogeneous sarcomere morphologies.

5.2 METHODS

5.2.1 3D coupled wave analysis for conical diffraction (3DCW)

Three-dimensional rigorous coupled wave analysis for conical diffraction was formulated by Moharam and Gaylord (1983) to analyze planar and surface relief gratings

mounted at an angle. Since then, it has been widely used to analyze diffractive structures (Gaylord and Moharam, 1995; Van der Aa and Mattheij, 2007). Following Moharam and Gaylord's derivation (1983), the incident region is labeled I and the transmitted region is defined as III. As shown in Fig. 5-1, $\mathbf{k_I}$ is the vector of the wave that is obliquely incident upon the grating at an incidence angle of $\boldsymbol{\alpha}$ and an azimuth angle of $\boldsymbol{\delta}$.

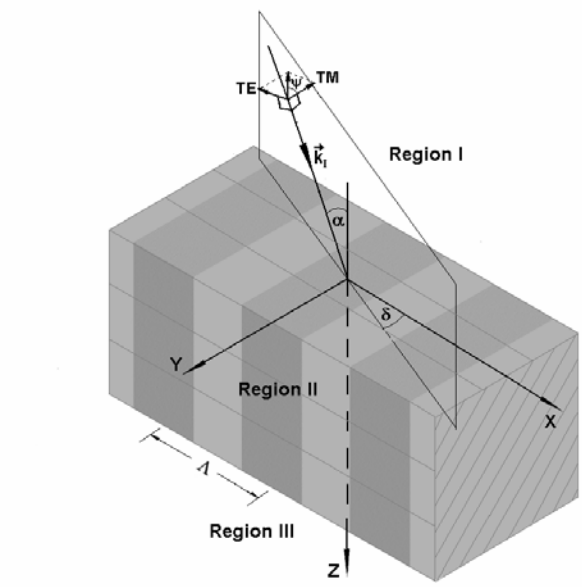

Fig. 5-1. The coordinates used in the 3DCW simulation of a sarcomeric grating structure.

The electrical fields in regions I and III can be expressed as:

$$\mathbf{E_I} = \mathbf{E_0}\exp\left(-j\mathbf{k}_\mathrm{I}\bullet \mathrm{r}\right)+\sum_i \mathbf{R}_\mathrm{i}\exp\left[-j\mathbf{k}_{\mathrm{I}\,\mathrm{i}}\bullet \mathrm{r}\right] \tag{5-1}$$

$$\mathbf{E_{III}} = \sum_i \mathbf{T}_\mathbf{i}\exp\left[-j\mathbf{k}_{\mathbf{III}\,\mathbf{i}}\bullet\left(\mathbf{r}-\mathbf{d}\right)\right] \tag{5-2}$$

where $\mathbf{E}_0$ is the incident electrical field; $\mathbf{d}$ is the fiber thickness; $\mathbf{R}_\mathbf{i}$ and $\mathbf{T}_\mathbf{i}$ are the electrical fields of the i^{th} reflected and transmitted waves, respectively; and $\mathbf{k}_{\mathbf{I}\,\mathbf{i}}$ and $\mathbf{k}_{\mathbf{III}\,\mathbf{i}}$ are the wave vectors in regions I and III, respectively. In region II, the transverse electrical field $\mathbf{E_{II}}$ and the magnetic field $\mathbf{H_{II}}$ can be expressed in terms of the space

harmonics **S** and **U**:

$$\mathbf{E_{II}} = \sum_i \left[S_{xi}(z)\hat{x} + S_{yi}(z)\hat{y} + S_{zi}(z)\hat{z}\right]\exp\left[-j\boldsymbol{\sigma}_\mathbf{i} \bullet \mathbf{r}\right] \tag{5-3}$$

$$\mathbf{H_{II}} = \sqrt{\varepsilon_0 / \mu_0} \sum_i \left[U_{xi}(z)\hat{x} + U_{yi}(z)\hat{y} + U_{zi}(z)\hat{z}\right]\exp\left[-j\boldsymbol{\sigma}_\mathbf{i} \bullet \mathbf{r}\right] \tag{5-4}$$

where ε_0 and μ_0 are the free space permittivity and permeability, respectively; and $\boldsymbol{\sigma}_\mathbf{i} = k_{xi}\hat{x} + k_y\hat{y}$ when the grating is perpendicular to the z-axis (Moharam and others 1995b). The set of coupled wave equations of **S** and **U** can be derived by substituting Eq. 5-3 and 5-4 into Maxwell's equations:

$$\nabla \times \mathbf{E_{II}} = -j\omega\mu_0 \mathbf{H_{II}} \tag{5-5}$$

$$\nabla \times \mathbf{H_{II}} = j\omega\varepsilon_0 \varepsilon(x) \mathbf{E_{II}} \tag{5-6}$$

where $\varepsilon(x)$ is the permittivity distribution in the grating, which is the square of the refractive index profile: $\varepsilon(x) = n^2(x)$. The distribution of permittivity in the grating $\varepsilon(x)$ is independent of $\hat{z}$ because the grating is perpendicular to the z-axis. The Fourier expansion of $\varepsilon(x)$ can be written as

$$\varepsilon(x) = \sum_h \hat{\varepsilon}_h \exp(jh\mathbf{K}x) \tag{5-7}$$

where **K** is the grating vector ($\mathbf{K} = 2\pi/\Lambda$) and Λ is the grating period. The h[th] Fourier coefficient is given by

$$\hat{\varepsilon}_h = \frac{1}{\Lambda}\int_0^\Lambda \varepsilon(x)\exp(-jh\mathbf{K}x)dx \tag{5-8}$$

The derived coupled wave equation can be solved by applying the Floquet condition and continuous boundary conditions. Stable and efficient numerical algorithms

for 3DCW have been previously developed by different groups (Moharam and others, 1995b; 1995a; Lalanne, 1997). The final diffraction efficiencies of each diffraction order for transmitted light (in region III) can be calculated as:

$$DE_{III\,i} = \mathrm{Re}(k_{z\,III\,i}/k_z)\left|\mathbf{T_i}\right|^2 \tag{5-9}$$

where DE_{IIIi} is the i^{th} order diffraction efficiency in region III. k_z is the z component of $\mathbf{k_I}$: $k_z = k_I \cos\alpha$; and $k_{z\,III\,i}$ is the z component of the i^{th} diffracted wave vector in region III. 3DCW can be used for either TE or TM polarized light; calculations from both polarizations can subsequently be averaged to predict results with unpolarized incident light.

5.2.2 Sarcomere model and parameters

A sarcomere has a well-organized structure with a periodic distribution of refractive indices based on the relative concentrations of two major proteins known as actin and myosin (Macintosh and others, 2006). A sarcomere's striated appearance is mainly due to the alternating darker A-bands and lighter I-bands (Fig 5-2a). The segment of A-band with only myosin proteins is called the H zone. The Z-line and M-line are located in the middle of the I-band and in the middle of the H zone, respectively. The sarcomere length is usually defined as the distance between two Z-lines. The "overlap" region refers to the part of the A-band where both actin and myosin are present.

The sarcomere model proposed by Thornhill and others (1991) was used in this study. This model improved the simpler Huxley model (1990) by considering seven sub-regions in a single sarcomere (Fig. 5-2b). These included the overlap region, the H zone, and the Z-line. We did not neglect the Z-line thickness in our study when calculating the

Fourier coefficients of the refractive index distribution. We calculated the exact Fourier components (Eq. 5-8) of these structures. Our calculations indicated that inclusion of the M-line has limited effect (<11% on diffraction efficiencies) on our results.

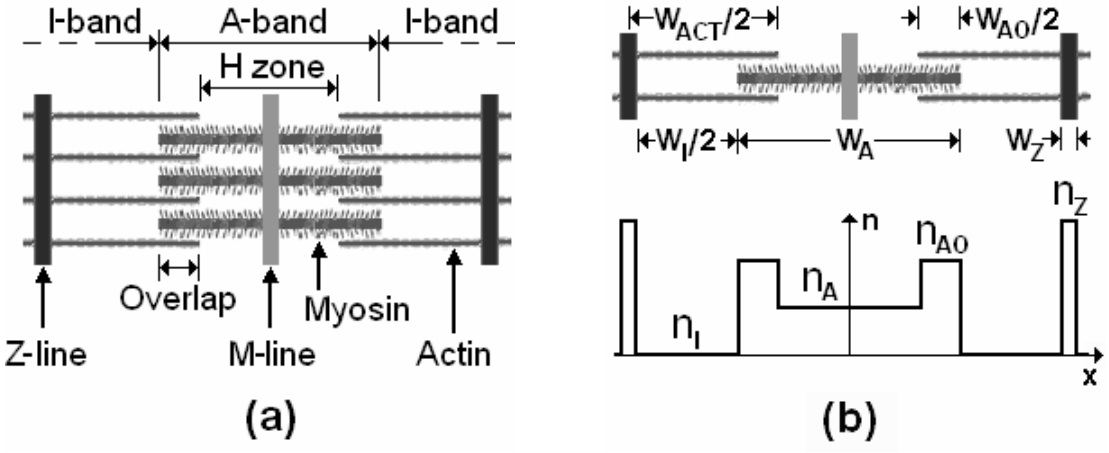

Fig. 5-2. Illustrations of (a) the sarcomere structure and (b) the optical sarcomere model. The distribution of refractive indices is also shown. W_{ACT}, W_A, W_I, W_{AO} and W_Z are the widths of the actin filament, A-band, I-band, overlap region and Z-line, respectively. n_A, n_I n_{AO} and n_Z are the refractive indices of the A-band, I-band, overlap region, and Z-band, respectively.

The majority of the reported experiments involving laser diffraction were conducted in frog *semitendinosus* muscles or rabbit *psoas* muscles. In most cases, the sarcomere length (Λ) varied between 2.0 and 4.0 μm (Kawai and Kuntz, 1973; Yeh and others, 1980; Fujime and Yoshino, 1978; Fujime, 1975; Rudel and Zite-Ferenczy, 1979; 1980; Baskin and others, 1979; Paolini and others, 1976).

In our simulation, all sarcomere parameters were chosen based on experimental measurements. Based on published data, the typical physiological ranges of several major sarcomere parameters are shown in Table 5-1. Unless specified individually, the following default parameters were used in our model. The width of the A-band or thick filament (W_A) was 1.5 μm. The width of the thin filament (W_{ACT}) was 1.9 and 2.0 μm for

frog and rabbit muscle, respectively. The width of the Z-line (W_Z) was 0.05 μm for all muscles. The length of the overlap area of the A-band (W_{AO}) can be calculated as $W_{AO} = W_A + W_{ACT} + W_Z - \Lambda$. The I-band length can be calculated as $W_I = W_{ACT} - W_{AO}$. The myofibril thickness and the fiber diameter (D) were 1.0 μm and 80 μm, respectively, following the approach used in previous simulation studies (Thornhill and others, 1991; Sidick and others, 1992; 1994).

Table 5-1. Muscle sarcomere parameters of the frog *semitendinosus* and rabbit *psoas* muscles reported in published studies.

Parameter	Species	Muscle	Size (μm)	Reference
W_A	Frog	*Semitendinosus*	1.2 ~ 1.6	(Huxley and Niedergerke, 1958)
		Semitendinosus	1.47 ~ 1.59	(Page and Huxley, 1963)
		Semitendinosus	1.43 ~ 1.64	(Carlsen and others 1961)
	Rabbit	*Psoas*	1.63	(Ding and others 2002)
W_{ACT}	Frog	*Semitendinosus*	1.87 ~ 1.97	(Page and Huxley, 1963)
		Semitendinosus	1.70~1.95	(Carlsen and others, 1961)
	Rabbit	*Psoas*	2.24	(Ding and others, 2002)
W_Z	Frog	*Semitendinosus*	0.035 ~ 0.054	(Luther and others 2003)
		Semitendinosus	~0.08	(Knappeis and Carlsen, 1962)
D	Frog	*Semitendinosus*	35-105	(Leiber and others, 1984)
		Semitendinosus	38~103	(Leung and others 1989)
	Rabbit	*Psoas*	60~100	(Burton and Huxley, 1995)

The wavelength (λ) of the incident light was 633 nm. The refractive indices of each sarcomere unit were largely based on the results obtained by Huxley and Hanson (1957) and by Thornhill and others (1991). The refractive index mismatch between the I-band and the overlap A-band was $\Delta n = 0.0074$. The refractive index of the I-band was $n_I = 1.3800$ and the refractive index of the overlap area in the A-band was calculated as $n_{AO} = n_I + \Delta n = 1.3874$. The refractive index of the H zone was $n_H = n_I + \Delta n/2 = 1.3837$ (Thornhill and others, 1991). The refractive index of the Z-line was estimated as $n_Z = 0.11\times(n_{AO}-n_I)\times(W_A/W_Z)$ (Huxley and Hanson, 1957).

It should be noted that the refractive index mismatch, Δn varies with the sarcomere length (Sidick and others, 1994) consistent with the experimental observations (Huxley and Niedergerke, 1958). Similar to a previous study (Yeh and Baskin, 1988), we assumed that Δn was proportional to the square of the sarcomere length. We selected an appropriate proportionality constant by equating a Δn of 0.0074 to a sarcomere length of 3.04 μm. When the fiber is overstretched, the A-band and the I-band can be completely separated and the overlap region disappears. The refractive index of this region was assumed to be the mean refractive index of the sarcomere.

5.2.3 Morphological variations in myofibril organization

In a completely straight skeletal muscle fiber (Fig. 5-3a), sarcomeres are perfectly aligned so that the Z-lines form a straight line that is perpendicular to the muscle surface. However, actual muscle fibers may possess one or more morphological variations such as skew, ripple, or slip as observed in electron micrographs (Sundell and others, 1986).

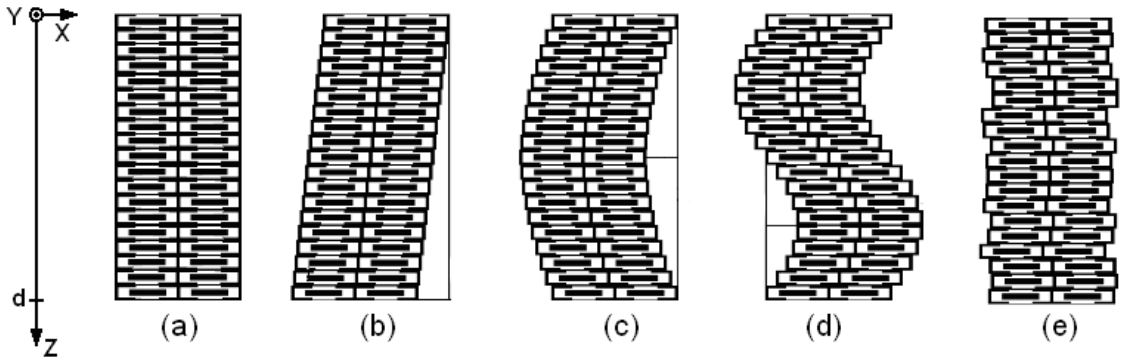

Fig. 5-3. A schematic illustration of muscle fibers of different morphologies. (a) straight; (b)skew; (c)half-wave ripple; (d)full-wave ripple; (e) random slip.

As shown in Fig. 5-3b-e, these structural variations can be modeled in terms of misalignments of the Z-line among myofibrils. In other words, the phase of the Fourier

coefficient in Eq. 8 is shifted by $u(z)$ for a specific myofibril located at z, where $u(z)$ is the distance between the center of a sarcomere and z axis (Thornhill and others, 1991; Sidick and others, 1992).

In skewed muscle fibers (Fig. 5-3b), the displacement function $u(z)$ is a linear function of the depth z:

$$u(z) = z \tan \alpha_{skew} \tag{5-10}$$

where α_{skew} is the slant angle. The $u(z)$ is positive or negative depending on whether the skew is toward the left or toward the right with respect to the z axis. For curved striations (ripple, Fig. 5-3c & 5-3d), the $u(z)$ can be represented as a sinusoidal striation (Thornhill and others, 1991):

$$u(z) = u_{ripple} \sin(2\pi\, z / \lambda_{ripple}) \tag{5-11}$$

where the ripple amplitude u_{ripple} indicates the maximum displacement distance. λ_{ripple} is the periodic distance of the ripple. As in previous studies, two special cases can be considered: the half-wave ripple ($\lambda_{ripple} = 2d$, Fig. 5-3c) and the full wave ripple ($\lambda_{ripple} = d$, Fig. 5-3d), where d is the fiber thickness. The "slip" of a myofibril (Fig. 5-3e) is a phenomenon in which $u(z)$ becomes a random variable (Sidick and others, 1994). For a normal random distribution,

$$u(z) = N(0, \delta_{slip}^2) \tag{5-12}$$

where $N(0, \delta_{slip}^2)$ is a normally distributed random variable with a zero mean and δ_{slip}^2 variance. For convenience, δ_{slip} is represented as a percentage of the sarcomere length Λ in the discussion section.

The misalignment of the Z-line in myofibrils can be modeled theoretically by modifying the Fourier coefficients for each myofibril. The 3DCW was applied to calculate the diffracted electric and magnetic fields in each myofibril. The fields generated by the previous myofibril acted as incident fields for the subsequent myofibril. The process was repeated until light was diffracted from the last myofibril.

5.2.4 Domain effect and variable sarcomere parameters

At different locations along a muscle fiber, the structural profiles of the myofibril might be different. It is reasonable to assume that a specific set of morphological parameters can be used for a small area of the muscle fiber (a small domain), while different parameters may be assigned to different areas. The domain effect can be impacted by many sarcomere parameters, including skew, ripple, slip, sarcomere length, etc. However, in practice skew is the variable most often encountered in real samples and it has a significant impact on diffraction efficiency. In almost all the reported experimental studies, at least a small shift from the theoretical Bragg peak location was observed. Bragg incident angle (θ) is defined as $\sin\theta=m\lambda/2\Lambda$, where m is the diffraction order. These observations suggest that skew is indeed a prevalent morphology that exists in muscle fibers. Electron microscopic studies (Sundell and others, 1986) have shown that the skew angles can be as large as 20°. Accordingly, in this study we focused primarily on the skew-induced domain effect. The skew domain effect can be simulated by assigning a random slant angle α_i to each domain along a single myofibril:

$$\alpha_i = N\left(\alpha_\mu, \alpha_v^2\right) \tag{5-13}$$

where $N\left(\alpha_\mu, \alpha_v^2\right)$ is a normally distributed random variable with a mean slant angle

α_μ and a variance of α_v^2. The diffracted electrical and magnetic fields (Eq. 1-6) from each myofibril were calculated by integrating contributions from every individual domain. These total fields were then applied as incident fields to the next myofibril. The process was repeated until the light passing through the entire muscle fiber and the final diffraction efficiency could be calculated using Eq. 9.

5.3 RESULTS AND DISCUSSION

Most previous experimental studies that explored light diffraction in single muscle fibers can be classified into one of two categories. The first category is related to the Bragg diffraction phenomenon (Rudel and Zite-Ferenczy, 1979; Thornhill and others, 1991; Brenner, 1985; Baskin and others, 1981). In such studies, diffraction efficiencies were measured as a function of incident angles (ω scan). In the second category, light diffraction efficiencies were measured at different sarcomere lengths (Paolini and others, 1976; Baskin and others, 1979; Kawai and Kuntz, 1973; Buchthal and Knappeis, 1940) by stretching the muscle fibers.

5.3.1 Diffraction efficiencies as a function of incident angle (ω scan)

When incident light satisfies the Bragg condition, the diffracted light reaches the maximum or minimum diffraction efficiency depending on the thickness of the volumetric grating (Gaylord and Moharam, 1995).

The open circles in Fig. 5-4a show experimental results by Thornhill and others (1991) that were obtained using a focused TE polarized beam (~50 μm) in a rabbit *pasos* muscle fiber. Diffraction peaks can be seen for three-diffraction orders: -1, +1, and +3. No 2nd order diffraction was observed at the specific sarcomere length (3.04 μm) used.

The Bragg condition predicts that the 1st order peak will be at 5.98º and the 3rd order peak will be at 18.2º. The measured angular difference between the +1st order and -1st order Bragg peaks was 10.96º, slightly less than the 11.96º predicted from the Bragg angle condition.

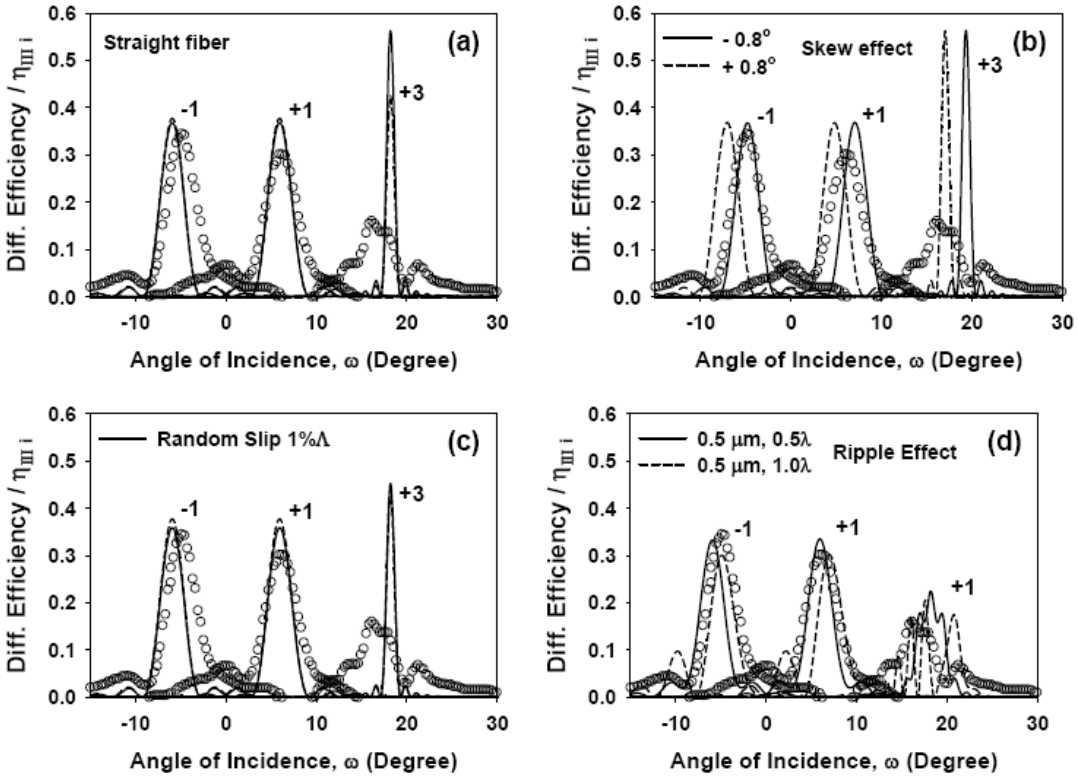

Fig. 5-4. Comparisons between experimental ω-scans (depicted as open circles) and theoretical results (shown as lines) were calculated for different myofibril parameters. Experimental results were obtained in rabbit *pasos* muscle fiber illuminated by TE polarized light. The sarcomere length was Λ = 3.04 μm and the fiber thickness was d = 71 μm. Other parameters were as stated in section 2.2. To conform to the experimental data, the refractive index outside the muscle fiber was 1.0. (a) Results obtained in straight fiber; (b) Effects of a positive (solid) or negative (short dash) skew (α_{skew} =0.8°); (c) Effects of a random slip: δ_{slip} = 1% Λ; (d) Effects of half-wave ripple (λ_{ripple}= 2d) and full-wave ripple (λ_{ripple} = d) with ripple amplitude u_{ripple} =0.5 μm.

The default sarcomere parameters discussed in section 2.2 were applied. It can be seen that the calculated 1st and 2nd order diffraction efficiencies agree closely with the experimental results. However, the 3rd order peak is both narrower and higher than the experimental results. We studied the effects of different sarcomere parameters and

myofibril morphologies in our simulation. We found that variations in W_A had minimal impact on the calculated diffraction efficiencies. For example, changing W_z from 0.05 to 0.10 increased the diffraction efficiency by 6% in all diffraction orders. On the other hand, reducing W_A from 1.5 μm to 1.3 μm increased 1st order diffraction efficiency by only 2%, but the 3rd order diffraction efficiency was reduced by 24%. We found that the refractive indices of individual sarcomere segments had more significant effects. An increase in the refractive index difference between the overlap A− and I−band from $\Delta n=0.0074$ (Thornhill and others, 1991) to 0.0128 (Huxley and Niedergerke, 1958) caused a 124% increase in the 1st order diffraction efficiency and a 77% increase in the 3rd order diffraction efficiency.

The skew effect shifts the ω-scan results from those obtained in straight fibers (Rudel and Zite-Ferenczy, 1979; Thornhill and others, 1991; Brenner, 1985; Baskin and others, 1981). As shown in Fig. 5-4b, a skew angle of 0.8° shifted the Bragg condition by ~1.1°. To study the effect of random slip, we introduced a small slip that was equal to 1% of the sarcomere length $\delta_{slip}=1\%\Lambda$ which was also used by Sidick and others (1994). Figure 5-4c shows that there is essentially no change in the 1st order diffraction, whereas the diffraction efficiency of the 3rd order decreases by 19.6%. Shifting effects were also observed when half-wave and full-wave ripples were applied (Fig. 5-4d). In addition, a rippled muscle fiber also changed diffraction efficiencies of all orders. In particular, the profiles of high diffraction orders were changed drastically. Following Thornhill and others (1991), we incorporated a small ripple of 0.5 μm amplitude. As illustrated in Fig. 5-4d, the small ripple significantly reduced the efficiency of the 3rd order diffraction and broadened its distribution.

The experimental data shown in Fig. 5-4 was obtained using an incident beam with a small illumination spot (Thornhill and others, 1991). Within a small area, muscle fiber parameters are relatively uniform. Therefore multiple domain effects were unlikely to be significant (Brenner, 1985). When a larger incident beam with a 1 mm diameter was used, the obtained ω-scan showed much wider distributions as observed by Rudel and Zite-Ferenczy (1979) and Baskin and others (1981). In Rudel and Zite-Ferenczy's study, a thick (150 μm) frog (*Rana esculenta*) muscle fiber with a sarcomere length of 2.6 μm was used (Fig 5-5). The full-width-half-maximums (FWHMs) of their ω-scan peaks were more than 10º, much larger than the <3º data shown in Fig. 5-4.

Due to domain effects, a different part of the illuminated fiber may have different myofibril profiles. Skew plays a dominant role in broadening the ω-scan profile. The summation of contributions from different domains significantly broadens the angular distribution because the skew effect shifts the ω-scan profile. In Fig. 5-5, we applied a domain effect using a Gaussian distributed skew angle (Eq. 5-12) with a variance of α_v=5.9°. The refractive index outside the muscle fiber was set to 1.377 (experimental mean refractive index of the fiber) in the calculation. To allow a quantitative comparison, the relative display scales among the 1st, 2nd, and 3rd order diffractions were identical for both the simulation and the experiment.

The simulated FWHMs are 13.2°, 8.8° and 9.7° for the 1st, 2nd, and 3rd order diffractions, respectively; while the corresponding experimental results are 12.7°, 12.0° and 8.7°. This result confirmed our hypothesis that the muscle domain effect can significantly broaden the ω-scan profiles.

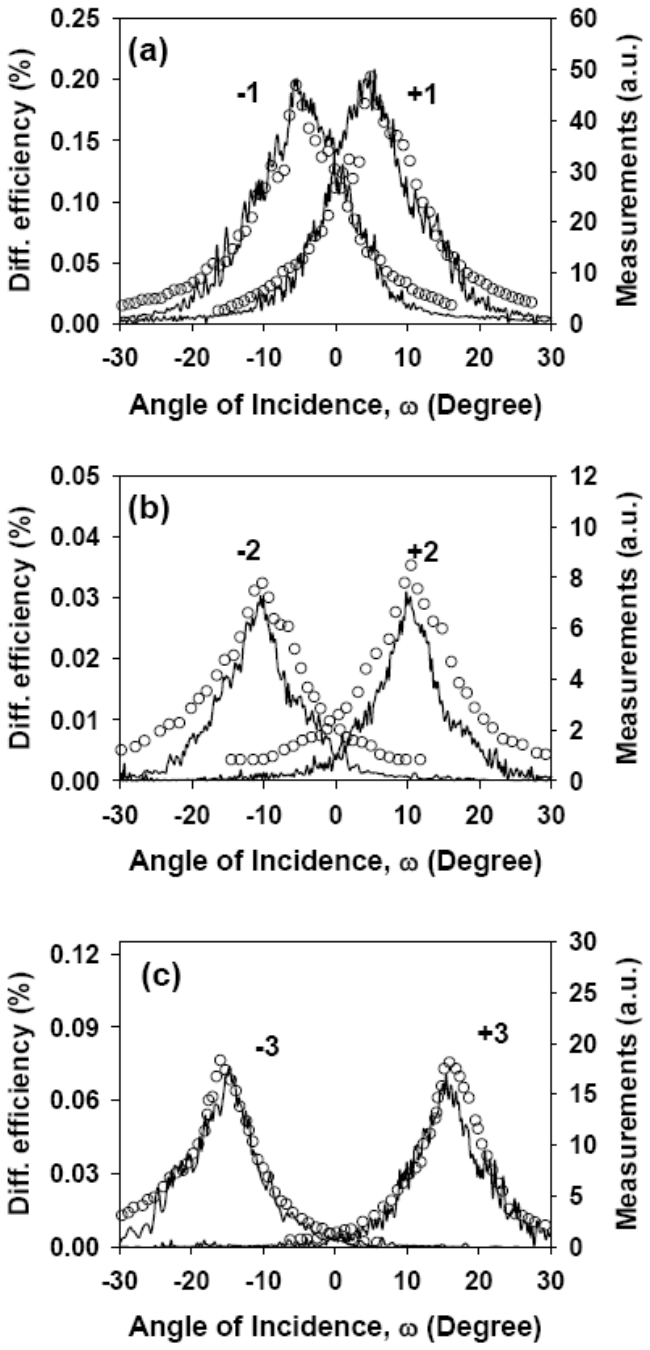

Fig. 5-5. The domain effect on ω-scan profiles (Λ =2.6 μm and d = 150 μm). The circles were defined according to experimental data from Rudel and Zite-Ferenczy (1980). The skew domain effect applied was α_v =5.9º and α_μ =0.0º. The default values discussed in Sec. 2.2 were used for all other sarcomere parameters.

5.3.2 Diffraction efficiencies as a function of sarcomere length

Theoretical diffraction studies (Huxley, 1990; Thornhill and others, 1991; Sidick and others, 1992; 1994) have suggested that oscillations exist at all diffraction orders when expressing diffraction efficiencies as a function of sarcomere length. Those have been attributed to the effects of constructive and destructive interference. On the other hand, such effects have not been observed in experimental studies (Paolini and others, 1976; Baskin and others, 1979). In addition, although it is known that the diffraction efficiency has a great dependence on sarcomere length (Baskin and others, 1979), the experimental results obtained in frog *semitendinosus* muscles showed inconsistent trends. For example, in an early investigation, Buchthal and Knappeis (1940) observed an increase in 1^{st} order diffraction with sarcomere length. Paolini and others (1976) reported that 1^{st} order diffraction had a curvilinear relationship with sarcomere length and a peak diffraction that appeared at 2.8~3.0 μm. Baskin and others (1979) reported that 1^{st} order diffraction increased with sarcomere length and reached a plateau at ~3.8 μm. Kawai and Kuntz (1973) also reported that 1^{st} order diffraction increased with sarcomere length but at a much slower rate than Baskin and others' (1979) results. In their results, the signal increased 10 times when sarcomere length increased from 2.4 μm to 4.0 μm, while Kawai and Kuntz (1973) showed that the signal barely increased by a factor of 2 over the same range of sarcomere lengths.

We found that a variety of experiments under different test conditions yielded results that can be explained by including a proper degree of skew and/or domain effects in the model. A summation of the diffractions from small segments with different skews eliminated the aforementioned oscillations as shown in the results below (Fig. 5-6)

because a skew shifted the Bragg locations (Fig. 5-4). In addition, a different degree of domain effect altered the smoothing effect and therefore produced a different trend as shown in Fig. 5-6.

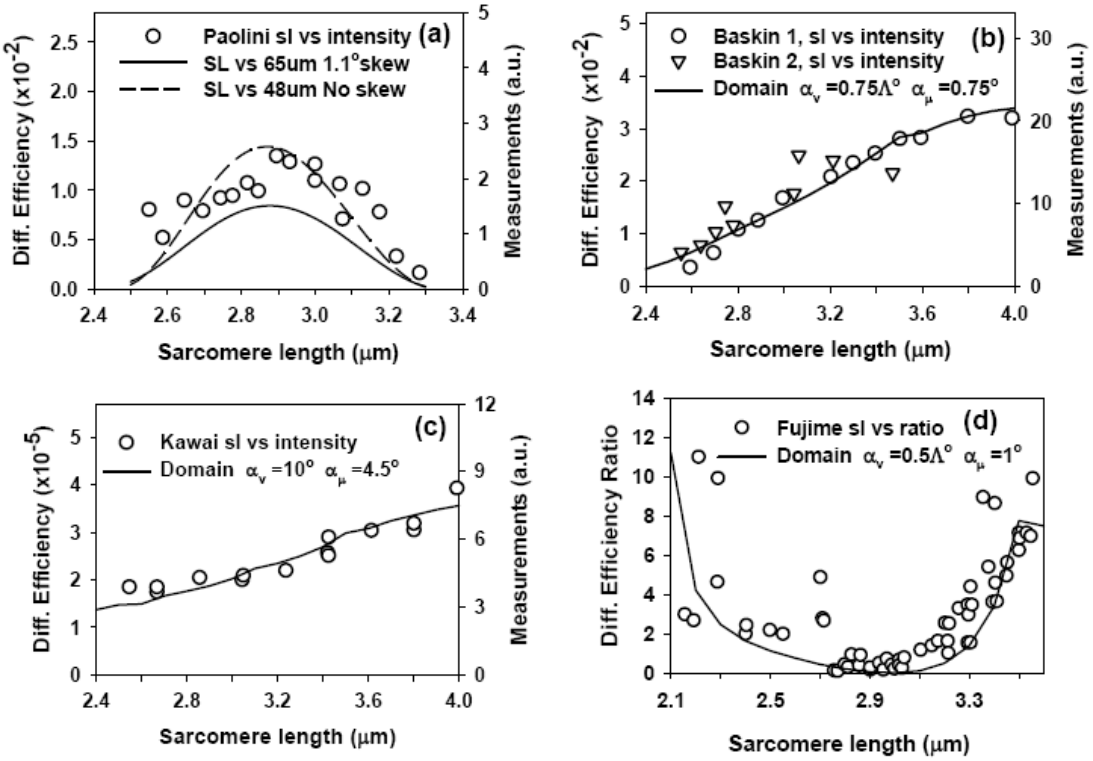

Fig. 5-6. Comparisons between simulated diffraction efficiencies (shown as lines) with experimental results (symbols) at different sarcomere lengths. (a) 1st order diffraction measured by Paolini and others (1976) in single frog *semitendinousus* muscle fiber (circles). Also shown are the calculated results for a straight 48 μm thick fiber (solid line) and with 1.1° skew for a 65 μm thick fiber (dashed line). (b) 1st order diffraction measured by Baskin and others (1979) in single frog *semitendinousus* muscle fiber (circles and triangles). The simulation results were obtained by considering a domain effect (α_v=0.75×Λ° and α_u=0.75°). (c) 1st order diffraction measured by Kawai and Kuntz (1973) in single frog *semitendinousus* muscle fiber (circles). The simulation results were obtained by introducing a domain effect (α_v=10°, α_u=4.5°). (d) The intensity ratio between the 2nd and 3rd diffraction orders measured by Fujime (1975) in frog *fascia of sartorius* muscle fiber (gray circles). Theoretical values were calculated with a domain effect of skew using α_v=(0.5Λ)° and α_u=1.0°. TE polarization was used in all calculations. A common fiber thickness of 80 μm was used for (b), (c) and (d). A value of 1.45 μm was used as the A-band width for (d). The default values discussed in Sec. 2.2 were used for all other sarcomere parameters.

Figure 5-6a shows that the curvilinear profile reported by Paolini and others (1976) can be obtained both in thin straight fibers and in skewed thicker fibers. Baskin and

other's (1979) results (Fig. 5-6b) had a significantly different profile. As shown in Fig. 5-6b, the simulation outputs matched Baskin and others' experimental results very closely when a smaller domain effect of skews was introduced. In the simulation, we assumed that the variance of the skew domain effect (Eq. 13) increased linearly with sarcomere length: α_v = (0.75×Λ)º with α_μ = 0.75º. Since fiber samples were stretched during experiments to achieve longer sarcomere lengths, it was likely that the inhomogeneity increased with sarcomere length.

In Kawai and Kuntz's (1973) experiment, a larger incident beam size (2.0 mm) was used, which potentially resulted in a more significant domain effect. Therefore, we introduced a broader distribution of the skew domain effect (α_v = 10º, α_μ = 4.5º) in the simulation. As shown in Fig. 5-6c, despite small discrepancies at shorter sarcomere lengths, the simulated trend was in good agreement with the experimental results.

Instead of providing absolute diffraction intensity, Fujime and Yoshino (1978) calculated the intensity ratio between the 2nd- and 3rd-order diffractions at various sarcomere lengths. In straight fibers, this ratio has very large fluctuations due to the oscillations in each individual diffraction order. Thus, the result cannot describe the observed experimental data shown in Fig. 5-6d. However, by considering a smaller domain effect (α_v = (0.5×Λ)°, α_μ = 1.0°), the simulated results provided a good match with the experimental results.

5.4 CONCLUSION

We simulated laser diffraction in muscle fibers by applying the 3DCW algorithm to a theoretical sarcomere model. Actual muscle fibers are not perfectly uniform grating

structures. Multiple irregularities may affect laser diffraction efficiency. By incorporating different irregularities in the model, a variety of experimental observations under different conditions can be explained.

The sarcomere parameters used in this study were all within normal physiological ranges as recorded in previous experiments. In some cases, the simulated results do not perfectly match with experimental observations. This might be due to the fact that only the skew domain effect was considered in the simulation, while many other sarcomere parameters could have inhomogeneous distributions in the muscle fiber. In addition, the cylindrical nature of the muscle fibers is not considered in the model and its potential impact needs further study.

Our results indicate that physiological inhomogeneities, as modeled with the domain effect, play a significant role in determining final diffraction efficiencies. With appropriate consideration of such inhomogeneous morphological properties in a physical sarcomere model, the 3DCW theory provides results that are consistent with experimental results of laser diffraction in single muscle fibers.

CHAPTER 6

IMAGING 2D OPTICAL DIFFUSE REFLECTANCE IN SKELETAL MUSCLE

6.1 INTRODUCTION

Light propagation in bulk tissue, i.e. the "photon migration" process, is usually described by the radiative transport theory, or its diffuse approximation (Patterson and others 1989) in many cases. For tissues with anisotropic structures, photon scattering is dependent to the incident direction within the medium. Therefore, the resulting diffuse reflectance at sample surface is not rotational symmetric when point-incident light is used. For turbid medium with a preferred light scattering orientation, both Heino and others' group (Heino and others, 2003) and Gandjbakhche's group (Dagdug and others, 2003) models predicted an elliptical reflectance profile, which was observed experimentally in several anisotropic tissue models (Hebden and others 2004; Sviridov and others, 2005; Ranasinghesagara and others, 2006).

One extraordinary anisotropy tissue that has not been thoroughly studied in the field of tissue optics is muscle. Striated or skeletal muscle is the single most abundant tissue in most vertebrates and is essential for locomotion and other important physiological functions. The normal mechanical and physiological functions of all striated muscles are realized by highly organized structures termed sarcomeres (Lieber, 2002). Sarcomeres are aligned precisely in muscle fibers and are readily observed using light microscopy as alternating light and dark bands called I-band and A-band. The periodic appearance of I- and A-band is due to the difference in their optical refractive indices. Such unique

structure makes laser diffraction a useful tool in studying sarcomere organizations in single fiber (Macintosh and others, 2006; Delbridge and Roos, 1977). However, it is not clear whether the effect of the sarcomere structure is still significant for multiple scattered light in a whole muscle.

Because of the inherent fibrous structure, light propagation in muscle is anisotropic (Binzoni and others, 2006), and optical properties of muscle depend on measurement orientation (Marquez and others, 1998; Zijp and ter Bosch, 1998). More importantly, our recent studies (Xia and others 2006) have found that light scattering in bulk muscle is strongly affected by sarcomere structure. In this dissertation, we investigated the effect of the sarcomere structure on 2D optical reflectance distribution in whole pre-rigor muscles. We discovered a unique reflectance image profile that has not been reported before. In order to quantify the reflectance images, we developed a mathematical model to fit the equi-intensity profiles. The quantitative fitting parameters were used to characterize the changes in reflectance images during stretching and rigor process. None of the existing models can explain our observations. However, we demonstrated that such unique image patterns can be produced when incorporating the sarcomere diffraction in a Monte Carlo model.

6.2 MATERIALS AND METHODS

6.2.1 Sample preparation

All muscle samples were obtained from the Meat Science Laboratory at the University of Missouri-Columbia. *Sternomandibularis* muscle (~5×20×5cm) was chosen in this study because it can be excised from beef cattle within 5-10 min after the

slaughter. It has a uniform muscle fiber orientation, which is a good choice for our studies. All external fat layers around the muscle were carefully removed after sample acquisition.

In addition to muscle samples, isotropic scattering phantoms were made from 20% Intralipid® (Sigma Aldrich, Inc., St Louis, MO) solution to verify the linearity of CCD and fitting algorithms. Protein extrusion products obtained from high moisture extrusion (Ranasinghesagara and others, 2005; 2006) of soy proteins were used to represent fibrous tissues with strong anisotropic structures.

6.2.2 Experimental setup

Muscle samples were placed on the sample holder so that the muscle fiber direction was approximately aligned with the x-axis (Fig. 6-1).

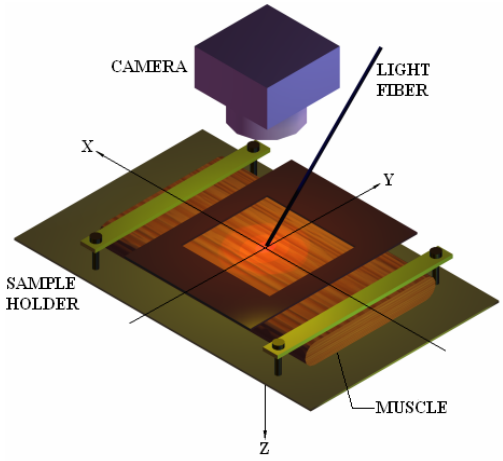

Fig. 6-1. A schematic illustration of the experimental setup. A laboratory coordinate system was set so that the x-axis is along the muscle fiber orientation. Light was incident obliquely via a 400 μm fiber.

Each end of the muscle sample was clamped firmly during the experiment. A black plate with a glass (thickness = 0.13~0.16mm, n=1.52) window (~3.5×4.5 cm^2) was placed

above the sample to create a flat surface. An optic fiber (400 μm) was held slightly above the window at an oblique incident angle of ~43-47º to the sample surface. It was located within the plane formed by the y-axis and the normal vector to the sample surface. The other end of the optic fiber was coupled to a red LED (λ=680nm, 2.2V, 350mA). The incident light intensity on the sample surface was ~120 μW. A digital camera (Model 1010, JAI-Pulnix, San Jose, CA) was mounted above the sample. The camera was aligned so that the light incident point was approximately at the center of the acquired image. Images were transferred to a personal computer via a frame grabber (Meteor-II, Matrox Inc., Quabec, Canada). In order to improve the signal to noise ratio, 10 consecutive images were recorded and averaged after subtracting the dark current. The reflectance image was stored in a 1001×1016 array for further processing.

When studying the effect of rigor process, muscle samples were mounted on the sample holder and reflectance images were taken continuously every 30 minutes for 24 hours. When studying the effect of muscle stretching, only one side of the muscle was firmly attached to the holder, while the other end was pulled to stretch the whole muscle. Once it was stretched to 125% of its original length, samples were released to the original length. Reflectance images were acquired for each stretched and relaxed position. The whole stretching experiment was finished within 4 hours of the slaughter.

6.2.3 Equi-intensity data selection

All acquired images were first smoothed using a 3×3 averaging filter in order to reduce noise. The small area covered by the shadow of the fiber tip was removed from all images. Incident point was considered as the origin. The pixel coordinates of the image were transformed into physical dimensions of the intensity pattern. A pixel corresponding

to a specific distance from the origin along the x-axis (along the muscle fiber) was selected. Then all pixels of the same intensity with a ±1% margin were extracted to represent the equi-intensity profile and their coordinates were stored for further processing.

6.2.4 Evaluation of optical reflectance profile

We designed a non linear fitting model to describe a symmetric geometric shape of equi-intensity contours. A point (x, y) in an equi-intensity contour was represented by:

$$x = aCos\theta\left|Cos\theta\right|^{p} \tag{6-1}$$

$$y = bSin\theta\left|Sin\theta\right|^{p} \tag{6-2}$$

where a and b describe the axial lengths along the x and y-axis, respectively; θ is the angle with x-axis; and $0 \le p \le 1$. Eqs. (1) and (2) can be simplified to obtain following equation.

$$\left(\frac{|x|}{a}\right)^{\frac{2}{p+1}} + \left(\frac{|y|}{b}\right)^{\frac{2}{p+1}} = 1 \tag{6-3}$$

or

$$f(x,y) = \left(\frac{|x|}{a}\right)^{q} + \left(\frac{|y|}{b}\right)^{q} - 1 = 0 \tag{6-4}$$

where $q = \frac{2}{p+1}$ and $1 \le q \le 2$.

Similar to Dagdug and others' (2003) definition of bias parameter for elliptical profile, we defined bias parameter B for our analysis as:

$$B = \left(\frac{b}{a}\right)^{2} \tag{6-5}$$

One advantage of this fitting equation is that it can also be used to fit either circles or

ellipses. When q =1, Eq. (6-4) describes a rhombus; while it becomes an ellipse when q=2 or specifically, a circle at q=2 with a=b.

We used the Levenberg-Marquardt (LM) nonlinear fitting algorithm (Press and others 1988) to estimate the three fitting parameters a, b, and q in Eq. (6-4). The fitting errors can be estimated using the average of the algebraic distance from n data points to the fitted curve:

$$\frac{1}{nab}\sum_{i=1}^{n} f(x_i, y_i)^2 \tag{6-6}$$

When an image profile was not perfectly aligned with the axes in the laboratory coordinates (Fig. 6-1), it was rotated to obtain such alignment before applying the LM fitting method. In addition, a direct least square error ellipse (DLSEE) fitting method (Fitzgibbon and others, 1999) was used initially to calculate the elliptical approximates for each equi-intensity contour. The fitted ellipse center was selected as the origin for the LM method because f(x,y) assumed a coordinate system with the origin located in the center of the contour. We multiplied the obtained major and minor axes values of elliptical fitting by 1.2~1.25 and used them as initial guesses in the LM fitting of parameters a and b. It was found that this initial setting provided better stability during convergence. The y value cannot be negative in the fitting because a non integer q value leads to an exception during calculation. Therefore all negative y values were mirrored to the positive side based on axial symmetry. Parameter q was initially set to unity to restrict any overshooting. The a and b values obtained from the LM fitting were then used to calculate the bias parameter B in Eq. 6-5.

6.3 RESULTS

Figure 6-2 shows the optical reflectance and fitting curves for three different samples: an isotropic Intralipid® phantom, a fibrous extrusion sample, and a *Sternomandibularis* muscle sample. The muscle sample was acquired from a beef cattle right after the slaughter. Clearly, the reflectance profile in skeletal muscle showed a special pattern which was neither a circle as in Intralipid solution nor an elliptical as in fibrous extrudates.

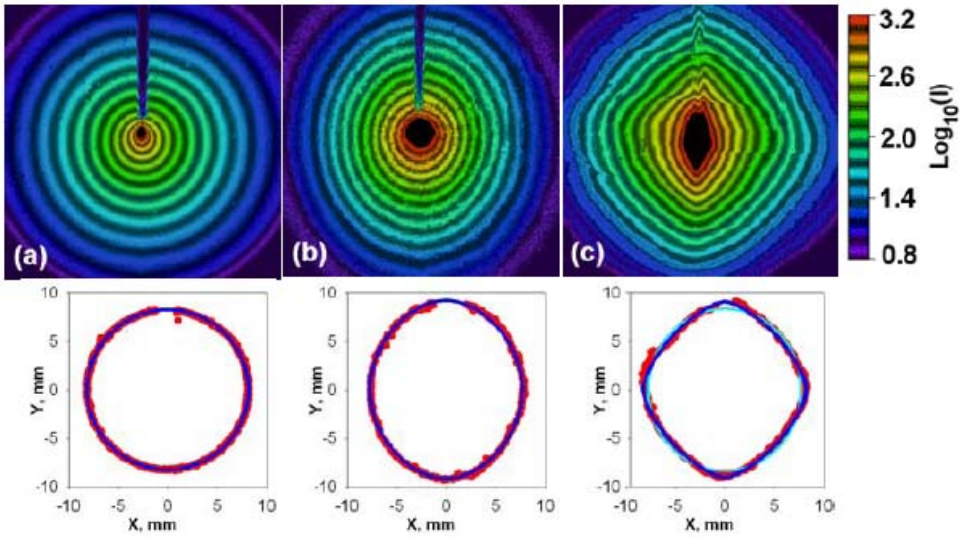

Fig. 6-2. The reflectance images of (a) 20% Intralipid solution (2.28% concentration); (b) soy extrusion sample; (c) prerigor S*ternomandibularis* muscle. Images were displayed in pseudo color which represented the pixel intensity in 10-based Logarithm. All images had sizes of 2.54×2.54cm^2. The graphs in the 2nd row were the fitting results for equi-intensity contours extracted at 8.0 mm from the incident point. Red dots indicated the extracted raw data points on the contour; while blue lines represented the fitting results. The obtained fitting parameters for the three media were: (a) DLSEE: B=1.01, LM: q=1.98, B=1.02; (b) DLSEE: B=1.40, LM: q=1.94, B=1.42; and (c) DLSEE: B=1.17, LM: q=1.46, B=1.21.

Both DLSEE elliptic fitting and Eq. 6-4 were used to find the best fit for these images. As expected, both methods provided an excellent fit for the Intralipid® phantom with bias parameter B close to unity. Fitting using Eq. 6-4 produced a q=1.98, which indicated a circular profile. Both methods provided an elliptic profile for soy extrudates

with B values significantly larger than unity (B=1.40 and B = 1.42). The q value obtained using Eq. 6-4 was 1.94 (Fig. 6-2b). These results indicated that the light reflectance profile from the fibrous sample was indeed elliptic. However, for skeletal muscle, it is clear that Eq. 6-4 (blue line in Fig. 6-2c) provided much better fit than DLSEE method (cyan line). As a confirmation of the visual difference, in Fig. 6-2c, the error from DLSEE fitting method was 14 times higher than that from the LM fitting method.

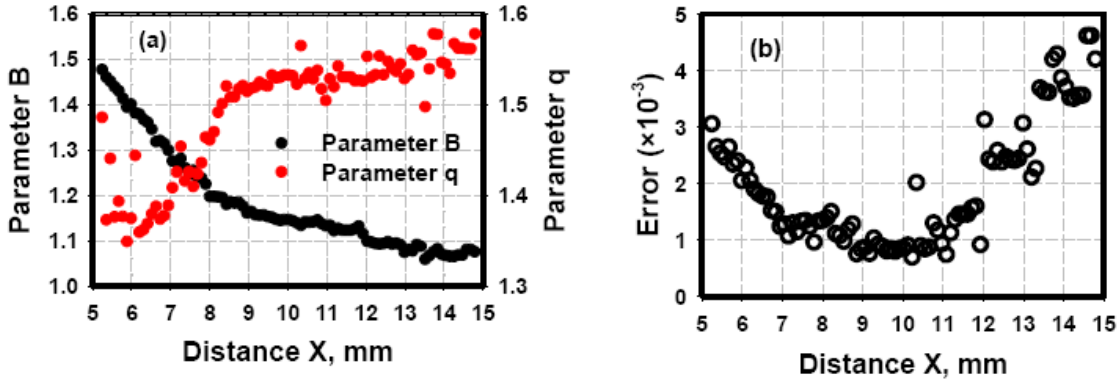

Fig. 6-3. The dependence of fitting results on the distance between evaluation location and light incident location.

In these experiments, we observed that the shape of light reflectance profiles depended on the distance between the evaluation point and the light incident location. Figure 6-3a shows the obtained B and q parameters at a distance from 5 mm to 15 mm for the reflectance image shown in Fig. 6-2c. The corresponding fitting errors (Eq. 6-6) were plotted in Fig. 6-3b. At distances close to the incident point, the fitting results changed rapidly. The calculated bias parameter decreased with the distance. We contributed this phenomenon to the effect of scattering because at a larger distance, photons experienced more scattering events that were not related to tissue anisotropic structures. However, starting from ~8 mm along x-axis, the obtained bias parameter changed very slowly. The fitted q parameter was stable between 8 – 13 mm. The calculated fitting error indicated

that fitting errors were minimized at a distance between 7 – 12 mm. In all subsequent results presented below, we chose 10 mm as the evaluation distance to extract the equi-intensity profiles. However, similar curves were obtained at other evaluation locations.

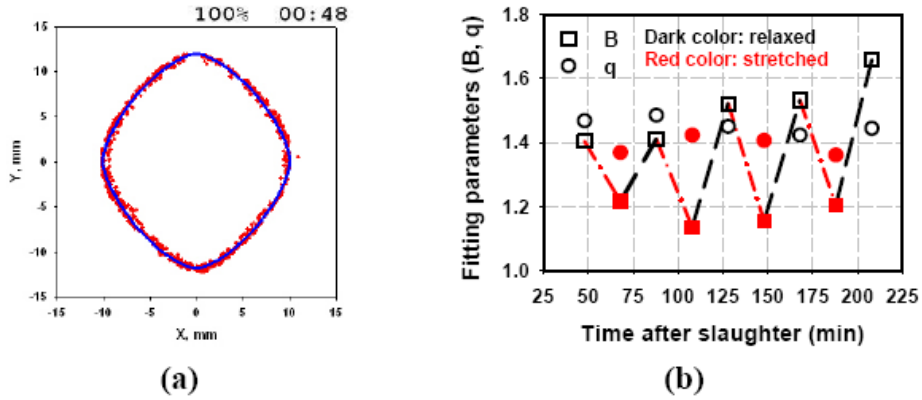

Fig. 6-4. Change of reflectance profile during stretching. (a) image sequence of equi-intensity contour (red) with numeric fitting results (blue). The image was 2.47×2.47 cm^2 in size. (b) Quantitative changes of fitting parameters.

Figure 6-4 shows the effect of stretching on the reflectance profile analyzed using our fitting model (Eq. 6-4). A pre-rigor *sternomandibularis* muscle was stretched to 125% of its original length and then relaxed to its natural length. The measurements were started 48 minutes after the slaughter and repeated four times with 40 minute intervals. The reflectance image acquired for the first relax state was selected as reference. The pixel intensity at 10 mm along the x axis from the origin was used as the reference intensity to extract the contour profiles in all images. Fitting parameters and bias parameters were calculated for each event. Figure 6-4a shows an animated sequence of the changes of the reflectance contour along with the fitted curve during stretch and relax. Figure 6-4b shows the fitted bias parameter B and the q values. It can be seen that the bias parameter was reduced when stretched and recovered when released. Compared to the B value, the q values had very little change.

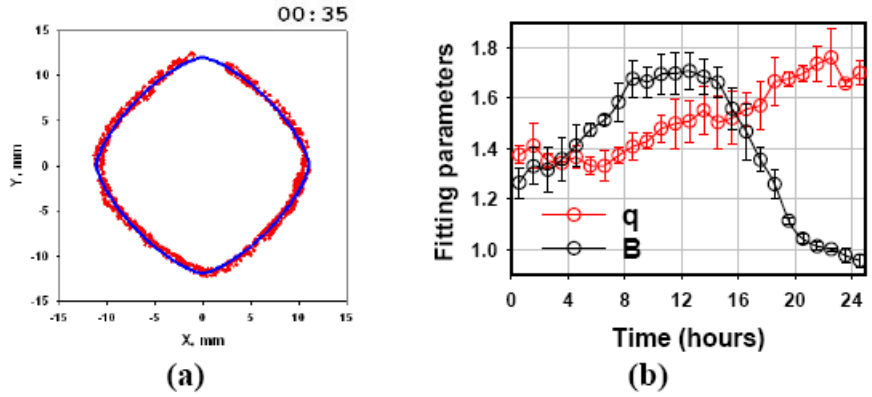

Fig. 6-5. Change of reflectance profile during rigor process. (a) image sequence. The image had a physical size of 3.05×3.05 cm^2. (b) Fitting parameters q and B versus time. For clarity, data points measured ever hour were shown in the figure.

Optical reflectance was also monitored during rigor mortis development at room temperature (Fig. 6-5). Muscle samples were fixed by restraining both ends to a sample holder. Images were recorded every 30 minutes. The first measurement was taken 35 minutes after the slaughter. Each time the average intensity of a pixel located 10 mm from the origin was used to extract the equi-intensity contours. Figure 6-5a shows the animated sequence of the reflectance images during the 25 hr rigor process. Figure 6-5b shows the variations of the bias parameter B and the fitting parameter q. These results indicated that the q parameter had little change during the first 8 hrs while the bias parameter B increased from 1.2 to ~1.7. The q then increased until it reached ~1.8 at ~24 hrs after slaughter. On the other hand, the B parameter stabilized from 8 ~ 14 hrs and then started to decrease thereafter. After 24 hrs, the reflectance profiles approached circular patterns.

6.4 DISCUSSION

Equi-intensity profiles of optical reflectance in *Sternomandibularis* muscle showed a distinct pattern that can not be explained using currently available anisotropic photon

migration models (Heino and others, 2003; Dagdug and others, 2003; Kienle and others, 2003). A previous model (Kienle and others, 2003) based on Mie scattering of infinite cylinder can produce similar rhombus patterns. However, in their simulation the pattern became elliptic when the measurement location was only ~2 mm away from the light incident point. On the contrary, the patterns observed in prerigor muscle were distinctly different from ellipse even at locations that were much more than 1 cm away from the incident point (Fig. 6-2 and 6-3). We found that such distinct pattern can be quantitatively analyzed using a simple fitting equation (Eq. 4) with three parameters a, b, and q. As in previously reported studies (Dagdug and others, 2003), the non-unity bias parameter B suggested anisotropic optical properties parallel and perpendicular to muscle fibers. More importantly, the smaller q parameter clearly indicated the deviation from the elliptic profile predicted from all existing models.

We found that the significant decrease in the bias parameter during stretching was mostly due to the increase in parameter a. This suggested that light propagated longer distances along the muscle fiber. Since stretching, pre-rigor muscle resulted in proportional changes in the sarcomere length as well as the fiber diameter (Gillis and Hendrickson, 1969), both effects had the potential to modulate the photon migration process. On one hand, an increase in sarcomere length can alter the scattering phase function and scatter more light toward fiber orientation (Yeh and others, 1980). On the other hand, the decrease in fiber diameter may reduce the scattering cross section (Marquez and others, 1998), which reduced the probability that light being scattered away from the fiber orientation. More studies are necessary to elucidate the detailed mechanism.

In rigor mortis analysis, equi-intensity contour were extracted at a fixed distance (10 mm) from the incident location in all images. The bias parameter B reflected the relative distance that the photon traveled perpendicular and parallel to muscle fibers. Based on our observation in the stretching experiment (Fig. 6-4), the initial increase in bias parameter during the first 8 hrs seemed to suggest a contracting process of sarcomere. Such sarcomere shortening phenomenon was studied before (Hertzman and others 1993) and found to be subjective to effects of environmental factors especially temperature. As rigor mortis progressed, actin and myosin proteins were bound together and formed actomyosin complex. This stage corresponded with the phase in Fig. 6-4b where the bias parameter became stabilized. It has been recognized that after ~12 hrs, the proteolysis process (Goll and others 2003) eventually became significant because of the release of autolytic enzymes stored in lysosomes. These enzymes broke down the actomyosin complex and disintegrated sarcomere structure. The destruction of sarcomere structures may explain the decreasing of the bias parameter. More interestingly, the change in q values indicated the shape of the equi-intensity profile changed significantly during the rigor process. Initially, q was small and equi-intensity contours formed a pattern closer to a rhombus. After 24 hours, the equi-intensity contour formed a pattern closer to an ellipse as a result of the loss of sarcomere integrity. It is interesting to note that when we kept muscle samples at controlled low temperature (4 ºC) during rigor, the bias parameter varied slowly with the time due to a slower rigor process. Nevertheless, optical reflectance measurements were able to reflect structural changes of the whole muscle during pre and post rigor.

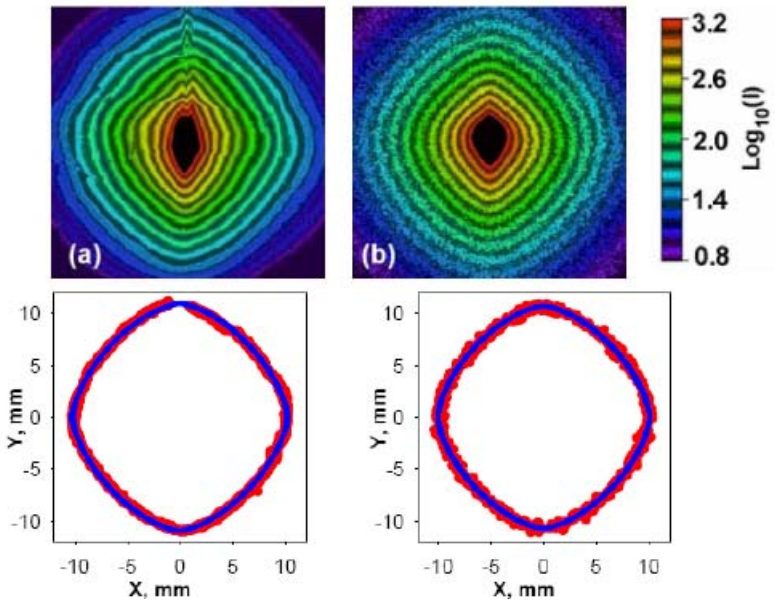

Fig. 6-6. The reflectance images of (a) prerigor S*ternomandibularis* muscle acquired in experiments; and (b) Monte Carlo simulation (10^7 photons). All images were 2.54 × 2.54 cm^2. The graphs in the 2nd row show the corresponding equi-intensity contours (red dots) extracted at 10mm from the incident and the LM fitting results (blue lines). Fitting results were (a) q=1.54, B=1.15; and (b) q=1.55, B=1.13.

Light diffraction by sarcomere in single fibers is a well studied subject in muscle physiology. As an approximation, muscle fibers are often treated as a volumetric phase grating in theoretical studies. Two dimensional couple wave theory (Moharam and Gaylord, 1982) has been successfully applied before in studying muscle sarcomere structures in single muscle fibers or fiber bundles (Sidick and others, 1992). Our current experimental studies suggested the unique reflectance observed in whole muscle is likely due to the sarcomere diffraction. In order to test this, we applied a three dimensional coupled wave theory (Moharam and Gaylord, 1983) in a semi-infinite Monte Carlo model. The sarcomere structure model and properties proposed by Thornhill and others (1991) was used in the calculation. Each sarcomere was taken as a single grating with following geometrical parameters: sarcomere length = 3.1 μm, length of the A band =1.5

μm, and length of the I band = 2.0 μm. A photon packet experienced regular scattering events as in the conventional Monte Carlo model (Wang and others 1995) with Henyey–Greenstein phase function. However, in between two consecutive scatterings, the photon had a probability to be diffracted instead of following a ballistic trajectory. Based on incident angle and the step size, diffraction efficiency and diffraction angle was computed using the coupled wave theory. The effect of step size and incident angle can change the diffraction efficiencies as shown in previous studies (Moharam and Gaylord, 1982; 1983; Thornhill and others, 1991; Sidick and others, 1992). The actual diffraction angle was sampled based on the relative efficiencies of all diffraction orders and was used as the new photon direction. In addition, to consider the fibrous effect, different scattering probabilities (scattering coefficients) were assigned to the interaction direction parallel and perpendicular to the muscle fibers (Nickell and others, 2000; Heino and others, 2003). This process was continued until photon lost its energy due to absorption or photon was transmitted out of the medium.

Figure 6-6b shows a simulation result for optical reflectance with a total 30% diffraction probability. A pencil beam was incidental upon the thin glass window on top of the sample at 45º oblique incident angle. Optical properties used were scattering coefficient along x-axis μ_{sx}=13.4cm^{-1}, scattering coefficient along y-axis μ_{sy}=30cm^{-1}, anisotropy g=0.94, absorption coefficient μ_a=0.1cm^{-1}. The quantitative fitting results are also shown in Fig. 6-6. It can be seen that the simulated reflectance pattern (Fig. 6-6b) was very similar with experimental results (Fig. 6-6b), especially at a larger distance from the incident point. However, discrepancies can be observed at locations that were closer to the light incident location. Figure 6-7 shows the calculated B and q parameters at

different distance for the reflectance images shown in Fig. 6-6. The simulated images were quite noisy at distances greater that 12 mm and we could not get reliable fitting results. It can be seen that the simulated B and q had very good agreements with experimental observations at a distance larger than 8 mm. The differences at smaller distances were obvious. This is likely caused by the aforementioned method we applied to handle the fibrous effects, which may only be valid in the diffuse region. Better results might be produced if the cylindrical geometry (Kienle and others, 2004) of muscle fiber is considered.

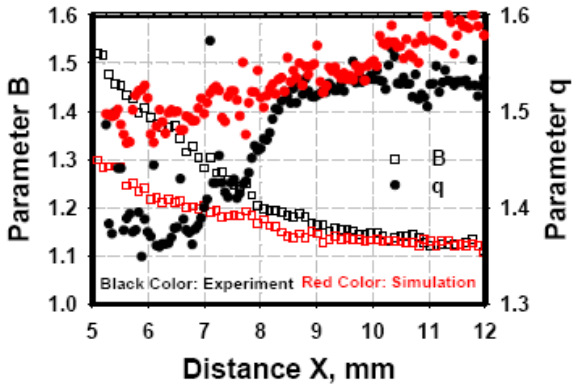

Fig. 6-7. The dependence of fitting results (B and q) on the distance between evaluation location and light incident location: comparison between experiment (black) and simulation (red).

6.5 CONCLUSION

All existing light propagation models failed to describe the light propagation in striated muscles because the effects of the sarcomere structure were not accounted for. We have developed a fitting function which can fit the experimental equi-intensity contours very well. The fitting parameters provided a quantitative description of light reflectance patterns measured at muscle surface. Our *in vitro* studies on pre-rigor muscles highlighted that optical reflectance images that can monitor the changes in the muscle

microstructures. Our Monte Carlo simulation added strong evidence that the sarcomere structure was responsible for the unique reflectance patterns observed in our experiments.

As sarcomere is the fundamental functional unit in muscle (Lieber, 2002), a method that can monitor its dynamics in whole muscle may prove useful in many muscle related studies such as exercise physiology. In addition, sarcomere length is an important factor that determines the eating quality of meat (Koohmaraie and others 2002). Therefore, such a method may provide a useful tool in characterizing muscle qualities in the meat industry.

CHAPTER 7

EFFECTS OF MUSCLE PHYSICAL AND CHEMICAL PROPERTIES ON OPTICAL DIFFUSE REFLECTANCE

7.1 INTRODUCTION

Light propagation methods have been widely applied in various biomedical studies and food industry (Tuchin, 2000; Raghavachari, 2001; Ranasinghesagara and others, 2005; Huanga and others 2008). Only a few investigations have been made on light interaction in whole muscles. Several groups have applied near infrared spectroscopy (NIRS) on live muscles to study muscle metabolism, blood flow and muscle oxygenation (Binzoni and others, 2006; Yu and others, 2005; Beekvelt Van and others 2001; Hampson and Piantadosi, 1998). Others have applied NIRS to classify the postmortem muscle (meat) qualities (Byrne and others 1998; Rødbotten and others 2000; Swatland, 1989; Shackelford and others, 2001; Swatland and Irie, 1992) based on absorption. Light propagation within the muscle depends on the absorption and scattering coefficient of the muscle. The optical absorption is related to the light attenuation inside the muscle by different chemical compositions (Snyder, 1968). On the other hand, optical scattering which is the probability of light being scattered by structural components reflects the structural information of the muscle.

In recent studies, Xia and others (2006; 2007; 2008a; 2008b) have shown the relationship between optical scattering and muscle sarcomere structures. They used a

fiber optic probe to acquire one dimensional optical spectrum for oblique incidence. The absorption and scattering coefficients were calculated by applying theory of oblique-incident reflectometry developed by Wang and Jacques (1995) on spatially resolved data. Their technique was only used to obtain optical reflectance data perpendicular to the muscle fiber. Recently, we showed that unique two dimensional optical reflectance of the whole muscle can provide additional information of underlying muscle structure (Ranasinghesagara and Yao 2007).

The muscle starts to become meat after slaughter. These changes start as a result of the biochemical changes within the muscle and depend on the species, race, structure, muscle type and physical activity of the muscle (te Pas and others 2004). The Gravitational force allows certain muscles to shorten and other muscles to stretch during suspension. By making use of various suspension methods, it is possible to acquire different sarcomere lengths for the same muscle in the carcass (Hostetler and others 1970). In addition, suspension method affects the shear force and taste panel scores. It is also known that muscles inherit different characteristics from their breed. Tenderness is one of the main palatability attribute considered by consumers. Crouse and others (1989) have observed meat from certain breeds are tender than other breeds. (Shackelford and others, 2001). Our recent studies has shown that optical parameters shows a good correlation with meat tenderness, sarcomere length, aging, etc. (Xia and others, 2006; 2007; Ranasinghesagara and Yao 2007). However, a comprehensive study of optical parameters in muscles under different suspensions and from different breeds has not been reported.

In this study, we calculated various optical parameters from two dimensional optical reflectance images in multiple muscles. The effects of breed, aging and muscle type on those optical parameters were analyzed. By understanding the correlation between optical parameters and muscle physical and chemical properties, we will be able to design better optical techniques to predict different characteristics of the muscle and meat in the future.

7.2 MATERIALS AND METHODS

7.2.1 Animals

Fourteen cattle were slaughtered in the meat science lab at South Dakota state university. Half of the cattle were "*Bos indicus*" and other half were "*Bos taurus*" breed. The *Bos indicus* cattle are traditionally tougher because they have limited proteolysis process. Animals were numbered randomly and the numbers 1,5,7,8,10,12 and 13 were *Bos indicus* and the numbers 2,3,4,6,9,11,14 were *Bos taurus*. To facilitate adequate time for sample preparation and measurements, numbers 1 to 7 were slaughtered in one day and the rest were slaughtered on another day. After the slaughter, the carcasses were split mid-sagittally. One side of the carcass was hung by the hip (HS) and other side was hung by the leg (NS). The limbs were allowed to suspend free in +4ºC for one day. After 24 hours, *M. longissimus dorsi* (LD), *M. psoas major* (PM), and *M. semitendinosus* (ST) muscles were removed from the limb. Four steaks of similar size (approximately 3cm width × 3cm length × 2cm thick) from each muscle were separated, vacuum packaged, and stored in +4°C for 1, 4, 7 and 10 day measurements. Three more steaks of the same muscle were stored for sarcomere length, shear force and proteolysis measurements.

7.2.2 Optical imaging

The steak sample was placed on a lab-jack (Fisher Scientific International Inc., Hampton, NH) such that the muscle fiber direction was approximately parallel to x axis (Fig. 7-1). A black plate with a glass window (~3.5×4.5cm) was mounted above the sample at a fixed height. The lab-jack height was adjusted until the sample lightly touched the glass. Small monochromatic light beam (~2mm diameter BW = 20nm) was focused to the center of the glass. The light fiber was placed in the y-z plane with an oblique angle of ~46.5º to the z axis. The incident point was considered as the origin of our Cartesian coordinate system.

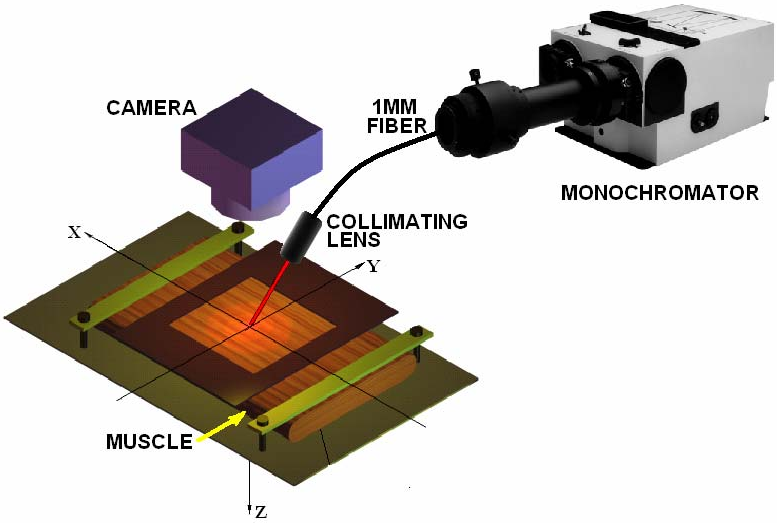

Fig. 7-1. Schematic of the experiment setup. Entrance side of the Monochromator was coupled to a 100W Quartz Tungsten Halogen light source.

Wavelength of the incident beam was varied from 640nm to 860nm in 20nm steps by a software controlled motorized monochromator (MicroHR, Horiba Yvon, Edison, NJ, USA). A digital camera (PULNIX 1010, JAI-Pulnix, San Jose, CA, USA) was mounted above the meat sample so that the light incident was approximately at the middle of the image frame. The incident light intensity at each wavelength was kept constant and the

ambient light was blocked throughout the procedure. The backscattered reflectance images were transferred to a personal computer via a frame grabber (Matrox Meteor-II/Digital Matrox Inc Dorval, Quebec, Canada). Five continuous images were recorded and averaged to improve the signal to noise ratio. After removing the dark image, the reflectance image was stored in a 10bit 1001×1016 array for further processing. For each sample, two different locations were imaged. The second incident location was kept within 5mm from the first location.

7.2.3 Data analysis

To quantitatively study the diffuse reflectance, we obtained the following parameters: the geometric profiles of the equi-intensity reflectance, the spatial gradients of the reflectance parallel and perpendicular to muscle fibers, and the total intensity of diffuse reflectance.

Before the equi-intensity selection, we applied a 3×3 averaging filter to reduce noise and smooth the data. We selected a pixel located at a specific distance from the incident point and its intensity was set as the reference intensity. All the intensities similar to the reference intensity with ±1% margin were extracted and their coordinates were stored. Then the geometric center of the equi-intensity profiles were obtained using a direct least ellipse fit (Fitzgibbon and others, 1999; Ranasinghesagara and Yao 2007). By considering it as the origin, we fitted the equi-intensity data using Eq. 6-4 with the Levenberg-Marquardt algorithm to obtain a, b and q values. The B parameter was calculated as discussed in Eq. 6-5.

The spatial decay rate of the reflectance gradient ($\log_{10}$(intensity)/mm) related to the optical properties of the sample (Wang and Jacques, 1995). In isotropic medium, the

spatial gradient of the optical reflectance is independent of measurement directions. This is not true for skeletal muscles. Therefore, the spatial gradient along the x axis and y-axis were calculated separately. The pixels that lay in between 5mm and 10mm from the center of the profile along the x-axis were extracted. The log intensities against the distances were fitted by a linear fitting algorithm (Press and others, 1988) to obtain the spatial gradient. Similarly, by extracting pixels along the y axis, we calculated the spatial gradient perpendicular to the muscle fibers. The total intensity of the optical reflectance image was calculated by integrating the intensities of all pixels within the area between 5 mm and 10mm in radius. By selecting this region, we avoided highly saturated pixels near the incident point and noisy pixels at the boundary. As the number of pixels in the above region is constant for all the images, total intensity was represented as mean intensity after dividing by the total number of pixels in the above region.

7.2.4 Warner-Bratzler shear force

Warner-Bratzler shear force measurements were obtained on steaks cooked to 71°C on an electric calm shell grill (George Forman Indoor/Outdoor grill Model GGR62, Lake Forest, IL). After cooling the sample for 24 hours at 4°C, six to eight cores (ϕ = 1.27cm) were removed from each sample. Coring was done parallel to the muscle fiber orientation. Using a Warner-Bratzler shear machine (G-R-Electric Manufacturing Company, Manhattan, KS), maximum shear force for each core was recorded. Final WBSF value was obtained by averaging peak shear force values achieved from all cores.

7.2.5 Statistical analysis

Statistical analysis was carried out with SAS software (SAS Inc., Cary, NC). Data was categorized by breed, suspension, days and muscle type. Significance of differences

among optical parameters and different categories was determined by analysis of variance (ANOVA) using the Bonferroni (Dunn) t-test. Differences were considered as significant at $p<0.05$ level.

7.3 RESULTS AND DISCUSSION

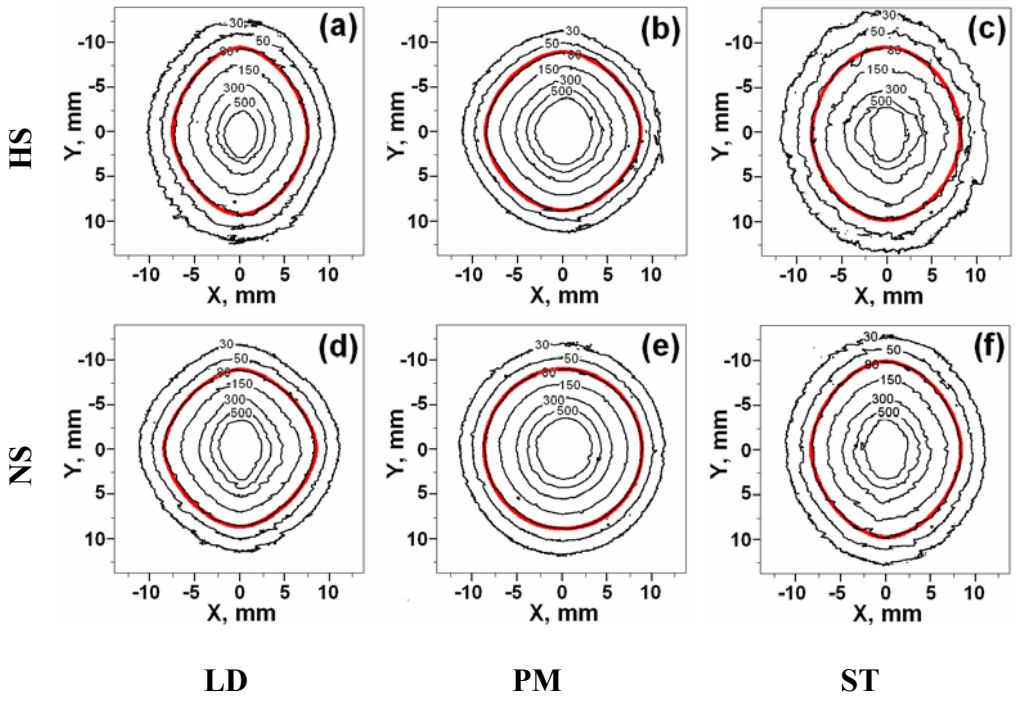

Fig. 7-2. Equi-intensity contours of three muscles with different suspensions for animal #3. Best fit curve when intensity equals to 80 a.u. is shown in Red. Incident wavelength was 720nm (a) HS LD: q=1.70, B=1.55; (b) HS PM: q=1.77, B=1.03; (c) HS ST: q=1.85, B=1.36; (d) NS LD: q=1.66, B=1.03; (e) NS PM: q=1.97, B=1.02; (f) NS ST: q=1.76; B=1.38.

Figure 7-2 shows examples of the best fit curves at a single intensity. The equi-intensity profiles in PM muscle with hip-suspension and LD muscles with normal suspension look similar to the unique two dimensional profiles observed before for *M. Sternomandibularis* (Ranasinghesagara and Yao 2007). Their q parameters are ~1.7, representing a profile between a rhombus and an ellipse. Under normal suspension, contours PM muscle are almost elliptical with a q parameter close to 2.0. The equi-

intensity profiles of LD-HS, ST-HS and ST-NS muscles tend to elongate along y axis than others with B parameters larger than 1.0.

Figure 7-2 shows examples of the best fit curves at a single intensity. The equi-intensity profiles in PM muscle with hip-suspension and LD muscles with normal suspension look similar to the unique two dimensional profiles observed before for *M. Sternomandibularis* (Ranasinghesagara and Yao 2007). Their q parameters are ~1.7, representing a profile between a rhombus and an ellipse.

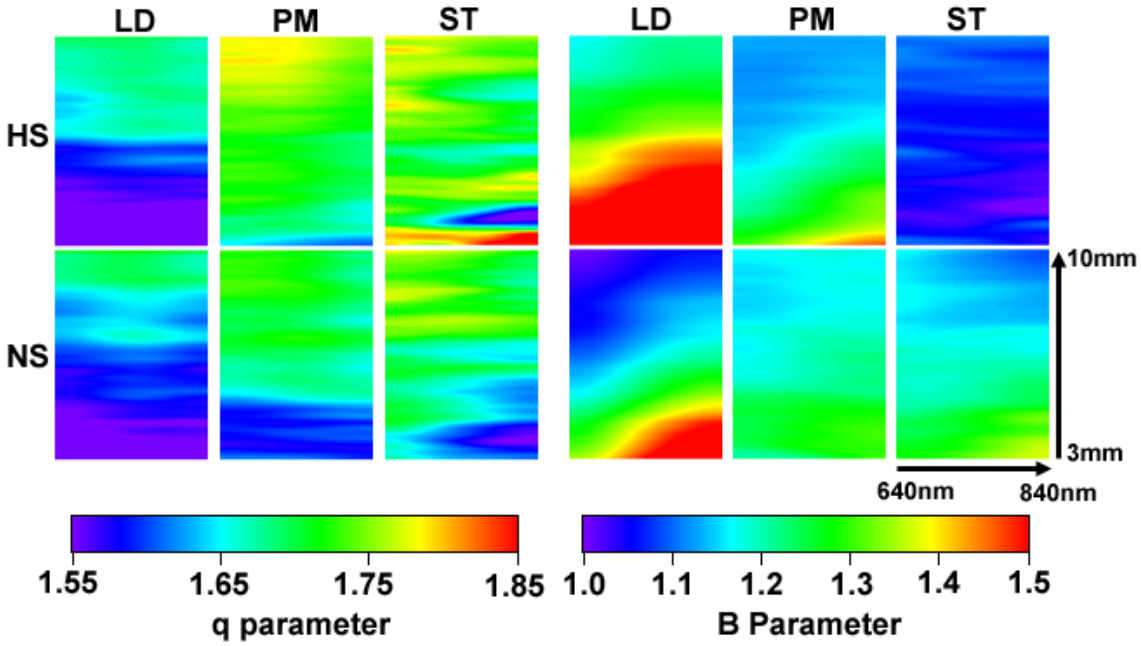

Fig. 7-3. Example fitting parameters q and B obtained from animal No.14 at 1 d postmortem. The horizontal axis is the wavelength (640 nm ~ 840 nm); while the vertical axis represents the distance from the incident point (along the x-axis in Fig.1). The values are pseudo color coded as shown in the color maps.

At each wavelength, a set of B and q parameters can be obtained at each distance from the incident location. A two dimensional (2D) map can be used to visualize the B or q parameter calculated in each sample. An example obtained in animal #14 is shown in Fig. 7-3. The vertical direction represents the fitting distance from 3 mm to 10 mm along the x-axis (Fig.1), and the horizontal direction represents the wavelengths from 640 nm to

860 nm. The 2D map is pseudo color coded. For example, in the B parameter map, the red color indicates a B parameter of 1.5 and the purple color indicates a B parameter of 1.0. Similar to our previous measurements in *M. sterniomadibularis* muscle (Ranasinghesagara and Yao 2007), the calculated bias parameter B generally decreases with the distance between the measurement location and the incident point as shown in Fig. 7-3. Both B and q parameters have larger variations at distances close to the incident point. However, they become stabilized beyond 8 mm from the center. We extracted equi-intensity contours at 0.05 mm step and calculated mean B and q parameters for all contours from 8.5 mm to 9.0 mm for our analysis below.

The extracted B and q parameters discussed above have a weak dependence on wavelength. On the contrary, the obtained spatial gradient (both parallel and perpendicular to muscle fibers) and scattering intensity are strong wavelength dependent. As shown in Fig. 7-4, the gradient curves resemble the absorption spectra of myoglobin with a small peak at ~760 nm (Xia and others, 2006).

Meanwhile, the intensity spectra show a dip at this wavelength. This phenomena can be understood because the total diffuse intensity and the spatial gradient are subject to the effects of both tissue scattering and absorption (Xia and others, 2006; 2008a). However, the weak wavelength dependent nature of the B and q parameters suggests that they are not sensitive to muscle absorption. To simplify our analysis below, only optical measurements at 720 nm are used with the understanding that the spectra information warrants further investigation.

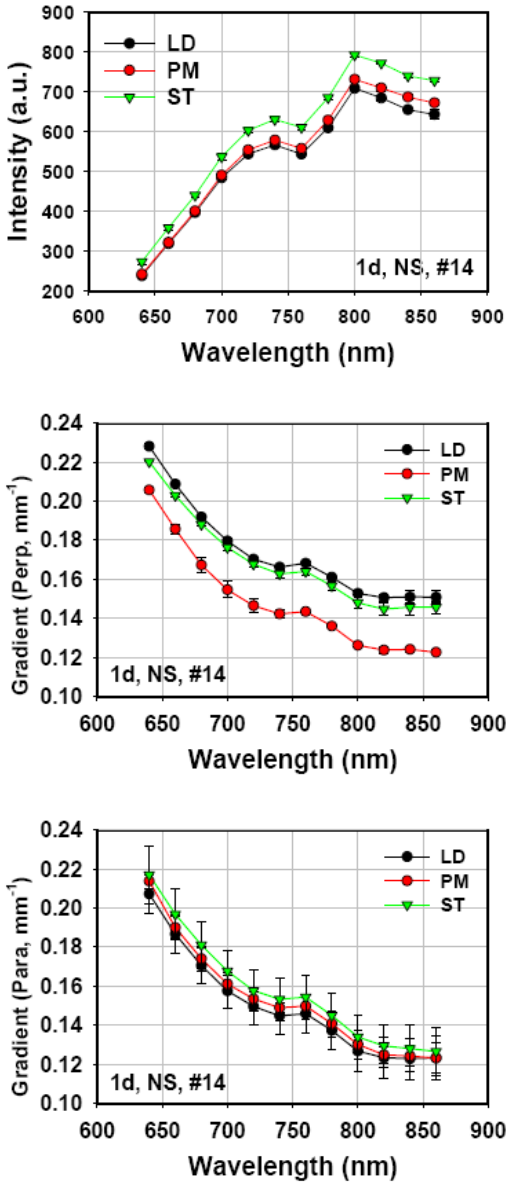

Fig. 7-4. The spectra of scattering intensity and spatial gradients measured from animal No. 14 at 1day postmortem.

7.3.1 Muscle effect

Both the spatial gradient parallel to the muscle fiber and mean intensity is significantly different for different muscle types (p<0.05) (Fig. 7-5). In addition, B parameter and spatial gradient perpendicular to muscle fiber is significantly different between PM muscles and the other two.

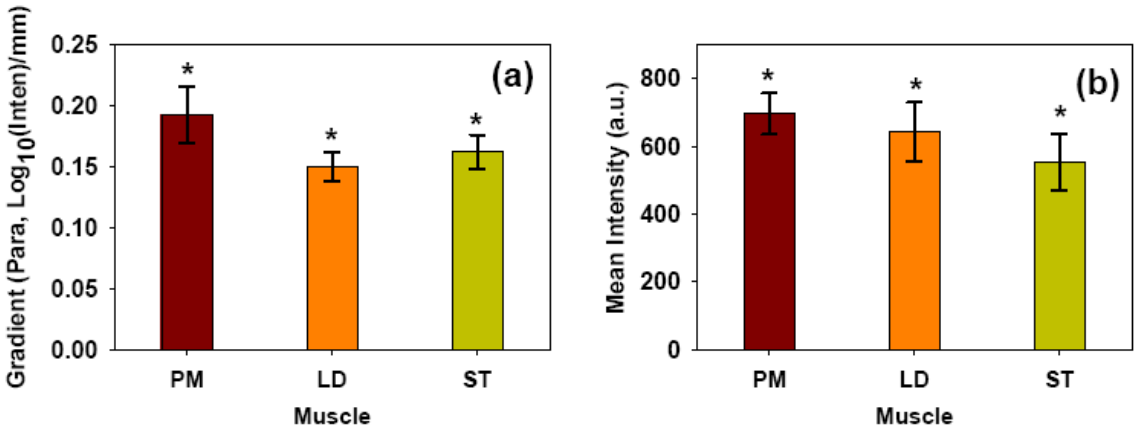

Fig. 7-5. Muscle type effect. (a) Spatial gradient parallel to the muscle fiber and (b) mean intensity for different muscle for different muscle types.

The q parameter for LD muscles is significantly different from the other two. Different muscle types carry different collagen content, fiber size, biochemical compositions and undergo dissimilar proteolysis process. Above results indicate that such factors affect light propagation of muscle significantly.

7.3.2 Aging effect

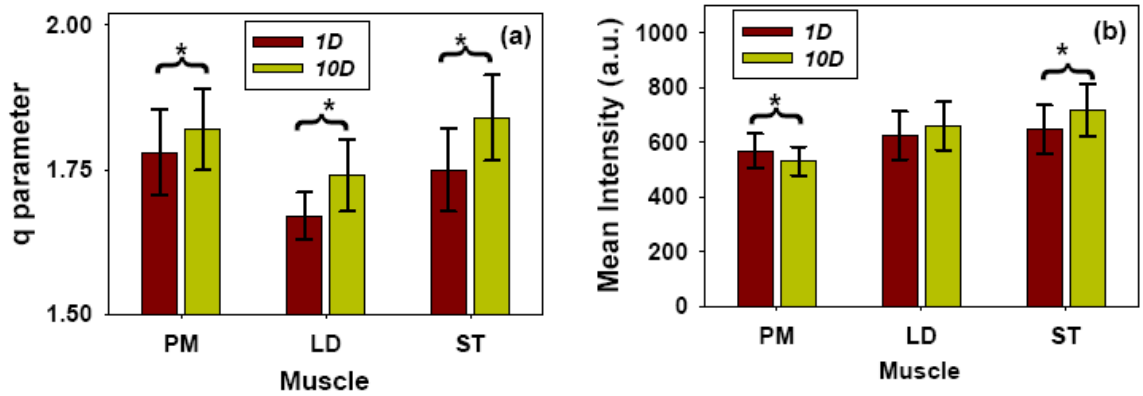

Fig. 7-6. The aging effect on (a) q parameter and (b) mean intensity for different muscle measured at 1day and 10day. Number of data acquired for each muscle type is 28. Asterisk (*) indicates *one breed* is significantly different from other. Error bars indicate the standard deviation.

As shown in Fig. 7-6, the q parameter and mean intensity are significantly different (p<0.05) for 1 day and 10 day measurements of PM and ST muscle. During the aging

process, proteolysis process affects the sarcomere structure. The unique profile gradually gets the elliptic profile with the time. Meanwhile, 1 day and 10 day measurements of two spatial gradients (⊥ and //) for PM muscle are significantly different (p<0.0001).

7.3.3 The breed effects

The *Bos indicus* breed has a slower proteolysis process than the *Bos taurus* breed traditionally. In this study, all optical parameters except spatial gradient perpendicular to the muscle fiber show significantly different results for two breeds (p<0.01).

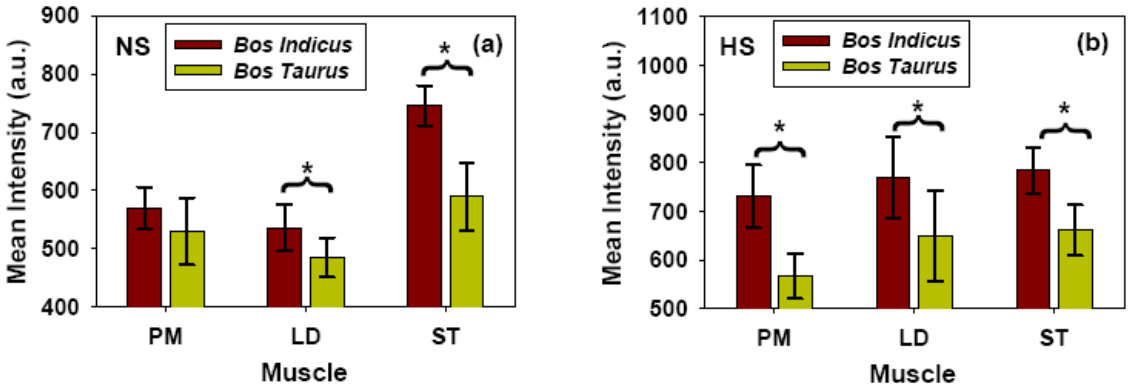

Fig. 7-7. Mean intensity obtained from 10 day optical reflectance images of *Bos indicus* and *Bos taurus* breeds. (a) NS and (b) HS. Asterisk (*) indicates *Bos indicus* is significantly different from *Bos taurus* animals (p<0.05). Number of data acquired for each animal type is 7. Error bars indicate the standard deviation.

The mean intensity shows significantly different values (p<0.05) for two breed in 10 day measurements except PM-NS. Figure 7-7 shows the mean intensity for each breed based on muscle type and suspension. Chemical changes of the muscle by inheritance can be reflected by mean intensity.

7.3.4 Correlation between WBSF and optical parameters

We analyzed the correlation between WB shear force and optical parameters because shear force is a good indicator for meat tenderness. The q parameter showed a

low correlation with the shear force (r = 0.35) (Fig. 7-8). But further analysis has shown the q parameter of NS muscles have good correlation (r = 0.55) and HS muscles have no correlation. In HS, sarcomere lengths were distributed in a narrow range. The q parameter may not be sensitive enough to small sarcomere length changes. Both spatial gradients demonstrate slightly larger correlation with shear force than the mean intensity or q parameter.

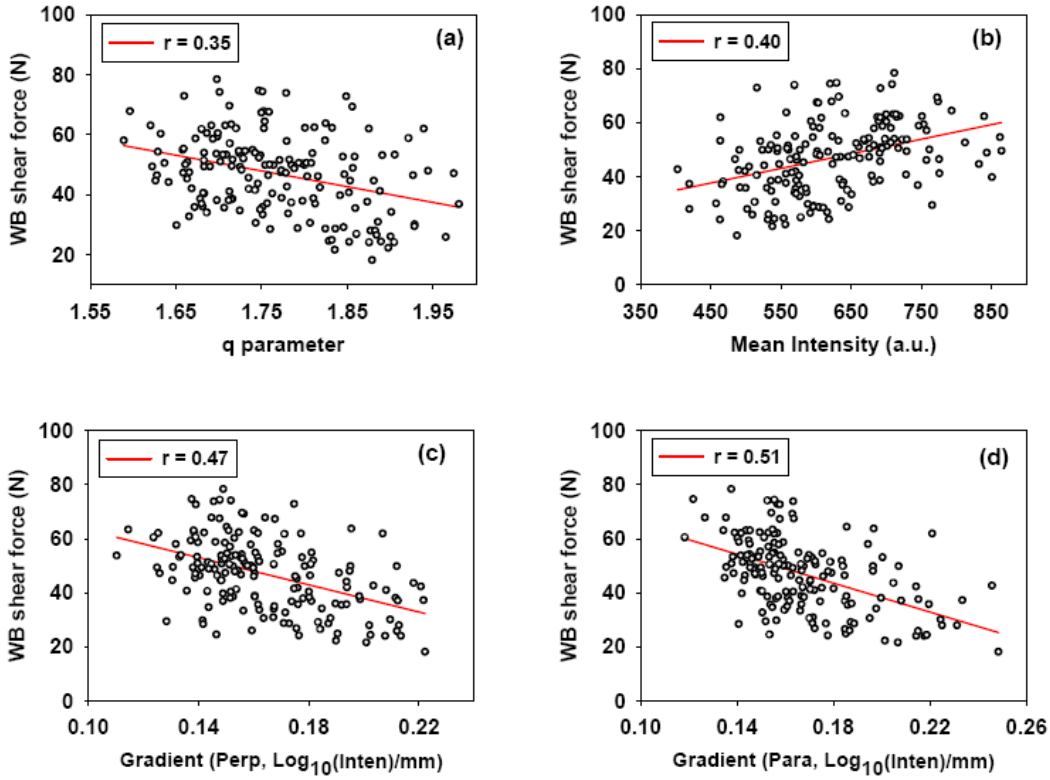

Fig. 7-8. Correlation between shear force and (a) q parameter (b) mean intensity (c) spatial gradient perpendicular to muscle fiber and (d) spatial gradient parallel to the muscle fiber.

7.4 CONCLUSION

We extracted a set of optical parameters from optical reflectance images. Two dimensional optical reflectance images are able to produce comprehensive optical parameters for studying light propagation in muscle in detail. The measured optical

parameters are strongly affected by the breed, muscle type and aging. Further studies on large group of muscles are necessary to develop a statistical model to predict physical and chemical activities in muscle.

CHAPTER 8

SUMMARY AND FUTURE DIRECTIONS

We have successfully implemented a photon migration technique in a fast laser scanning system to quantify fiber formation in soy protein extrudates. However, our studies are limited to samples with flat surfaces. Some food processors produce extrudates with curved surfaces such as cylindrical extrudates. In such extrudates, the optical reflectance profile captured by a camera does not represent the real optical reflectance distribution on the surface. In future development, both the theory and the fitting program need to be modified to handle samples with a curved profile.

We have studied optical reflectance in whole skeletal muscle. Simultaneously acquiring optical reflectance and transmittance may provide additional information for understanding light propagation in whole muscle. The optical parameters we obtained from optical reflected images have good correlations with physical and chemical properties of the muscle. In future studies, a large number of samples should be used to validate these results. In addition, the spectroscopy information should be explored and analyzed using more advanced statistical algorithms.

We have demonstrated that light diffraction by sarcomere plays a significant role in modulating light propagation in skeletal muscles. We have assumed whole muscle was a volumetric planner grating medium, where the cylindrical nature of the myofibril structures was not considered. Our studies have shown that inhomogeneous myofibril morphology can greatly change light diffractions in single muscle fiber. However, its effect on light propagation in whole muscles needs further study.

APPENDIX

COPYRIGHT PERMISSIONS

1.1 JOURNAL OF FOOD SCIENCE

-----Original Message-----
From: Mothersole, Laura - Oxford on behalf of Permission Requests - UK
Sent: Thu 11/20/2008 4:19 AM
To: Ranasinghesagara, Janaka C. (MU-Student)
Subject: RE: Request permission

Dear Janaka Ranasinghesagara

Thank you for your email request. Permission is granted for you to use the material below (print only) for your thesis/dissertation subject to the usual acknowledgements and on the understanding that you will reapply for permission if you wish to distribute or publish your thesis/dissertation commercially.

Best wishes,
Laura Mothersole

Permissions Assistant
Wiley-Blackwell
9600 Garsington Road
Oxford OX4 2DQ
UK
Tel: +44 (0) 1865 476160
Fax: +44 (0) 1865 471158
Email: laura.mothersole@wiley.com

-----Original Message-----
From: Ranasinghesagara, Janaka C. (MU-Student) [mailto:jcrqm5@mizzou.edu]
Sent: 11 November 2008 21:15
To: Permission Requests - UK
Subject: Request permission

Dear Sir/Madam,

The purpose of this letter is to request approval for using following published work in my PhD dissertation.

1. J. Ranasinghesagara, F. Hsieh, and G. Yao, "An image processing method for quantifying fiber formation in meat analogs under high moisture extrusion," J Food Sci.70, E450-454 (2005).

2. J. Ranasinghesagara, F. Hsieh, and G. Yao, "A photon migration method for quantifying fiber formation in meat analogs," J. Food Sci.71, E227-231(2006).

3. J. Ranasinghesagara, F. Hsieh, H. Huff, and G. Yao, "A laser scanning system for real-time mapping of fiber formations in meat analogs," J. Food Sci., In press (2009).

Please grant permission to use above mentioned journal publications in my PhD dissertation. If you have any questions, please email me at jcrqm5@mizzou.edu

Sincerely,
Janaka Ranasinghesagara

Janaka C. Ranasinghesagara
PhD Candidate
Biological Engineering
University of Missouri - Columbia

1.2 OPTICAL SOCIETY OF AMERICA

-----Original Message-----
From: Lehman, Susannah [mailto:SLEHMA@osa.org]
Sent: Tue 11/11/2008 3:57 PM
To: Ranasinghesagara, Janaka C. (MU-Student)
Subject: RE: Request permission

Dear Janaka Ranasinghesagara,

Your permission is below.

Sincerely,
Susannah Lehman

The Optical Society of America considers the below requested use of its copyrighted material to be allowed under the OSA Author Agreement submitted by the requestor on acceptance for publication of his/her manuscript. It is requested that a complete citation of the original material be included in any publication.

Susannah Lehman
Authorized Agent
Optical Society of America

-----Original Message-----
From: Ranasinghesagara, Janaka C. (MU-Student) [mailto:jcrqm5@mizzou.edu]
Sent: Tuesday, November 11, 2008 4:11 PM
To: Copyright
Subject: Request permission

Dear Sir/Madam,

The purpose of this letter is to request approval for using following published work in my PhD dissertation.

1. Janaka Ranasinghesagara, Gang Yao, "Imaging 2D optical diffuse reflectance in skeletal muscle" Opt. Express, Vol 15, Issue 7, p3998-4007 (2007).

2. Janaka Ranasinghesagara, Gang Yao, "Effects of inhomogeneous myofibril morphology on optical diffraction in single muscle fibers," J Opt. Soc. Am. A, 25(12), In press (2008).

Please grant permission to use above mentioned journal publications in my PhD dissertation. If you have any questions, please email me at jcrqm5@mizzou.edu

Sincerely,
Janaka Ranasinghesagara

Janaka C. Ranasinghesagara
PhD Candidate
Biological Engineering
University of Missouri - Columbia

REFERENCES

Akdogan H. 1999. High moisture food extrusion. Int J Food Sci. & Tech. 34:195-207.

Astrand B & Baerveldt AJ. 2005. A vision based row-following system for agricultural field machinery. Mechatro. 15:251-269.

Bargo PR, Prahl SA, Goodell TT, Sleven RR, Koval G, Blair G & Jacques SL. 2005. In vivo determination of optical properties of normal and tumor tissue with white light reflectance and an empirical light transport model during endoscopy. J Biomed Opt. 10:034018.

Baskin RJ, Roos KP & Yeh Y. 1979. Light diffraction study of single skeletal muscle fibers. Biophys. J 28:45-64.

Baskin RJ, Leiber RL, Oba T & Yeh Y. 1981. Intensity of light diffraction from striated muscle as a function of incident angle. Biophys. J 36:759-773.

Bate Smith EC. 1939. Changes in elasticity of mammalian muscle undergoing rigor mortis. J Physio. 96:176-193.

Beekvelt Van MCP, Willy N, Colier JM, Weavers RA & Van Engelen BGM. 2001. Performance of near infrared spectroscopy in measuring local O2 consumption and blood flow in skeletal muscle. J. Appl. Physiol. 90:511-519.

Binzoni T, Courvoisier C, Giust R, Tribillion G, Gharbi T, Hebden JC, Leung TS, Roux J & Delpy DT. 2006. Anisotropic photon migration in human skeletal muscle. Phys. Med. Biol. 51:N79-90.

Bonnemann CG & Laing NG. 2004. Myopathies resulting from mutations in sarcomeric proteins. Curr. Opin. Neurol. 17:529-537.

Breene WM & Baker TG. 1975. Development and application of a texture measurement procedure for textured vegetable protein. J Texture Studies 6:459-472.

Brenner B. 1985. Sarcomeric domain organization within single skinned rabbit psoas fibers and its effects on laser light diffraction patterns. Biophys. J 48:967-982.

Buchthal F & Knappeis GG. 1940. Diffraction spectra and minute structure of the cross-striated muscle fiber. Skand. Arch. Physiol 83:281-307.

Burkholder TJ & Lieber RL. 2001. Sarcomere length operating range of vertebrate muscles during movement. J Exp. Bio. 204:1529-1536.

Burton K & Huxley AF. 1995. Identification of Source of Oscilations in Apperent Sarcomere Length Measured by Laser Diffraction. Biophys. J 68:2429-2443.

Byrne CE, Downey G, J TD & Buckley DJ. 1998. Non-destructive prediction of selected quality attributes of beef by near-infrared reflectance spectroscopy between 750 and 1098 nm. Meat Sci 49:399-409.

Carlsen F, Knappeis GG & Buchthal F. 1961. Ultrastructure of the resting and contracted striated muscle fiber at different degrees of stretch. J Biophys. Biochem. Cyto. 11:95-117.

Cheftel JC, Kitigawa M & Queguiner C. 1992. New protein texturizing process by extrusion cooking at high moisture levels. Food Rev. Int. 8(2):235-275.

Chen B, Tojo S & Watanabe K. 2003. Machine vision for a micro weeding robot in a paddy field. Biosys. Eng. 85:393-404.

Crouse JD, Cundiff LV, Koch RM, koohKaraie M & Seideman SC. 1989. Comparisons of Bos indicus and bos taurus inheritance for carcass beef characteristics and meat palatability. J Ani. Sci. 67:2661-2668.

Dagdug L, Weiss GH & Gandjbakhche AH. 2003. Effects of anistropic optical properties on photon migration in structural tissues. Phys. Med. Biol. 48:1361-1370.

Delbridge LMD & Roos KP. 1977. Optical methods to evaluate the contractile function of unloaded isolated cardiac myocytes. J Mol. Cell Cardiol. 29:11-25.

Ding W, Fujita H & Kawai M. 2002. The length of cooperative units on the filament in rabbit psoas muscle fibres. Exp. Pysiol. 87:691-697.

Duda RO & Hart PE. 1973. Pattern Classification and Scene Analysis, 1st ed. New York: John Wiley & Sons. 482p.

Fitzgibbon A, Pilu M & Fisher RB. 1999. Direct Least Square Fitting of Ellipses. IEEE Trans. Patt. Anal. Mach. Int. 21(5):476-480.

Fujime S. 1975. Optical diffraction study of muscle fibers. Biochim. Biophys. Acta 37:227-238.

Fujime S & Yoshino S. 1978. Optical diffraction study of muscle fibers. I. A theoretical basis. Biophys. Chem. 8:305-315.

Gaylord TK & Moharam MG. 1995. Analysis and application of optical diffraction by grating. Proc. IEEE 73:894-937.

Gillis WA & Hendrickson RL. 1969. The Influence of Tension on Pre-Rigor Excised Bovine Muscle. J Food Sci. 34:375-375.

Golbitz P. 2006. Soyfoods: The U.S. Market 2006. Web Address: http://soyatech.com/pdf/06soystudy.pdf. Accessed: Nov, 2008.

Goll DE, Thompson VF, Li H, Wei W & Cong J. 2003. The calpain system. Physiol. Rev. 83:731-801.

Gonzalez RC & Wintz P. 1987. Digital Image Processing, 2nd ed. New York: Addison-Wesley. 503p.

Gwiazda S, Noguchi A & Saio K. 1987. Microstructural studies of textured vegetable protein products: effects of oil addition and transformation of raw materials in various sections of a twin screw extruder. Food Microstr. 6:57-61.

Hampson NB & Piantadosi CA. 1998. Near infrared monitoring of human skeletal muscle oxygenation during forearm ischemia. J Appl. Physiol. 64:2449-2457.

Hebden JC, Guerero JJG, Chernomordik V & Gandjbakhche AH. 2004. Experimental evaluation of an anisotropic scattering model of a slab geometry. Opt. Letters 29:2518-2520.

Heino J, Arridge S, Sikora J & Somersalo E. 2003. Anisotropic effects in highly scattering media. Phys. Rev. E68(031908):1-8.

Heiskala J, Neuvonen T, Grant PE & Nissilä I. 2007. Significance of tissue anisotropy in optical tomography of the infant brain. Appl. Opt. 46:1633-1640.

Hertzman C, Olsson U & Tornberg E. 1993. The influence of high temperature, type of muscle and electrical stimulation on the course of rigor, ageing and tenderness of beef muscles. Meat Sci. 35:119-141.

Hostetler RL, Landmann WA, Link BA & Fitzhugh Jr HA. 1970. Influence of Carcass Position During Rigor Mortis on Beef Muscles: Comparison of two Treatments. J Ani. Sci. 31:47-50.

Hough PVC, inventor. 1962. Method and means for recognizing complex patterns. USA patent 3,069,654.

Huanga H, Yua H, Xua H & Ying Y. 2008. Near infrared spectroscopy for on/in-line monitoring of quality in foods and beverages: A review. J Food Eng. 87(3):303-313.

Huxley AF. 1990. Theoretical treatment of diffraction light by a striated muscle fibre. Proc R Soc. Lond B 241:65-71.

Huxley AF & Niedergerke R. 1958. Measurement of the striations of isolated muscle fibers with the interference microscope. J Physio. 144:403-425.

Huxley HE & Hanson J. 1954. Changes in the cross-striations of muscle during contraction and stretch and their structural interpretation. Nature 173:973-996.

Huxley HE & Hanson J. 1957. Quantitative studies on the structure of cross striated myofibrils. Biochim. Biophys. Acta 23:229-249.

Ishiwata S, Muramatsu K & Higuchi H. 1985. Disassembly from both ends of thick filaments in rabbit skeletal muscle fibers. An optical diffraction study. Biophys. J 47(3):257-266.

Iwai T, Takai N & Asakura T. 1982. Dynamic statistical properties of laser speckle produced by a moving diffuse object under illumination of a Gaussian beam. J Opt. Soc. Am. 72(4):460-467.

Jimenez A, Jain AK, Ceres R & Pons JL. 1999. Automatic fruit recognition: a survey and new results using range/attenuation images. Patt. Rec. 32:1719-1736.

Judy MM, Summerour T, Leconey R, Roa RL & Templeton GH. 1982. Muscle diffraction theory. Biophys. J 37:475-487.

Kawai M & Kuntz ID. 1973. Optical diffraction studies of muscle fibers. Biophys. J 13:857-876.

Kazemzadeh M, Diehl KC, Jr. Rhee & Daham PF. 1986. Mechanical and structural evaluation of the texturied soy proteins of varying protein content. Cereal Chem. 63(4):304-310.

Kienle A. 2007. anisotropic Light Diffusion. An Onymoron? Phy. Rev. Lett. 98(21):4.

Kienle A, Forster FK & Hibst R. 2004. Anisotropy of light propagation in biological tissue. Opt. Letters 29:2617-2619.

Kienle A, Forster FK, Diebolder R & Hibst R. 2003. Light propagation in dentin: influence of microstructure on anisotropy. Phys. Med. Biol. 48:N7-14

Kienle A, D'Andrea C, Foschum F, Taroni P & Pifferi A. 2008. Light propagation in dry and wet softwood. Opt. Express 16(13):9895-9906.

Knappeis GG & Carlsen F. 1962. The ultrastructure of the Z disc in skeletal muscle. J Cell Bio. 13:323-335.

Koch RM, Dikeman ME, Allen DM, May M, Crouse JD & Campion DR. 1976. Characterization of biological types of cattle. III. Carcass composition quality and palatability. J Ani. Sci. 54:35-45.

Kogelnik H. 1969. Coupled wave theory for thick hologram grating. Bell Syst. Tech. J 48:2909-2943.

Koohmaraie M, Kent MP, Shackelford SD, Veiseth E & Wheeler TL. 2002. Meat tenderness and muscle growth: is there any relationship. Meat Sci. 62:345-352.

Lalanne P. 1997. Improved formulation of the coupled-wave method for two-dimensional gratings. J Opt. Soc. Am. 14:1592-1598.

Leavers VF. 1992. Shape mical characteristics of soy protein meat analog extruded at high moisture. , 1st ed. London: Springer-Verlag. 197p.

Leiber RL, Yeh Y & Baskin RJ. 1984. Sarcomere length determination using laser diffraction. Biophys. J 45:1007-1016.

Leung AF. 1982. Calculation of the laser diffraction intensity of striated muscle by numerical methods. Comp. Prog. Biomed 15:169-174.

Leung AF. 1984. Fine structures in the light diffraction pattern of striated muscle. J Mus. Res. Cell Mot. 5:535-558.

Leung AF, Cheung YM & C HJ. 1989. Light diffraction intensity from muscle fibers in different osmotic solutions: measurement of equlibarium time. Euro. J. Physiol. 414:676-682.

Lieber RL. 2002. Skeletal Muscle Structure, Function & Plasticity: The Physiological Basis of Rehabilitation, 2nd ed. Philadelphia: Lippincott Williams & Wilkins. 369p.

Lieber RL, Loren GJ & Fridén J. 1994. In vivo measurement of human wrist extensor muscle sarcomere length changes. J Neurophysiol. 71:874-881.

Lin S, Huff HE & Hsieh F. 1997. Effects of lipids and processing conditions on degree of starch gelatinization of extruded dry pet food. Lebens-Wiss. U. Technol. 30:754-761.

Lin S, Huff HE & Hsieh F. 2000. Texture and chemical characteristics of soy protein meat analog extruded at high moisture. J Food Sci. 65(2):264-269.

Lin S, Huff HE & Hsieh F. 2000. Texture and chemical characteristics of soy protein meat analog extruded at high moisture. J Food Sci 65(2):264-269.

Lin S, Huff HE & Hsieh F. 2002. Extrusion process parameters, sensory characteristics, and structural properties of a high moisture soy protein meat analog. J Food Sci. 67(3):1066-1072.

Liu Y, Lyon LBG, Windham WR, Realini CE, Dean T, Pringle D & Duckett S. 2003. Prediction of colour, texture, and sensory characteristics of beef steaks by visible and near infrared reflectance spectroscopy. A feasibility study. Meat Sci. 65:1107-1115.

Lu R & Ariana D. 2002. Determination of firmness of intact apple fruit by near-infrared reflectance spectroscopy. Appl. Eng. Agr. 18(5):585-590.

Luping N. 1993. Texturization of soy protein via twin-screw extrusion. Urbana-Champaign: University of Illinois. p. 138.

Lusk K, Fox LJA, Schroeder TC, Mintert J & Kooharaie M. 2001. In-store valuation of steak tenderness. J Agr. Econ. 83:539-550.

Luther PK, Padron R, Ritter S, Craig R & Suire JM. 2003. Hetrogenity of Z-band Structure within a Single Muscle Sarcomere: Implications for Sarcomere Assembly. J Mol. Bio 332(161-69).

Lynch GS. 2004. Roll of contraction-induced injury in the mechanisms of muscle damage in muscular dystrophy. Clin. Exp. Pharm. 31:557-561.

Macintosh BR, Gardiner PF & McComas AJ. 2006. Skeletal Muscle: Form and Function, 1st ed. Champaign: Human kinematics. p.

Maningat CC, DeMeritt Jr. GK, Chinnaswamy R & Bassi SD. 1999. Properties and applications of texturized wheat gluten. Cereal Foods World 44(9):650-655.

Marquez G, Wang LH, Lin SP, Schwartz JA & Thompsen SL. 1998. Anisotropy in the absorption and scattering spectra of chicken breast tissue. Appl. Opt. 37:794-804.

Moharam MG & Gaylord TK. 1982. Diffraction analysis of dielectric surface-relief gratings. J Opt. Soc. Am. 72:1385-1392.

Moharam MG & Gaylord TK. 1983. Three Dimensional vector coupled-wave analysis of planer-grating diffraction. J Opt. Soc. Am. 73:1105-1112.

Moharam MG, Grann EB, Pommet A & Gaylord TK. 1995a. Formulation for stable and efficient implementation of the rigorous coupled-wave analysis of binary gratings. J Opt. Soc. Am. 12:1068-1076.

Moharam MG, Drew A, Pommet A, Grann EB & Gaylord TK. 1995b. Stable implementation of the rigorous coupled-wave analysis for surface-relief gratings: enhanced transmittance matrix approach. J Opt. Soc. Am. 12:1068-1076.

Montes JM, Utz HF, Schipprack W, Kusterer B, Muminovic J, Paul C & Melchinger AE. 2006. Near-infrared spectroscopy on combine harvesters to measure maize grain dry matter content and quality parameters. Plant Bre. 125(6):591-595.

Moss RL. 1979. Sarcomere length-tension relations of frog skinned muscle fibers during calcium activation at short length. J. Physio. 292:177-192.

Mullikin JC, Van Vliet LJ, Netten H, Boddeke FR, Feltz GV & Young IT. 1994. Method for CCD Camera Characterization. Proceedings of the SPIE Conference on Image Acquisition and Scientific Imaging Systems. San Jose: SPIE. p. 73-84.

Nickell S, Hermann M, Essenpreis M, Farrell TJ, Kramer U & Patterson MS. 2000. Anisotropy of light propagation in human skin. Phys. Med. Biol. 45:2873-2886.

Ning L. 1993. Texturization of soy protein via twin-screw extrusion. University of Illinois at Urbana-Champaign.

Nioka S & Chance B. 2005. NIR spectroscopic detection of breast cancer. Tech. Can. Res. Treat. 4(5):497-512.

Oba T, Baskin RJ & Lieber RL. 1981. Light diffraction studies of active muscle fibres as a function of sarcomere length. J Mus. Res. Cell Mot. 2(2):215-224.

Page SG & Huxley HE. 1963. Filament lengths in striated muscle. J Cell Bio. 19:369-390.

Paolini PJ, Sabbadini R, Roos KP & Baskin RJ. 1976. Sarcomere length dispersion in single muscle fibers and fiber bundles. Biophys. J 16:919-930.

Patterson MS, Chance B & Wilson BC. 1989. Time resolved reflectance and transmittance for the noninvasive measurement of tissue optical properties. Appl. Opt. 28:2331-2336.

Perez JM, Schreiner S & E GG. 2006. Evaluation of the VITUS smart laser scanner for accuracy, resolution, and repeatability for clinical assessment of Pectus deformities and scoliosis. Proceedings of the IEEE 32nd Annual Northeast Bioeng. Conf. p. 33-34.

Pratt WK. 1991. Digital Image Processing, 2nd ed. New York: John Wiley & Sons Inc. 698p.

Press WH, Flannery BR, Teukolosky SA & Vetterling WT. 1988. Numerical recipes in C: The art of scientific computing, 1st ed. Cambridge: Cambridge University Press. p.

Proske U & Morgan DL. 2001. Muscle damage from eccentric exercise: mechanism, mechanical sign, adaptation and clinical applications. J Physio. 537:333-345.

Raghavachari R. 2001. Near-Infrared Applications in Biotechnology, 1st ed. New York: Marcel Dekker. 382p.

Ramsey CB, W CJ, H MB & S TR. 1963. Effects of type and breed of British Zebu and dairy cattle on production palatability and composition II. Palatability differences and cooking losses as determined by laboratory and family panels. J Ani. Sci. 22:1001.

Ranasinghesagara J & Yao G. 2007. Imaging 2D optical diffuse reflectance in skeletal muscle. Opt. Express 15:3998-4007.

Ranasinghesagara J, Hsieh F & Yao G. 2005. An Image Processing Method for Quantifying Fiber Formation in Meat Analogs Under High Moisture Extrusion. J Food Sci. 70(8):E450-454.

Ranasinghesagara J, Hsieh F & Yao G. 2006. A photon migration method for characterizing fiber formation in meat analogs. J Food Sci. 71(5):E227-231.

Rhodes VJ, Kiehl ER & Brady DE. 1955. Visual preferences for grades of retail cuts. Missouri Agri. Exp. Sta. Res. Bull. Columbia. p. 583.

Ritter GX & Wilson JN. 1996. Handbook of Computer Vision Algorithms in Image Algebra, 1st ed. Florida: CRC Press. 448p.

Rødbotten R, Nilsen BN & Hildrum KI. 2000. Prediction of beef quality attributes from early post mortem near infrared reflectance spectra. Food Chem. 69(4):427-436.

Roussel L. 1996. Making meat products using extrusion technology. Extrusion Comm. 9(6):16-18.

Rudel R & Zite-Ferenczy F. 1979. Interpretation of light diffraction by cross-striated muscle as bragg reflexion of light by the lattice of contractile proteins. J Physio. 290:317-330.

Rudel R & Zite-Ferenczy F. 1980. Efficiency of light diffraction by cross striated muscle fibers under stretch and during isometric contraction. Biophys. J 30:507-516.

Russ J. 2005. Image Analysis of Food Microstructure, 1st ed. Florida: CRC Press. 369p.

Sezgin M & Sankur B. 2004. Survey over image thresholding techniques and quantitative performance evaluation. J Elect. Imag. 13(1):146-165.

Shackelford SD, Wheeler TL, Meade MK, Reagan JO, Byrnes BL & Koohmaraie M. 2001. Consumer impressions of Tender Select beef. J Ani. Sci. 79:2605-2614.

Sidick E, Baskin RJ, Yeh Y & Knosen A. 1994. Rigorous analysis of light diffraction ellipsometry by striated muscle fibers. Biophys. J 66:2051-2061.

Sidick E, Knosen A, Xian K, Yeh Y & Baskin RJ. 1992. Rigorous analysis of light diffraction by a striated muscle Fiber. Bio Sci. R Soc. 249.

Snyder HE. 1968. The study of myoglobin derivatives in meat samples by reflectance spectrophotometry. American Meat Institute Foundation. Chicago. p. 21-31.

Stark H & Lubensky TC. 1996. Multiple Light Scattering in Nematic Liquid Crystals. Phys. Rev. Lett. 77:2229-2232.

Sundell CL, Goldman YE & Peachey LD. 1986. Fine structure in near-field and far-field laser diffraction patterns from skeletal muscle fibers. Biophys. J 49:521-530.

Sviridov A, Chernomordik V, Hassan M, Russo A, Eidsath A, Smith P & Gandjbakhche AH. 2005. Intensity profiles of linearly polarized light backscattered from skin and tissue-like phantoms. J Biomed. Opt. 10(014012):1-9.

Swatland HJ. 1989. A review of meat spectrophotometry (300 to 800 nm). Can Inst. Food Sci. Tech J 22:390-402.

Swatland HJ & Irie M. 1992. Effect of wavelength on spatial measurements of light scattering for the measurement of pork quality. J Ani. Sci. 70:2138-2143.

te Pas MFW, Everts ME & Haagsman HP. 2004. Muscle Development of Livestock Animals: Physiology, Genetics, and Meat Quality, 1st ed. Oxfordshire: CABI Publishing. 428p.

Theodoridis S & Koutroumbas K. 2003. Pattern Recognition, 2nd ed. San Diego: Academic Press. 689p.

Thornhill RA, Thomas N & Berovic N. 1991. Optical diffraction by well ordered muscle fibers. Eur. Biophys. 20:87-99.

Tuchin V. 2000. Tissue Optics, 1st ed. Bellingham: SPIE Press. 378p.

Van der Aa NP & Mattheij RMM. 2007. Computing shape parameter sensitivity of the field of one-dimensional surface-relief gratings by using an analytical approach based on RCWA. J Opt. Soc. Am. 24:2692-2700.

Van Syckle C & Brough Jr OL. 1958. Customer acceptance of fat characteristics of beef. Washington DC: Washington Agri. Exp. Sta. Tech. Bull. p. 27.

Wang LH & Jacques SL. 1995. Use of a laser beam with an oblique angle of incidence to measure the reduced scattering coefficient of a turbid medium. Appl. Opt. 34(13):2362-2366.

Wang LH, Jacques SL & Zheng L. 1995. MCML - Monte Carlo modeling of light transport in multi-layered tissues. Comp. Meth. Prog. Biomed. 47:131-146.

Weeks Jr. AR. 1996. Fundamentals of Electronic Image Processing, 1st ed.: Wiley-IEEE Press 576p.

Weiss GH. 1994. Aspects and applications of the random walk, 1st ed. Amsterdam: North Holland. 361p.

Weiss GH, Porra JM & Masoliver J. 1998. The continuous-time random walk description of photon motion in an isotropic medium. Opt. Comm. 146:268-276.

Wolf WJ & Cowan JC. 1975. Soybeans as a Food Source, ed. Boca Raton: CRC Press. p.

Xia J, Weaver A, Gerrard DE & Yao G. 2006. Monitoring sarcomere structure changes in whole muscle using diffuse reflectance. J Biomed. Opt. 11(040504):1-3.

Xia J, Berg EP, Lee JW & Yao G. 2007. Characterizing beef muscles with optical scattering and absorption coefficients in VIS-NIR region. Meat Sci 75(1):78-83.

Xia J, Weaver A, Gerrard DE & Yao G. 2008a. Distribution of optical scattering properties in four beef muscles. Sens. & Inst. Food Qual. 2:75-81.

Xia J, Weaver A, Lee BE & Yao G. 2008b. Heating induced optical property chages in beef muscle. J Food Sci 84:75-81.

Yao G, Liu K & Hsieh F. 2004. A new method for characterizing fiber formation in meat analogs during high-moisture extrusion. J Food Sci. 69(7):E303-307.

Yeh Y & Baskin RJ. 1988. Thory of optical ellipsometric measurements from muscle diffraction studies. Biophys. J 54:205-218.

Yeh Y, Baskin RJ & Roos KP. 1980. Theory of light diffraction by single skeletal muscle fibers. Biophys. J 29:509-522.

Yousif HA & Boutros E. 1992. A FORTRAN code for the scattering of EM plane waves by an infinitely long cylinder. Phys. Comm. 69:406-416.

Yu G, Lech G, Zhou C, Chance B, Mohler III ER & G YA. 2005. Time-dependent blood flow and oxygenation in human skeleton muscles with non invasive near-infrared diffuse optical spectroscopy. J Biomed. Opt. 10(0240271).

Zijp JR & ter Bosch JJ. 1998. Optical properties of bovine muscle tissue in vitro; a comparison methods. Phys. Med. Biol. 43:3065-3081.

VITA

Janaka C. Ranasinghesagara was born in Kottawa, Sri Lanka. He received his bachelor's degree in electrical engineering in 1996 from University of Moratuwa, Sri Lanka. After obtaining his degree, he worked as a lab instructor in the same university for four months. Then he moved to industry and worked as an electrical and communication engineer at Scopex Power & Plant until he came to the USA in 1997. While working in the electrical and communication industry, he studied for his master's degree in electrical engineering as a part time student at California State University, Long Beach. He completed his master's degree in electrical engineering in May 2002 and started his Ph.D. in biomedical engineering at the University of Texas, Arlington (UTA) in August 2004. After completing one semester at UTA, he transferred to the University of Missouri and enrolled in the biological engineering program as a PhD student. His research interest is light-tissue interaction.